Nonlinear Inelastic Mechanical Behavior

Of Epoxy Resin Polymeric Materials

by

Masoud Yekani Fard

A Dissertation Presented in Partial Fulfillment
of the Requirements for the Degree
Doctor of Philosophy

Approved June 2011 by the
Graduate Supervisory Committee:

Aditi Chattopadhyay, Chair
Lenore Dai
Jian Li
Antonia Papandreou-Suppappola
John Rajadas

ARIZONA STATE UNIVERSITY

August 2011

ABSTRACT

Polymer and polymer matrix composites (PMCs) materials are being used extensively in different civil and mechanical engineering applications. The behavior of the epoxy resin polymers under different types of loading conditions has to be understood before the mechanical behavior of Polymer Matrix Composites (PMCs) can be accurately predicted. In many structural applications, PMC structures are subjected to large flexural loadings, examples include repair of structures against earthquake and engine fan cases. Therefore it is important to characterize and model the flexural mechanical behavior of epoxy resin materials. In this thesis, a comprehensive research effort was undertaken combining experiments and theoretical modeling to investigate the mechanical behavior of epoxy resins subject to different loading conditions. Epoxy resin E 863 was tested at different strain rates. Samples with dog-bone geometry were used in the tension tests. Small sized cubic, prismatic, and cylindrical samples were used in compression tests. Flexural tests were conducted on samples with different sizes and loading conditions. Strains were measured using the digital image correlation (DIC) technique, extensometers, strain gauges, and actuators. Effects of triaxiality state of stress were studied. Cubic, prismatic, and cylindrical compression samples undergo stress drop at yield, but it was found that only cubic samples experience strain hardening before failure. Characteristic points of tensile and compressive stress strain relation and load deflection curve in flexure were measured and their variations with strain rate studied. Two different stress strain models were used to investigate the effect of out-of-plane loading on the uniaxial stress strain response of the epoxy resin material. The first model is a strain softening with plastic flow for tension and compression. The influence of softening localization on material behavior was investigated using the DIC system.

It was found that compression plastic flow has negligible influence on flexural behavior in epoxy resins, which are stronger in pre-peak and post-peak softening in compression than in tension. The second model was a piecewise-linear stress strain curve simplified in the post-peak response. Beams and plates with different boundary conditions were tested and analytically studied. The flexural over-strength factor for epoxy resin polymeric materials were also evaluated.

DEDICATION

I dedicate this dissertation to my parents for

instilling the importance of hard work and for supporting

me pursuing my doctoral degree.

ACKNOWLEDGMENTS

I am greatly appreciative to Prof. Aditi Chattopadhyay whose encouragement, supervision and support from the preliminary to the concluding level enabled me to complete my study. This dissertation would not have been possible without her support. The members of my dissertation committee, Prof. Antonia Papandreou-Suppappola, Prof. Jian Li, Prof. John Rajadas, and Prof. Lenore Dai have generously given their time and expertise to better my work. I thank them for their helpful suggestions, insightful discussions and their good-natured support. I would also like to thank all my fellow graduate students who supported me in any respect during the completion of the project. I also would like to make a special help to Ms. Kay Vasley, the executive assistant of AIMS center, for all the help and support. Next, I would like to acknowledge the support of Dr. Kingsbury from the school of engineering of matter, transport and energy.

This thesis was supported by the Army Research Office, AMSRD-ARL-RO-SI Proposal Number: 49008-EG, Agreement Number: W911NF-07-1-0132, Program Manager: COL. Reed F. Young. The support is greatly appreciated.

TABLE OF CONTENTS

LIST OF TABLES

Table Page

LIST OF FIGURES

Figure Page

Figure Page

1. Introduction to Mechanical Behavior of Epoxy Resin Polymeric Materials

1.1. Motivation

Polymeric materials play an important role in modern industries today. Polymer and polymer matrix composites (PMC), in particular, due to their lightweight and excellent mechanical characteristics, are being extensively used in a variety of civil and mechanic engineering applications such as repair and rehabilitation of structures against earthquake and aircraft engine fan cases. Over the past several decades, the understanding of their mechanical behavior has significantly advanced, but due to their different deformation modes, the material response of PMCs takes on complexities. Unlike metals, where conducting different types of loading tests and specimens geometries do not present a significant problem due to homogeneity and isotropy of metals, in polymeric material and PMCs, this type of testing is challenging because of the inhomogeneities and anisotropy.

Another aspect in which the relationship between load and deformation in epoxy resins is more complex than in metals is that the hydrostatic component of the stress on epoxy resins has a significant effect on material response. Furthermore, epoxy resin behavior under different types of load and loading conditions has to be understood before the mechanical behavior of PMCs can be accurately predicted. Finally, the mechanical properties (stress strain curve and fracture patterns) of epoxy resin polymeric materials are sensitive to the rate and environmental conditions in which they are loaded and deformed.

Although there is considerable literature on the behavior of polymeric materials with regards to tension, compression, and shear at different strain rates and temperatures, test results obtained thus far contain many discrepancies. These differences are especially more discernable in the post-peak region of the material's response. Details about these discrepancies are discussed in chapter 2, section 2.1.

Over the past three decades, several constitutive models have been proposed for polymeric materials. These models have been particularly successful in fitting quasi-static, in-plane test results, and have been able to partially describe the material response at different strain rates. However, in many structural applications, polymer based composite structures are usually subjected to large flexural loadings; therefore, it is important to characterize and model the flexural behavior of these structures and their constituents.

The literature, to date, provides many mechanical characterization studies where the averaged mechanical response over the entire specimen volume is taken as the point-wise material response. However, averaging over a specimen that is deforming non-homogeneously will lead to excessive error. Also, in order to study the flexural behavior of epoxy resin materials, a complete set of material properties (tension, compression, and bending) at different strain rates is needed. Therefore, to improve analysis capabilities and arrive at a precise prediction of structural behavior, a constitutive relation of materials is desirable for describing material property behavior under various loading conditions. To the best of this author's knowledge, no material characterization study exists in the literature that relates to the tension, compression, and flexural behavior of a single type of epoxy resin material.

In this dissertation, comprehensive research has been undertaken, combining theoretical model development, simulation, and experiments to investigate the flexural response of epoxy resin polymeric materials subject to different loading rates. Specimens with different geometries and sizes are designed to study different effects, such as slenderness ratio, side effects, etc., on the mechanical behavior of the epoxy resin polymeric materials.

Recently there has been significant interest in high fidelity multiscale modeling techniques for accurate characterization and response analysis, as well as damage evolution and failure mechanisms in both metallic and composite materials. The results from multiscale analysis are also being used in Structural Health Monitoring (SHM) applications. However, accurate multiscale modeling depends on the use of proper constitutive models of the constituents. During loading, polymer composite structures are often subjected to large flexural stresses; thus the flexural response of these structures and their constituents must be accurately modeled.

Two different models representing the flexural behavior of epoxy resin materials have been proposed: 1) a bi-linear ascending model with post-peak strain softening followed by constant plastic flow in tension and compression, and 2) a bi-linear ascending model with simplified post-peak response in tension and compression. It is observed that the constitutive stress strain relationship obtained from uniaxial tension and compression tests must be modified to obtain the flexural response of polymeric materials.

1.2. Background

The mechanical properties of fiber reinforced polymeric composites are of increasing interest as their applications in mechanical and civil industries become widespread. These properties are affected by mechanical properties of the matrix, so the role of epoxy resin in polymeric matrix composites is critical due to the nonlinear nature of polymer behavior. A characteristic feature of polymers is the way in which they respond to an applied stress or strain depending on the rate, temperature, or time period of loading. If a polymer is subjected to a rapid change in strain, it appears stiffer than if the strain were applied at a slower rate (Ward and Sweeney, 2004). The stress strain behavior can be brittle, plastic, and highly elastic (elastomeric or rubber-like). Tensile modulus and

tensile strengths are orders of magnitude smaller than those of metals, but elongation can be up to 1000% in some cases.

Mechanical properties change dramatically with temperature, from glass-like brittle behavior at low temperatures to a rubber-like behavior at high temperatures (Ward and Sweeney, 2004). In general, decreasing the strain rate like increasing the temperature makes polymer softer and more ductile. Initially, the stress strain response is linear, which means that an elastic, fully recoverable deformation is taking place, and at this stage recoverable rotation of the molecules is also occurring. Once the stress strain curve becomes nonlinear, plastic deformation takes place, which is non-recoverable on unloading.

There is extensive data in the literature related to mechanical properties of polymers using different samples with various shapes and sizes, including methods of deflection and strain measurement (Littell et al., 2008; Gilat et al., 2007; Jordan et al., 2008; Shah khan et al., 2001; Chen et al., 2001; Fiedler et al., 2001; Behzadi and Jones, 2005; Walley and Field, 1994; Liang and Liechti, 1996; G'Sell et al., 2002; G'Sell and Souahi, 1997; Boyce and Aruda, 1990; G'Sell et al., 2000; Buckley and Harding 2001; Mannocci et al., 2001; Fergusson et al., 2006). However, the accuracy of the deformation/strain measurement system and the effect of the shape and size of the sample on the material response have not been adequately studied. In the literature, the most successful constitutive stress strain models for polymeric materials have been proposed by (Buckley and Jones, 1995; Buckley and Dooling, 2004) at Oxford, (Boyce et al., 1989, 1994; Hasan and Boyce, 1995; Mulliken and Boyce, 2006) at MIT, and (Tervoort, 1996, 1998; Govaert et al., 2000) at Eindhoven. While these models differ in detail, conceptually they represent three-dimensional non-Newtonian viscoelastic and/or viscoplastic models. The

models have been shown to be successful, especially, in fitting quasi-static in-plane tension and compression test results, and are able to partially describe the material response at high strain rates. Details about these constitutive models are discussed in chapter 4, section 4.1.

In real industrial applications, however, composite structures are usually subjected to large flexural loadings, which is why the flexural behavior of these structures and their constituents are critical to their use. Flexural strength distributions and ratio of flexural strength to tension strength of epoxy resin and PMMA materials have been studied using a modified two-parameter Weibull model (Giannotti et al., 2003 and Vallo, 2002). However, to the best of the author's knowledge, no experimental study has been conducted on tension, compression, and flexural behavior of the epoxy resin material using a precise digital image correlation (DIC) system to obtain material response. In addition, there is no numerical and/or analytical simulation in the literature that explores the correlation between uniaxial inplane tension, compression constitutive stress strain relationship, and out-of-plane flexural behavior for epoxy resin polymeric materials.

This study is motivated by the need to better characterize the flexural behavior of epoxy resin materials. Experimental results obtained from a DIC system captures some of the fundamental features of the tensile and compressive true stress strain behavior of epoxy resin materials. Experiments on cubic, prismatic, and cylindrical compression samples were performed demonstrating strain stiffening at high strain values in the cubic samples due to a barrel-like phenomenon and tri-axial stress state. Therefore, for large strain values, strain hardening can be ignored in the constitutive behavior. The goal of this experimental study is to fully characterize the response of epoxy resin materials and to formulate analytical solutions.

An analytical technique has been used for epoxy resin materials to investigate the effects of out-of-plane loading on the constitutive relationship based on two different stress strain models. The first is a complete strain softening model for tension and compression defined by 14 unique parameters. The second model is a simplified constitutive stress strain curve with constant plastic flow in tension and constant yield in compression defined by 11 parameters. Closed form solutions for moment curvature response were derived based on nonlinear tension and compression stress strain curves. The results were expressed in normalized form to eliminate the effects of size and strength of specimen. A complete set of analytical parametric studies shows the correlation of flexural load carrying capacity of epoxy resin to different parts of the tension and compression stress strain curve. These results provide insight into improved modeling and design of composite structures that account for the effects of out-of-plane loading.

A technique based on the uniaxial tension and compression stress strain relations, strain compatibility in bending, static equilibrium, and softening localization was used to simulate flexural load deflection response in statically determinate beam- and plate-like structures. Since the solution is derived explicitly, the material response is accurate and the iterative procedures required for approaching material nonlinearity are not required. This method is a powerful tool for forward and inverse analyses. Using this method, it is possible to examine the effects of different segments of tension and compression stress strain curves for improving the flexural performance of epoxy resin materials.

1.3. Objectives of the Work

The research is unique because it takes on a comprehensive approach to investigating flexural behavior of polymeric materials. The results of this research will be useful for

accurate characterization and response analysis as well as for providing data for damage detection and prognosis. This research aims to accomplish the following main objectives:

1. Conduct experimental investigations to characterize different material behavior over a wide range of strain rates.

2. Investigate nonlinear behavior of polymer matrix materials under flexural loading.

3. Investigate the effect of different sections of the inplane stress strain curve on the out-of-plane structural response.

4. Investigate the effect of out-of-plane loading conditions on constitutive stress strain relationship for simulation of polymeric structures subjected to different loading rates.

5. Evaluate the effects of stress gradient on the peak tension and compression strength.

1.4. Thesis Outline

This dissertation is structured as follows:

Chapter 1 provides an introduction and rationale for the research. Chapter 2 gives an overview of tension and compression mechanical tests on polymeric materials available in the literature, with a discussion of the advantages and disadvantages of each study. Comprehensive mechanical test results over a wide range of strain rates that take into consideration the geometric effects (shape and size) of samples on the behavior of materials are presented. Results obtained from strain gauges, extensometers, and actuators are compared with accurate results from a digital image correlation (DIC) system. Empirical relations between elastic strength and the peak strength in tension and compression are also obtained.

Chapter 3 describes the experimental study on three-point bending (3PB) flexural samples with notches and grooves. Load deflection curves over a range of loading rates are presented. Beams with different dimensions are considered. Strain distributions are studied, and softening localization zones at notches and grooves around the loading nose are determined. The relation between elastic load capacity and load carrying capacity is also obtained.

Chapter 4 discusses the theory behind the methodology used to analytically simulate the flexural behavior of polymeric materials. This chapter describes available constitutive models for different mechanical behaviors of polymeric materials. It discusses the need to incorporate the effects of out-of-plane loading on constitutive stress strain models validated with in-plane loading. Two multilinear tension and compression stress strain models are assumed. In model 1 and based on the results in chapter 2, a strain softening model with constant plastic flow in tension and compression has been considered. Model 2 is a simplified model for polymeric materials in which compression is stronger than tension. This model consists of constant strain softening in tension and constant yield stress in compression. The performance of the simplified model in the prediction of the flexural response is evaluated by comparing the flexural load deflection response with the response obtained from the full softening model. Then, a brief discussion of the modeling technique is presented, as well as the procedure for arriving at the structural response, based on the nonlinear stress strain curves obtained from chapter 2. An extensive parametric study is performed to examine the effects of different segments in the stress strain curve (pre- and post-peak region) on the load deflection response at the structural level. Results of forward solution and inverse analysis techniques are shown for

3PB case. Location of the neutral axis in the nonlinear phase is studied using the DIC system.

Chapter 5 presents the implementation of the modified material constitutive models to simulate the behavior of determinate and indeterminate polymeric beam in four-point bending (4PB) and plate structures. Tension and compression stress strain curves from the inverse analysis of 3PB load deflection response are used to predict the 4PB response. Fixtures, designed and constructed to conduct tests on plates with different boundary conditions, are discussed. Experiments conducted to obtain the structural response on plates with different geometries and boundary conditions are presented. The DIC system is used to study the failure patterns. Yield line theory is applied to correlate 3PB response with the response from plates. The flexural over-strength factor derived from chapter 4 is evaluated through inverse analysis.

Chapter 6 highlights the contribution of this research in the area of engineering mechanics of epoxy resin polymeric materials. In addition, this chapter discusses the need for further research in exploring the material behavior of epoxy resin polymeric materials.

2. Tension and Compression Behavior of Epoxy Resin Over a Range of Loading Rates Using Digital Image Correlation (DIC)

2.1. Introduction

Over the past several decades, significant advances have been made on understanding the constitutive stress strain relationship of epoxy resin materials, enabling their use in a wide variety of engineering applications. There is considerable data in the literature related to the mechanical properties of polymers based on samples of different sizes. Each sample was measured using one of several common methods of deflection and strain measurements, including strain gages and extensometers. However, a complete set of material properties that takes into consideration the effect of sample geometry and size, and the effect of the measurement technique on the results is not available. Also, there are discrepancies in some of the results. Strain softening at yield, followed by strain stiffening at higher strains in compression for different low and high strain rates has been reported in many studies (Fiedler et al., 2001; Littell et al., 2008; Jordan et al., 2008; Behzadi and Jones, 2005; G'Sell and Souahi, 1997; Boyce and Arruda, 1990; Buckley and Harding, 2001) . Shah Khan et al. (2002) and Chen et al. (2002) observed five distinct stages in the compressive stress strain behavior of some polymer materials. These are linearly elastic, nonlinearly elastic, yield-like (peak) behavior, strain softening, and nearly perfect plastic flow.

Table 2.1 summarizes findings from these experimental studies conducted over the last decade. Chou et al. (1973) studied the stress strain compression behavior of polymethyl methacrylate, (PMMA), cellulose acetate butyrate, polypropylene, and nylon 66 over a wide range of strain rates using a medium strain rate machine and a split Hopkinson pressure bar (SHPB). Small specimens like rigid rods of ASTM standard D-

638 of Epon 862 epoxy resin were tested by Littell et al. (2008) for tension, compression, and shear at different strain rates and temperatures using optical measurement techniques. Gilat et al. (2007) used small dog-bone shaped specimens with uniform thickness and reduced thickness for tension and shear tests to generate data for E-862 and PR-520 model verifications. Strain gages were used in this study. Jordan et al. (2008) investigated compressive properties of E 826 epoxy resin cured with diethynolamine (DEA) from low to high strain rates to verify their proposed analytical model. Shah Khan et al. (2001) studied fracture mechanisms of compression samples in low and medium strain rates using small cubes of polyester and vinyl ester with a length-to-width ratio of 1:1. Chen et al. (2001) conducted high strain rate tension and compression tests on Epon 828/T-403 and PMMA using cylindrical specimens with a slenderness ratio of 0.5.

Fiedler et al. (2001) studied the yield and fracture behavior of an unreinforced epoxy resin under tension, compression, and torsion using dog-bone samples with rectangular cross sections of 0.4 mm and 1 mm thickness, and small cubes with unit aspect ratios at a strain rate of 667 μstr/sec. All the samples in these tests failed in an unstable fracture mode, and samples with 1 mm thickness failed prematurely. No post-peak behavior was captured in this study, and a maximum fracture strain of 5.8% was reported. Behzadi and Jones (2005) conducted compression tests on Araldite MY720 and Araldite MY0510 resins at various temperatures and strain rates to study the yield behavior using modified data from crosshead displacements. G'Sell et al. (2002) has determined quantitatively the influence of damage processes (crazing and cavitations) on the tensile constitutive equation and the kinetics of plastic instability. Stress drop was observed at yield and there was nearly no strain hardening in polyethylene terephtalate and high-impact polystyrene. Walley and Field (1994) studied the behavior of a large number of polymers at room

temperature and strain rates ranging from 10^{-2} s^{-1} to 10^{4} s^{-1}. They observed that the yield stress is a function of $\log(\varepsilon')$, where ε' is strain rate, and the polymers tested fell into three distinct groups: (i) a linear relationship with no change at higher strain rates such as acetal, high-density polyethylene, and dry nylon 6; (ii) a bilinear behavior with a sharp increase in gradient at a strain rate of about 10^{3} s^{-1} for polypropylene, polyvinyl chloride, and polyvinylidine fluoride; (iii) a decrease in maximum stress at a strain rate of about 10^{3} s^{-1}, possibly followed by an increase, for dry nylon 66, polycarbonate, and polyetheretherketone. Liang et al. (1996) conducted a series of experiments to examine the mechanical response of a cross-linked epoxy resin. It was observed that localization in the form of shear bands occurred under the tensile, simple shear and biaxial stress states, but not under plain strain compression. Quantitative measure of the influence of damage processes (crazing and cavitations) on the tensile constitutive equation and the kinetics of plastic instability were reported by G'Sell et al. (2002). A stress drop was observed at yield, and there was nearly no strain hardening in polyethylene terephtalate and small-sized parallel-piped high-impact polystyrene specimens. Boyce and Arruda (1990) and G'Sell et al. (2000) have shown that strain hardening of glassy polymers is interpreted in terms of entropic forces, which are necessary to orient the macromolecular chains connected by cross links or entanglement. Ballatore and Carpinteri (1999) showed that the mechanical behavior of test coupons change from ductile to brittle when the scale size is increased and the geometrical shape remains unchanged.

In the current literature there are just a few studies that include both tension and compression tests; however, many of these studies ignore the effects of strain rate. Fundamental material properties related to strength, modulus, and ductility are not measured and reported. At present, the literature shows that only one deflection

measurement tool is used without considering the accuracy of such measurement system. Strain gages and extensometers collect data at points or a very small area of the samples and may miss stress concentration areas. In a mechanical test using cross head displacement to measure strain, the mechanical response averaging over the specimen volume is taken as the point-wise material response. Averaging over a specimen that is deforming non-homogeneously especially in the plastic range will lead to excessive error.

This research uses different measurement techniques to record deflection, but focuses mainly on a non-invasive, non-contact digital image correlation (DIC) system. This method captures the surface structure of the object to be measured as images, and allocates coordinates to the image pixels. Displacement and characteristics of the object are calculated by comparing the digital images. Using the DIC system, tensile and compressive stress strain behavior of epoxy resin is investigated under a range of monotonic strain rates at room temperature. This chapter describes the results of tension and compression tests at various strain rates, ranging from 5.9×10^{-5} s^{-1} to 0.03 s^{-1} in the low and medium strain rate ranges. An attempt is made to correlate the ultimate tensile strength (UTS) point with the tensile proportionality limit point (PEL), the compressive yield stress (CYS) point with the compressive PEL point. In summary, the topics discussed in this chapter are as follows:

(a) Evaluate the effect of geometry and sample size on material behavior and the accuracy of different measurement techniques.

(b) Study the post-peak behavior of polymer material in tension and compression.

(c) Measure the fundamental material properties in tension and compression.

(d) Identify relations between mechanical properties of polymer material and strain rate.

(e) Obtain a relationship between PEL state and the peak point in tension and compression.

(f) Gather sufficient data to study the failure criteria of epoxy resin materials.

The work on tension and compression characterization is summarized in a peer reviewed journal article (Yekani Fard and Chattopadyay, 2011c).

Table

2.1 Some of Experimental Studies on Polymer Materials

Name, Year & Material	Description	Remarks
Jordan et al. , 2008, E 826	• Compression at strain rates:10^3 μstr/sec to $10^4 s^{-1}$. • Effect of temperature on compression behavior was studied at 1470 s^{-1}. • Dynamic mechanical analysis tests were conducted. • Short cylindrical specimens with 8 mm diameter and 3.5 mm height were used. • The strain was determined from actuator without any modification for compliance of machine. • The strains from medium strain rate tests (order 10 to 100 s-1) were obtained from LVDT.	• The authors assumed that there were a little difference among samples tested quasi-statically using 2:1 or 1:2 lengths: diameter ratio. • In fact, due to short length and low L/D, the stress state in the compression tests was affected by the global barreling phenomenon. • The stress strain curve from the actuator and LVDT showed the average response of the material. • Curves obtained from actuator included the compliance of the test set-up.
Littell et al., 2008, E 862	• Tension, compression, and shear tests at strain rates: 10 μstr/sec to 10^{-1} s^{-1}. • Tests were conducted from room temperature to 80°C. • Strains were measured with optical measurement system. • Tests were conducted under displacement control. • Load/unload tests were done at three strain rates and three temperatures. • Small cylindrical samples with D=3.2mm and L=3.2mm were used.	• In compression tests, due to short length and L/D equal to 1, the stress state was not uniform and was affected by global barreling.
Gilat et al., 2007, E 862 & PR 520	• Tensile and shear at strain rates: 50 μstr/sec, 2 s^{-1}, 450 and 700 s^{-1}. • Dynamic shear modulus and tensile stress relaxation (all tests at room temperature). • Tests were conducted at constant strain rate. • Dogbone samples with w=7.1 mm,	• The tensile strain determined from actuator was larger than the strain obtained from strain gauges. • Due to stress concentration effects, the tensile samples failed prematurely in the bilinear ascending portion

	t=2.8, L= 7.9mm and t=2.8, L=7.9mm, and w=7.1 to 2.8 mm were used. • The strain in the tensile tests was measured with strain gauges and through crosshead displacements.	before getting to the peak point. • Maximum strain observed was less than 9% and the brittle behavior was not the correct material behavior. • The samples with constant width were fractured in the fillet.
Behzadi & Jones, 2005, Araldite MY721 & Araldite MY0510	• Compression tests at strain rates: 167 μstr/sec to 16700 μstr/sec. • The tests were conducted at a range of temperature between 20^{o}C and 180^{o}C. • Strains were measured through the corrected readings from the actuator. • Short cylindrical specimens with 10 mm diameter and 10 mm height were used for compression tests.	• The readings from the actuator were modified assuming a constant compliance for the machine which corrected the initial slope but not the errors in the entire stress strain curve. • The stress strain curve showed the average response, not the point-wise response; therefore it could not show the non-homogeneous behavior in the plastic stage. • The stress strain curve could not be corrected due to the triaxial effect and bulging effect in samples.
Shah Khan et al., 2002, Synolite 0288-T1 (Polyester) & Derakane 8084 (Vinylester)	• Compression tests from 0.005 to 10 s^{-1}. • The specimens were 10 mm cube machined from a plate with 10 mm thickness. • Tests were conducted under displacement control and at ambient temperatures. • The strains were calculated through modified actuator readings.	• The strain was measured through modified actuator readings. • Instead of true stress strain, the nominal stress and nominal strain values were reported. • The nominal stress strain curve could not be corrected due to the triaxial effect and bulging effect in small cube samples.
Chan & Cheng, 2002, E 828, T-403 & PMMA	• Tension and compression quasi-static and dynamic tests: 110 μstr/sec to 5200 s^{-1}. • A MTS extensometer was used to measure the axial strain. • Short cylindrical specimens with 12.7 mm diameter and 6.35 mm height were used for compression tests. • Small dogbone samples with width	• Due to short length and low L/D, the stress state in the compression tests was not uniform (global barreling). • The stress strain curve showed the average response, not the point-wise response, so it could not show the inhomogeneous behavior in the plastic stage.

	of 7.65 mm and L/W ≅ 3 were used for tension tests. • Tests were conducted under displacement control and at ambient temperatures.	
Fiedler et al., 2001, Bisphenol-A	• Tension, compression, and torsion tests at constant displacement rate of 1 mm/min. • Small dogbone tensile samples with width of 5 mm, thickness of 0.4mm and 1mm and gauge length of 25 mm were tested. • For the compression tests, cubes of plain resin with lengths of 5 and 10mm were used. • The strain was measured by strain gauges. • True stress and strain were calculated.	• Due to stress concentration effects, the tensile samples failed prematurely in the bilinear ascending portion before getting to the peak point. • Maximum strain observed was less than 6%, and the brittle behavior was not the correct material behavior. • The post-peak behavior in tension was not been captured. • Due to the short length and low L/D, the stress state in the compression tests was not uniform (global barreling).
Walley et al., 1989 N6, N66, PC, Noryl, PBT, PVDF, ….	• Compression at different strain rates from 10^{-2} to 10^{4} s^{-1}. • The strain was measured with high speed photography. • The effect of different lubricants on the stress strain response was studied. • 1mm and 2mm thick cylindrical samples with D=5 mm were used.	• There was the effect of tri-axiality in the results. • Strain stiffening at high strain values was observed.

2.2. Material Composition

The materials used in this research project is the polymer Resin Epon 863 with a hardener EPI-CURE 3290 using a 100/27 weight ratio. All tests were performed at room temperature, applying a displacement control.

2.3. Specimens, Experimental Set-up, and Test Procedure

ASTM standards D638 (section 6.1, 2010), and D695 (sections 6.2 and 6.7, 2010) were considered for tensile and compressive samples, respectively. Hobbiebrunken et al. (2007) showed that the size related matrix strength is much higher than the strength obtained by standard test methods. Since it is difficult to construct thick resin sheets due to cracking, bubbling, and warping, thin polymer sheets were constructed, with samples cut and machined from these sheets. Figures 2.1 and 2.2 and Tables 2.2 and 2.3 illustrate the dimensions of tensile and compressive samples used. 4mm cubes (type C_1), right square-sided prisms (type C_2) with a length of 8 mm and a side of 3.5 mm and cylinders (type C_3) with a length of 10 mm and diameter of 4 mm were used for compression tests. Results of these tests show the effects of triaxiality of state of stress and the cross section shape on the stress strain response. Dogbone samples were used for the tension tests. The length to width ratio of the strain gage area of all tensile dogbone samples was greater than four to achieve a uniaxial state of stress.

The symbolic notation X_Y-Z has been used to describe the test and sample types in this dissertation. “X” denotes the type of the test (T: tension, C: compression), “Y” denotes the type of sample in each type of test. “Y” in tension is 1, 2 and 3 with detailed explanations provided in Fig. 2.1 and 2.2. In compression, “Y” is 1 for cubic samples, 2 for right square-sided prismatic samples, and 3 for cylindrical samples. Tension sample type one (T_1) with almost a square shape cross section was used for monotonic tests

with different strain rates. Tension sample type two (T_2) with a rectangular cross section was used for monotonic tests, and type three (T_3) was used for relaxation tests at strain levels lower than the UTS point. Trial tests showed that it is not possible to obtain the entire tensile response on the T_3 specimens, and thinner specimens must be used to prevent any premature failure due to cracking and bubbling in thicker samples. In large volume samples, the presence of severe defects (e.g., voids) is higher than in smaller volumes. It has been shown that the mechanical behavior of test coupons changes from ductile to brittle when the size scale is increased while the geometrical shape remains unchanged (Ballatore and Carpinteri, 1999). In Tables 2.2 and 2.3, SA is the surface area, r is the radius of gyration equal to $(I/A)^{0.5}$ where *I* and *A* are moments of inertia and area of the cross section, respectively, and *L/r* is the slenderness ratio.

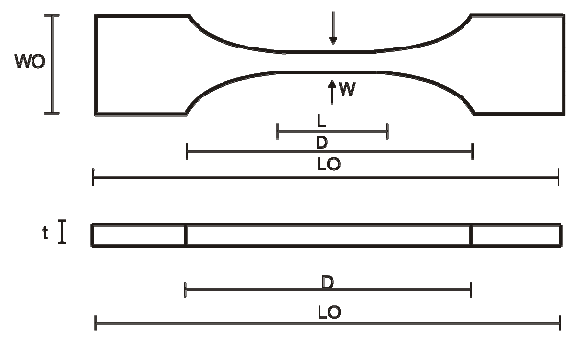

(a)

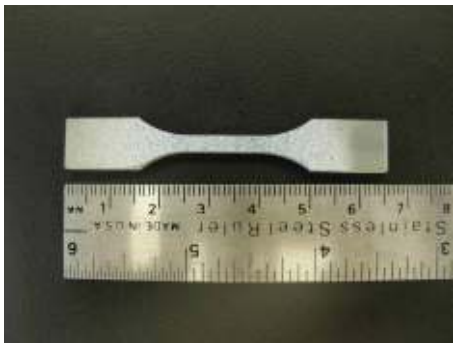

(b)

Fig. 2.1 Dogbone samples for tension tests

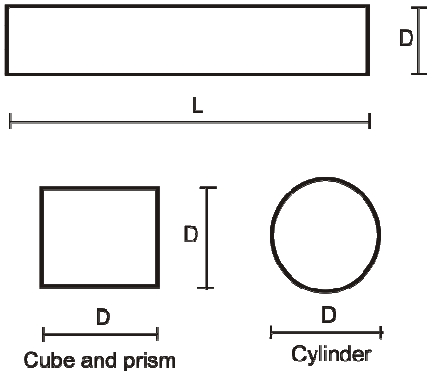

(a)

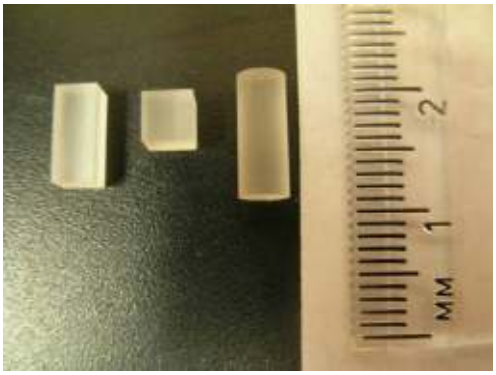

(b)

Fig. 2.2 Cylindrical, cubic and prismatic compression samples

Table

2.2 Average Dimension of Tensile Samples

Type	T (mm)	W (mm)	WO (mm)	L (mm)	LO (mm)	D (mm)	L/W	WO/W	SA/V (1/mm)
one	3.18	3.43	9.74	14	63.84	33.84	4.08	2.84	0.95
two	3	13	19	55	165	100	4.23	1.46	0.8
three	6	6	19	57	183	118	9.5	3.17	0.52

Table

2.3 Average Dimension of Compression Samples

Type	D (mm)	L (mm)	SA (mm^2)	V (mm^3)	L/D	L/r	SA/V (1/mm)
One, cube	4	4	96	64	1	3.47	1.5
Two, prism	3.5	8	136.5	98	2.29	7.92	1.39
Three, cylinder	4	10	125.66	125.66	2.5	10	1

The ARAMIS 4M (2006), a 3D digital image correlation (DIC) system that enables non-contact measurement of displacement and strain fields, is particularly suitable for three-dimensional deformation measurements under static and dynamic loading. It is possible to obtain the true tensile and compressive stress strain relationship using a DIC system because it is capable of capturing loads off of the test frame and recording the loads in an output file. A random speckle pattern is applied on the surface of the samples using an opaque white and black color spray. Stochastic spray patterns are critical in tracking the displacements of the speckled dots, especially in small cubic and cylindrical samples. A picture of the test setup is shown in Fig. 2.3. An interface load cell (interface model SM-1000) was used to measure the axial load. A MTS extensometer (model MTS 634-12E-24), strain gages (model SGD-3/120-RYB23), and ARAMIS 4M were used to calculate the axial strain. As extensometers and strain gages are still among common devices to measure deformation and strain in material characterization studies (Gilat et al. 2007; Chen et al. 2001), they were used in some of the tensile tests in this study to compare stress strain curves with curves obtained from the DIC system. True tensile or compressive stresses were determined assuming isochoric deformation. The longitudinal true strain along the sample and major/minor true strain were calculated by taking the average value of nine stage points in the highest strain region. The true stress (Cauchy stress) was calculated at each stage of loading taking into account the reduction/increase of the cross-sectional area (through DIC system) that the specimen undergoes while it is stretched and compressed. The true strain, ε_{tr} is determined from the displacement or engineering strain as

$$\varepsilon_{tr} = \ln\left(\frac{L_i}{L_t}\right) = \ln\left(1+\varepsilon_e\right) \tag{2.1}$$

where, L_i and L_t are initial and instantaneous lengths respectively, and ε_e is defined as the nominal engineering strain. The true stress, assuming a constant volume deformation is defined as

$$\sigma_{tr} = \frac{F}{A_0 \exp(\varepsilon_{tr})} = \sigma_e (1 + \varepsilon_e) \tag{2.2}$$

where A_0 is the initial cross-sectional area, F is load, and σ_e is the nominal engineering stress.

Fig. 2.3 Equipment set-up in tension and compression tests

In order to study the strain rate effect on mechanical behavior, displacement rates as shown in Table 2.4 were used. Samples T_1-1 to T_1-8 and T_2-1 to T_2-4 are from one cast resin plate (PL 1), and samples T_1-11, T_1-12, T_1-14 to T_1-17, and T_3-1 to T_3-2 are from the second cast resin plate (PL 2). The remaining samples are from the third cast resin plate (PL 3).

Table

2.4 Experimental Tension and Compression Tests Plan

Sample type	Sample No.	Monotonic (μstr/sec)	Type of Load Frame	relaxation	measuring tool
T_1	1-8	493	Dual	-	Ex, Ac

T_1	11-12	493	MTS 4411	-	Opt
T_1	14-17	59	MTS 4411	-	Opt
T_2	1-4	833	Bionix	-	Sg, Ac
T_3	1-2	-	MTS 1331	1% strain	Op, Ac
C_1	1-2	493	Syntech 1/S	-	Op, Ac
C_1	3, 7-8	10^4	Syntech 1/S	-	Op, Ac
C_1	4-6	10^3	Syntech 1/S	-	Op,Ac
C_1	9-10	3×10^4	Syntech 1/S	-	Op, Ac
C_2	1-2	493	Syntech 1/S	-	Op, Ac
C_2	3,5-7	10^3	Syntech 1/S	-	Op, Ac
C_2	4,8-9	10^4	Syntech 1/S	-	Op, Ac
C_2	10-11	3×10^4	Syntech 1/S	-	Op, Ac
C_3	1-2	493	Syntech 1/S	-	Op, Ac
C_3	3-4	10^3	Syntech 1/S	-	Op, Ac
C_3	5	10^4	Syntech 1/S	-	Op, Ac

Ex: extensometer, Ac: actuator, Sg: strain gage, Op: optical system

2.4. Tension Results

Experimental results clearly captured some of the fundamental features of the tensile true stress strain behavior of polymers. All the tests were run until failure of the samples occurred. Dogbone specimens specified as type 1 (T_1) were used in tests with the DIC system and extensometers. Dogbone specimens, shown as type 2 (T_2), were used in tests where the strain was measured with strain gages. Dogbone specimens shown as type 3 (T_3) were used in tensile relaxation. Table 2.2 shows the average dimensions of different tensile samples. Figure 2.4 shows an ascending curve, which is bilinear, starting from 0 to proportionality limit state point (PEL), defined as the point at which deviation is observed in the linear part of stress strain curve, and from PEL to the ultimate tensile

strength (UTS) in the pre-peak region. Post-peak response includes strain softening followed by nearly perfect plastic flow, which is a plateau with almost constant flow stress and strain hardening behavior in some cases up to ultimate tensile strain. Contrary to other glassy polymers for which a nearly constant flow true stress has been recorded (G'Sell et al. 2002), Epon E 863 shows some hardening before failure. The premature failure of specimens at 4% strain due to the stress concentration at the location of strain gauge is shown in Fig. 2.5. This observation indicates that stress concentration plays a role in the type of fracture and may overshadow the strain rate effect on the ultimate tensile stress and the overall response of the material. Gilat et al. (2007) also observed the effect of strain gage on the premature failure in characterization of E 862.

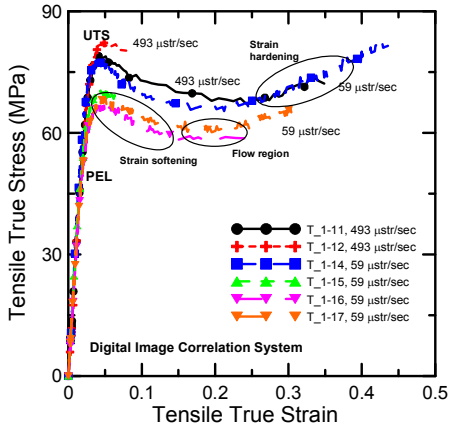

Fig. 2.4 Stress strain response of samples type 1 using DIC system

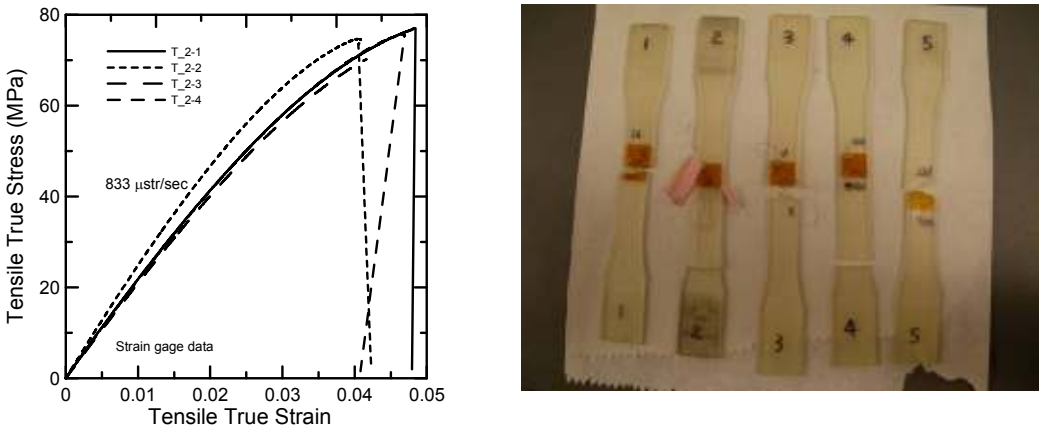

Fig. 2.5 Stress strain response of samples type 2 with strain gage at 833 μstr/sec

The complete stress strain response of the material, including the softening response and flow stress, is necessary for constitutive modeling. Figure 2.6 (a) shows the stress strain curve obtained from the extensometer showing that the maximum strain averaged in the gage length is around 15%. It must be noted, as mentioned before, strain gages and extensometers only collect data at specific points or over a very limited area in a sample. These measurement techniques may miss areas of stress concentrations. Averaging the strain over a specimen that is deforming in homogeneously particularly in the plastic range does not capture the post-peak response accurately, as shown in Fig. 2.6 (b). Load deflection history, which is measured through the loading mechanism of the test frame, is affected by extraneous deformations associated with machine compliance in the elastic range. The magnitude of this error depends on the compliance of the test frame and the magnitude of applied load. The stress strain curve obtained from cross-head data shows the average mechanical response over the specimen volume. Mechanical characteristics of tensile samples obtained from the DIC system are shown in Table 2.5. The summarizes the obtained ultimate stress and strain (σ_{UTS}, ε_{UTS}), proportionality elastic limit stress and

strain (σ_{PEL}, ε_{PEL}), strain at failure or strain capacity (ε_f), and modulus of elasticity E for different nominal strain rates.

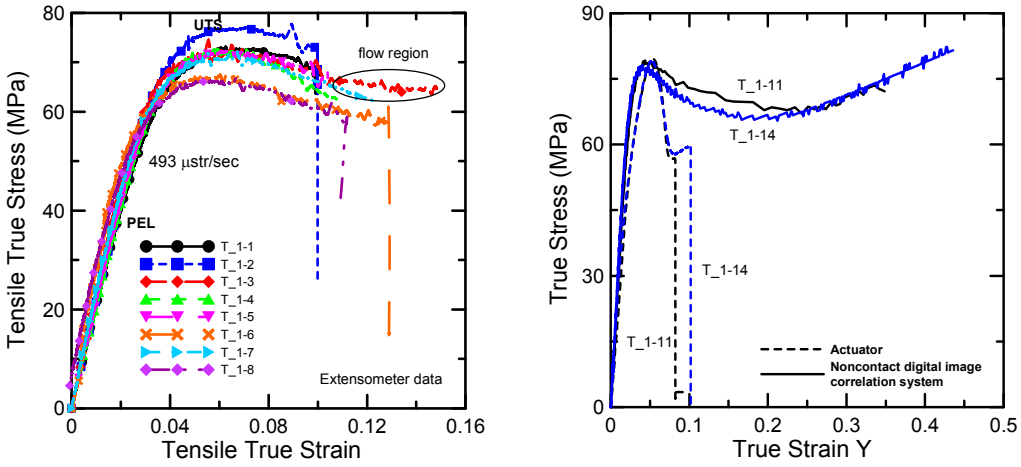

(a) (b)

Fig. 2.6 (a) Stress strain response of samples type 1 with extensometer at 493 μstr/sec; (b) Comparison of stress strain response obtained from actuator and DIC system

The tensile Young's modulus was measured as the slope of the stress strain curve in the linear region between 0.3% and 1.4%. Results indicate that the average ultimate tensile strength of the material under higher strain rates is higher than its lower strain rate counterpart (~ 81MPa compared with ~ 72MPa). Figure 2.7 shows a representative sample taken by the left and right cameras just before failure. Necking was observed in samples T_1-11, T_1-14, T_1-16, and T_1-17, while crazes were observed in samples T_1-12 and T_1-15. Samples were fractured in crazes after the peak stress and at the start of softening, with failure strain around 8%. The low strain at fracture in crazes in samples T_1-12 and T_1-15 has influenced the failure strains in Table 2.5. Kramer (1983) also studied the phenomenon of crazing in glassy polymers, which represent an important

class of damage mechanisms. The interaction between the two modes of failure, plastic instability and brittle fracture due to unstable crack growth shown in Fig. 2.8 and 2.9, indicates that the mode of failure in tension cannot be identified for Epon E 863.

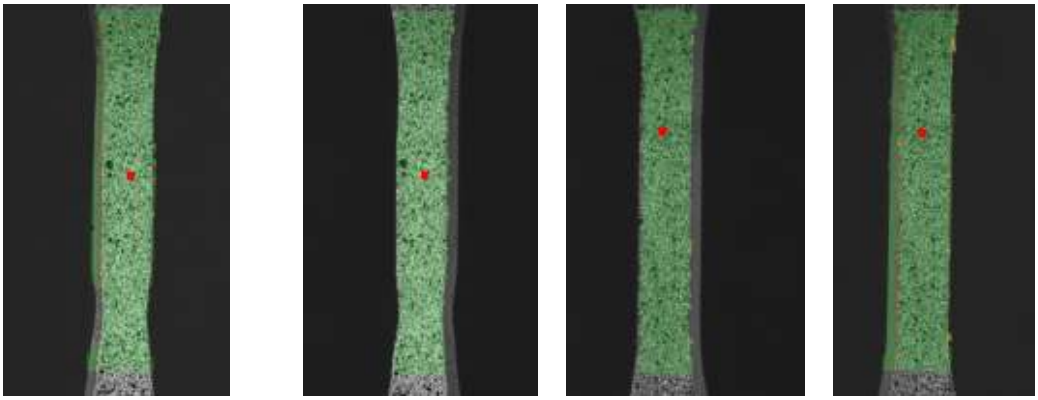

(a) (b)

Fig. 2.7 (a) Necking in sample T_1-11 at 41% strain before fracture; (b) Crazing in sample T_1-12 at 8% strain before fracture

Figure 2.8 shows the longitudinal strain distribution and the location of high strain corresponding to necking. The strain distribution is affected in the softening regime where a high degree of nonlinearity exists. Deformation is seen to localize in fine shear bands that grow and multiply within the neck. The necking of the specimen causes nonuniform strain and stress distributions in the remaining cross section. Under uniaxial tension, plastic instability is nucleated after the yield point due to softening, while neck propagation is favored by increasing hardening at large true strains (20%), as shown in Figs. 2.4 and 2.8 (sample T_1-11). Figure 2.9 shows the nonsymmetrical distribution of the major strain in stage 131 corresponding to the peak stress area. It is clear that crazes start from one edge near the top of the strain gage area in planes, whose normal is in the direction of tensile stress. The main reason for this phenomenon is probably stress

concentration near the free surface where plane stress governs. The type of fracture and failure mode affects the strain at failure. The ultimate strains for crazing and necking types of failure are around 8% and 35%, respectively. Results obtained from the digital image correlation system show that increasing strain rate increases UTS around 7% and slightly increases the initial elastic modulus.

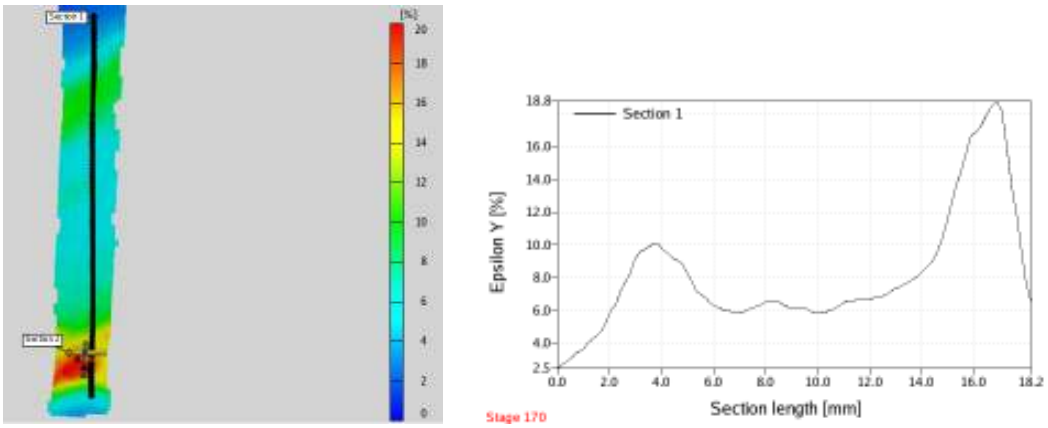

Fig. 2.8 Distribution of ε_y in necking in stage 170 out of 190 in sample T_1-11

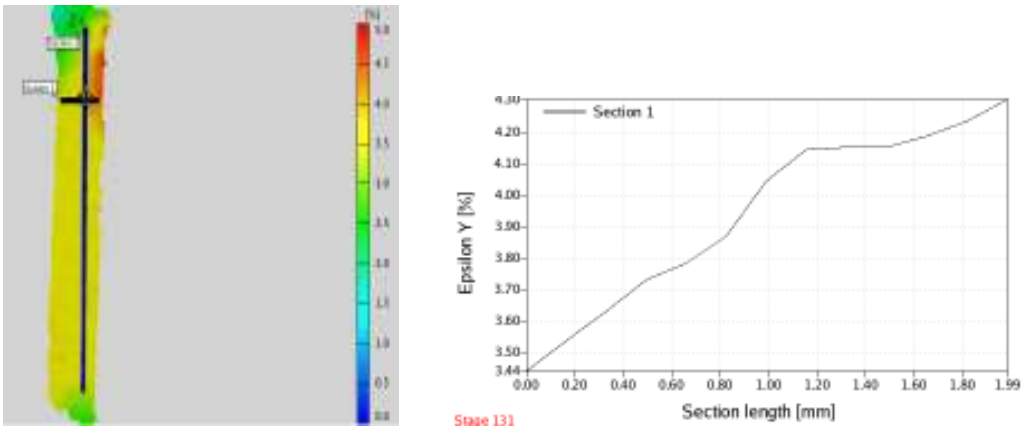

Fig. 2.9 Major strain distribution in stage 131 out of 150 in T_1-12 fractured in crazes

In the low and very low strain rate tests, the shape of the stress strain curve could be affected by stress relaxation during the test. As the displacement is constant during stress relaxation and the time of the relaxation phase is much higher than the first loading phase, the relaxation tests are independent of the strain rate effects. However, stress relaxation effects could be different for different levels of strains. Figure 2.10 displays the effect of stress relaxation on material response for a T_3 sample. It illustrates that strength at the linear elastic region decreases as much as 15% in almost 40 minutes. The duration of low strain rate tests are high enough for stress relaxation to occur. The attempts to separate the effect of viscoplasticity and plasticity on material behavior, specifically at low strain rates, have not been successful thus far. Further investigations for validation of this effect and reversibility through unloading-reloading tests are required in the future.

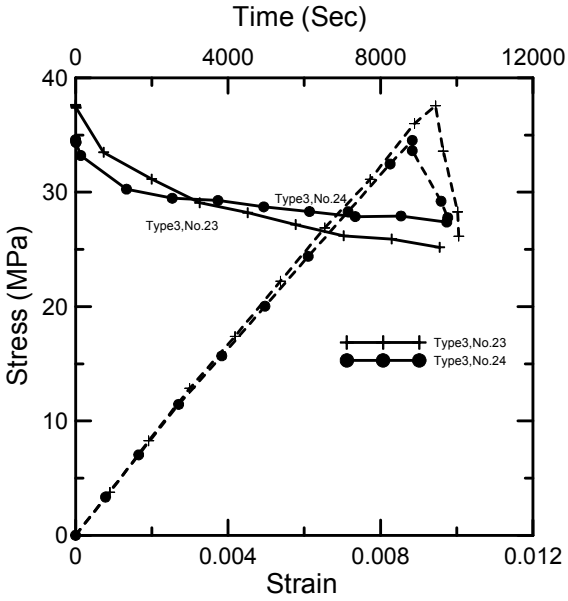

Fig. 2.10 Stress relaxation at PEL level and at room temperature

Table

2.5 Mechanical Characteristics of Epon E 863 Tensile Samples

Sample	Average Elasticity Modulus (MPa)	Average Slope of Post PEL (MPa)	UTS (MPa)	Strain at UTS (%)	PEL (MPa)	Strain at PEL (%)	Strain Capacity (%)
T_1-1	1970	721	73.0	6.25	44.0	2.23	9.92
T_1-2	2075	822	76.7	5.80	48.0	2.31	10.0
T_1-3	2240	878	74.5	5.56	42.2	1.88	14.86
T_1-4	2002	727	72.6	5.93	46.2	2.30	10.76
T_1-5	2100	907	71.8	5.36	40.7	1.93	10.4
T_1-6	2690	567	67.4	6.00	42.3	1.57	12.9
T_1-7	2230	695	72.6	6.68	38.0	1.70	13.1
T_1-8	2402	932	65.6	4.79	34.2	1.42	13.3
average	2214	781	71.8	5.80	42.0	1.92	11.9
T_1-11	3049	1203	79.6	4.13	49.4	1.62	34.9
T_1-12	3113	1365	82.4	4.00	49.5	1.59	7.90
average	3081	1284	81.0	4.07	49.45	1.61	21.4
T_1-14	3290	1225	78.9	3.54	56.6	1.72	43.6
T_1-15	3030	1084	71.5	4.28	39.0	1.28	7.00
T_1-16	2680	878	67.9	4.13	47.0	1.75	25.9
T_1-17	2877	948	69.9	4.24	44.3	1.54	30.6
average	2969	1034	72.0	4.13	46.7	1.57	26.8
T_2-1	2055	1267	77.06	4.8	39.9	1.91	4.84
T_2-2	2379	1469	74.7	4.06	38.4	1.59	4.23
T_2-3	1951	1255	70.2	4.16	48.4	2.43	4.2
T_2-4	2069	1299	75.7	4.67	39.4	1.87	4.70
average	2113	1323	74.42	4.43	41.63	1.95	4.49

2.5. Compression Results

In order to develop constitutive relations for epoxy resins under different kinds of loading conditions, strength, ductility, and the stress strain curve of the specimen should be independent of geometrical shapes. The quasi-static compressive test results on cubic, prismatic, and cylindrical samples are shown in Figs. 2.11- 2.13. The figures clearly show the fundamental features of the compressive stress strain behavior of epoxy resin samples with different geometries. These discrete features can be captured by a bilinear ascending curve starting from 0 to proportionality limit state point (PEL) and from PEL to the compressive yield strength (CYS) in the pre-peak region. Post-peak response includes strain softening followed by a nearly perfect plastic flow, which is a plateau with either nearly constant flow stress or a small softening slope up to ultimate compression strain in prismatic and cylindrical samples. Post-peak response in cubic samples includes strain softening followed by small plastic flow and strain hardening, and up to ultimate compression failure. Figure 2.12 indicates the relative increase in strength with increasing rates of loading. Figures 2.12 and 2.13 show that there is no significant difference in the flow stress beyond the CYS point at different strain rates. The results clearly illustrate that prismatic and cylindrical samples are capable of capturing the material behavior, confirming the strain softening phenomenon followed by a stress flow plateau and failure.

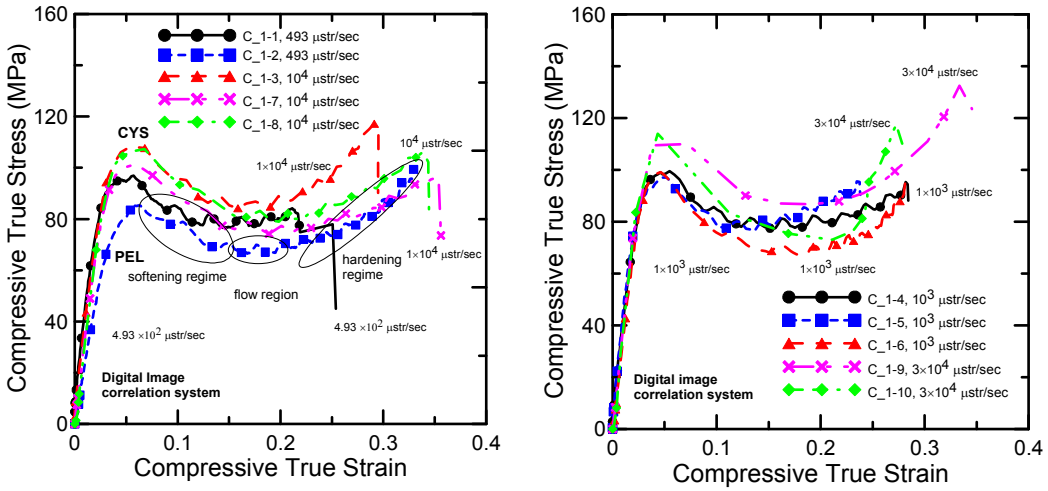

Fig. 2.11 Stress strain response of cubic samples using DIC

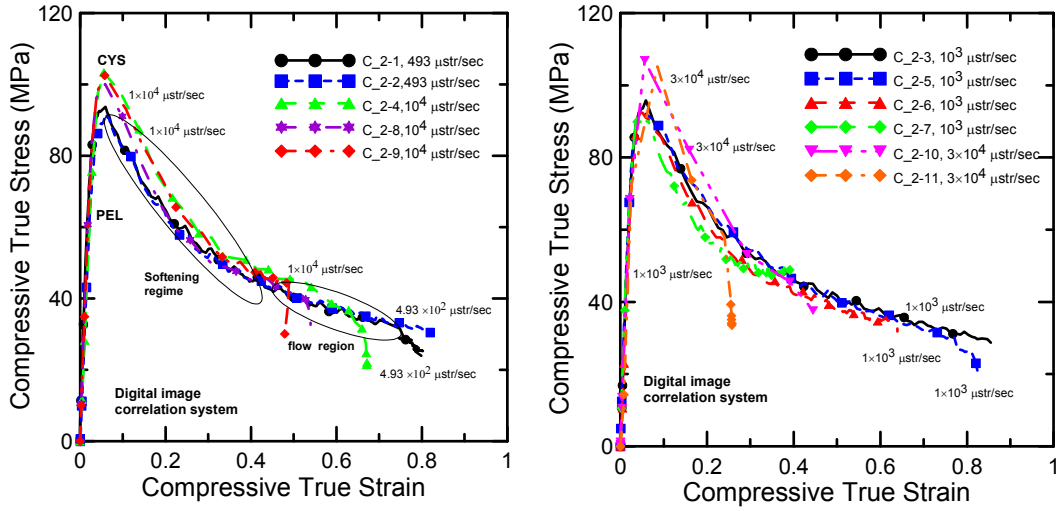

Fig. 2.12 Stress strain response of prismatic samples using DIC system

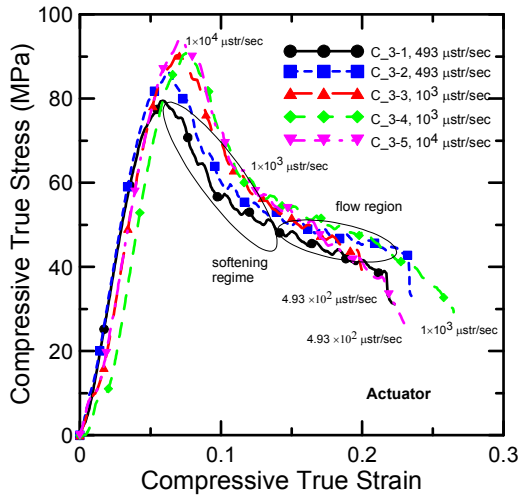

Fig. 2.13 Stress strain response of cylindrical samples using cross-head data

The compressive results of monotonic tests show some similarities and differences among sample types 1, 2, and 3. Cubic samples increase their cross section as shown in Fig. 2.14. Frictional forces hinder the outward deformation of the resin close to the compression anvils while the material at the center height can deform unconstrained in the outward direction. This leads to a barrel-like specimen profile. Plastic deformation followed by barreling in cubic specimens has been observed in other studies (Littell et al. 2008; Shah Khan et al. 2001; Fiedler et al. 2001). Cone-shaped areas produce a tri-axial state of stress in the epoxy resin close to the grip surface, therefore the pure uniaxial compressive properties cannot be measured when these cone-shaped regions are relatively large compared to the sample's size. After reaching the compressive yield stress, the cubic samples show a further increase in stress with applied strain and can reach a failure stress higher than their yield stress as shown in Fig. 2.11. In prismatic and cylindrical samples, the shape after the test is not barrel-like, and a pure uniaxial compressive state of stress can be measured due to minimum constrained areas. Figure

2.15 shows a uniform strain distribution in the bottom half of the samples. Also, it shows symmetric longitudinal strain distribution in prismatic samples.

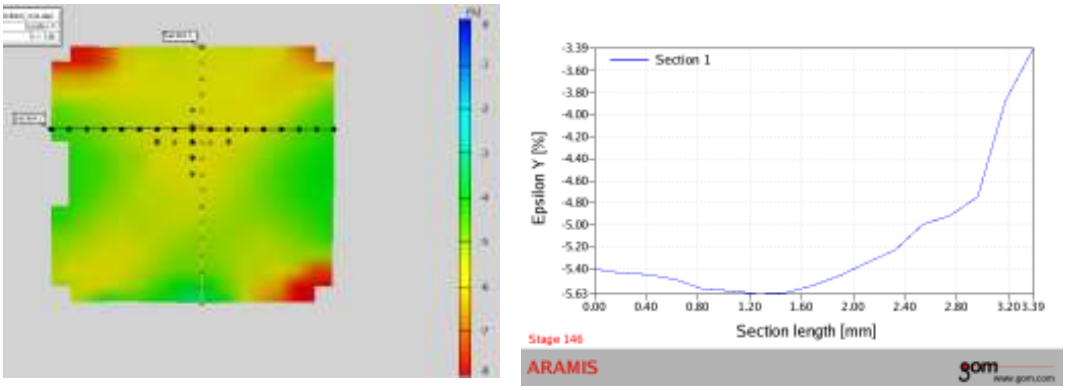

(a) (b)

Fig. 2.14 (a) Distribution of longitudinal strain in stage 146 out of 277 and the location of stage points in sample C_1-1 at 493 µstr/sec; (b) Distribution of longitudinal strain along a vertical section showing the effects of tri-axial state of stress

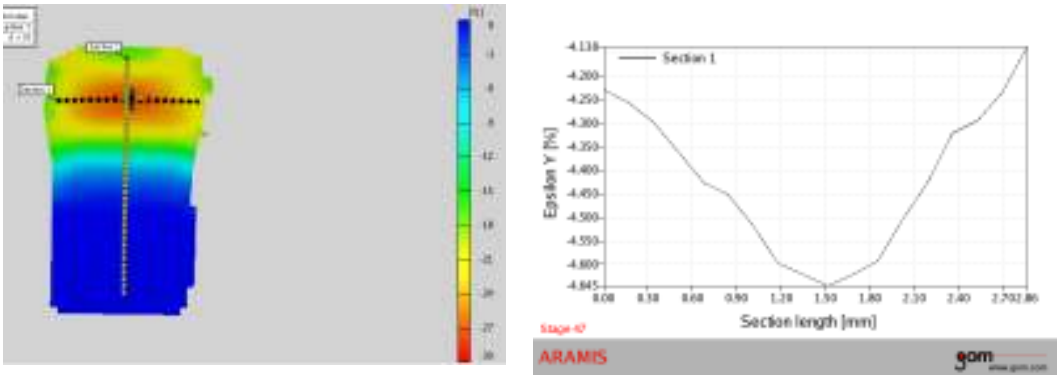

(a) (b)

Fig. 2.15 (a) Distribution of longitudinal strain in stage 47 out of 131 and the location of stage points in sample C_2-5 at 1000 µstr/sec; (b) Distribution of longitudinal strain along a vertical section

Table 2.6 summarizes the values of yield stress and strain (σ_{CYS}, ε_{CYS}), proportionality elastic limit stress and strain in compression ($\sigma_{PEL,c}$, $\varepsilon_{PEL,c}$), failure strain ($\varepsilon_{f,c}$), and modulus of elasticity E for all samples at different nominal strain rates. All compressive test specimens show a nonlinear material behavior and a considerable amount of plastic deformation. Results indicate that the compressive yield strength of the material under high strain rates is much higher than its low strain rate counterpart. In cubic samples, the average CYS is 91.2 MPa at 493 μstr/sec and 111.9 MPa at 3×10^4 μstr/sec. Results for the cubic samples show an increase of around 40% in initial elastic modulus. The cubic tests were stopped before failure as they showed a further increase in stress with applied strain due to global barrel-like behavior. The increase in strength and stiffness for higher strain rates in prismatic samples was less than that observed in cubic samples. The CYS and initial elastic modulus increased by 13% and 5%, respectively. All the tests show a considerable shift in the entire stress strain curve with increase in strain rate. The same trend was observed in other resins (Shah Khan et al. 2001). The average failure strain in prismatic samples was 81.3% at 493 μstr/sec and 35.05% at 3×10^4 μstr/sec, which shows an approximate reduction of 50%. Compared to failure strain, strain values at the PEL and CYS points did not show a considerable change due to changes in speed of loading. Thus, it can be concluded that increasing speed of loading, considerably decreases displacement ductility. The ratio of post-PEL slopes to the initial elastic modulus in all the tests were between 25% and 40%.

Tracking the displacement of the speckled dots in the cylindrical samples was not conducted because of the small size and geometry of the samples, and the limited nature of the lenses in the instrumentation available at the time of this research. The characteristics of the stress strain curves for the cylindrical samples were not included in

Table 2.6 due to the existing errors in cross-head data. Deflection data measured from cross-head movements is affected by unknown extraneous deformations associated with the machine's compliance. Also, the stress strain curves obtained from cross-head data show the global mechanical response over the specimen volume between the grips. Figure 2.16 illustrates the effect of extraneous deformations associated with the compliance of the machine in the elastic range on the stress strain response. Averaging the strain over a nonlinearly deforming specimen could not show the post-peak response accurately. This fact can significantly change the initial elastic modulus of the sample.

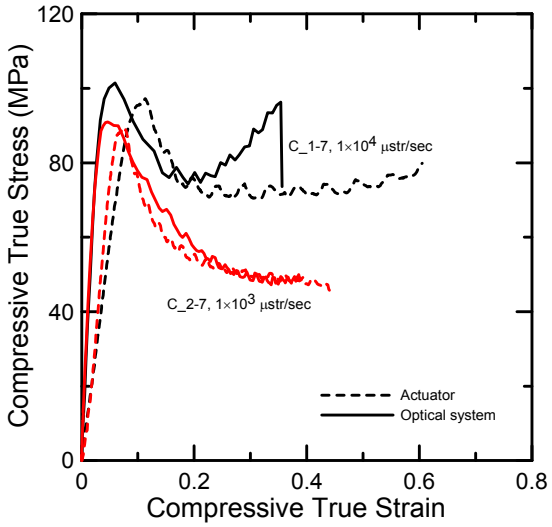

Fig. 2.16 Cubic and prismatic sample responses from ARAMIS & actuator readings

A comparison of the average mechanical properties of compression and tension stress strain curves at 493 μstr/sec shows that Epon E 863 is stronger in compression than in tension. The average CYS is around 92 MPa while the average UTS value is 81 MPa.

Table

2.6 Mechanical Characteristics of Epon E 863 Compressive Samples

Sample	Average Elasticity Modulus (MPa)	Average Slope of Post PEL (MPa)	CYS (MPa)	Strain at CYS (%)	PEL (MPa)	Strain at PEL (%)	Strain Capacity (%)
C_1-1	3330	930	96.9	5.72	61.0	1.86	25.4
C_1-2	2375	790	85.4	6.17	55.0	2.32	32.9
average	2853	860	91.2	5.95	58.0	2.09	-
C_1-3	3453	998	107.7	6.80	56.0	1.62	29.86
C_1-7	3508	1039	101.5	5.94	56.5	1.61	35.6
C_1-8	3639	894	107.3	6.77	62.0	1.70	34.4
average	3533	977	105.5	6.5	58.2	1.64	-
C_1-4	3424	1064	99.41	5.48	59.5	1.73	28.43
C_1-5	3415	1190	97.07	5.20	54.0	1.58	23.80
C_1-6	3594	1439	99.1	4.62	54.50	1.52	28.10
average	3477	1331	98.5	5.1	56.0	1.61	-
C_1-9	3936	744	109.9	7.15	70.0	1.78	34.5
C_1-10	4231	1409	113.95	4.34	79.0	1.86	28.0
average	4084	1077	111.9	5.74	74.5	1.82	-
C_2-1	3351	848	93.69	5.94	58.0	1.73	79.9
C_2-2	2934	819	91.67	6.05	58.50	2.0	82.6
average	3143	834	92.68	6.0	58.25	1.87	81.3
C_2-3	3165	905	95.8	5.89	59.5	1.88	85.4
C_2-5	3193	1180	93.6	4.72	60.1	1.89	82.4
C_2-6	3290	1041	92.40	5.13	57.0	1.73	63.9
C_2-7	3085	724	90.0	6.49	56.2	1.82	39.3
average	3183	963	93.0	5.56	58.2	1.83	67.75
C_2-4	3039	1145	103.30	5.58	63.0	2.06	67.1

C_2-8	3327	860	100.6	5.85	67.5	2.0	54.0
C_2-9	3284	1079	102.49	5.77	60.0	1.83	48.9
average	3217	1028	102.1	5.73	63.5	1.96	56.7
C_2-10	3147	1091	104.4	5.61	65.0	2.0	44.4
C_2-11	3468	564	105.2	8.54	69.1	1.99	25.7
average	3308	828	104.8	7.08	67.05	2.0	35.05

2.6. Mechanical Characteristics and Strain Rate

The obtained results and the average values of mechanical properties from the work of Littell et al. (2008) and Jordan et al. (2008) were used to study the effect of strain rate on the mechanical properties of epoxy resin. Figure 2.17 shows the variation of PEL, CYS, and UTS with logarithmic strain rate for different resins. Results show that the peak stress in tension and compression (UTS and CYS) increases with increase in the strain rate in all types of epoxy resins and in all types of specimens. The increase in CYS for the prismatic sample of Epon E 863 is less than the increase in cubic samples. The increase for Epon E 826 occurred bi-linearly; a linear increase in low and medium strain rate up to 1 s^{-1} and a sharper linear increase between 1 s^{-1} and 10^4 s^{-1}. Generally, PEL stresses in tension and compression in all types of specimens were found to be relatively less sensitive to strain rate. Figure 2.17 indicates that compressive PEL stress in Epon E 862 decreases slightly by increasing strain rate and then it increases. It is to be noted that there are no data available in strain rates higher than 0.03 s^{-1} and 0.1 s^{-1} for E 863 and E 862, respectively. Figure 2.18 (a) illustrates the effect of increasing strain rates on the modulus of elasticity of three epoxy resins. The results indicate that the modulus of elasticity increases with increasing strain rate. Foreman et al. (2010) observed that at a higher strain rate, the resin has less time to dissipate energy, and therefore, will yield at a

higher stress and has a correspondingly higher modulus. Strain rate influence on the compression failure strain of Epon E 863 is shown in Fig. 2.18 (b). Compression failure strain decreases substantially from 81.3% at 493 μstr/sec to 35.05% at 0.03 s^{-1}.

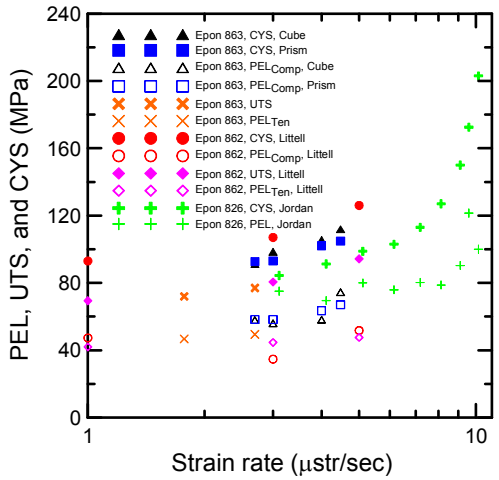

Fig. 2.17 Variations of PEL, CYS, and UTS with strain rates

Figure 2.19 compares the influence of strain rate on strains measured at PEL, CYS, and UTS points for different polymer resins. The results show no significant change in PEL strain with increasing strain rate within a single type of epoxy resin. However, the values are much higher for Epon E 826 compared to Epon E 862 and E 863. Also, strains at peak stress points in all types of epoxy resins show almost a near ascending order with increasing strain rate. The same trend has been observed on the increase in strain at yield stress (G'Sell and Souahi 1997). However, no change in strain at maximum stress with increasing strain rates was recorded in the case of vinylester resin (Shah Khan et al. 2001). In these figures, symbols enclosed in circles indicate overlapping.

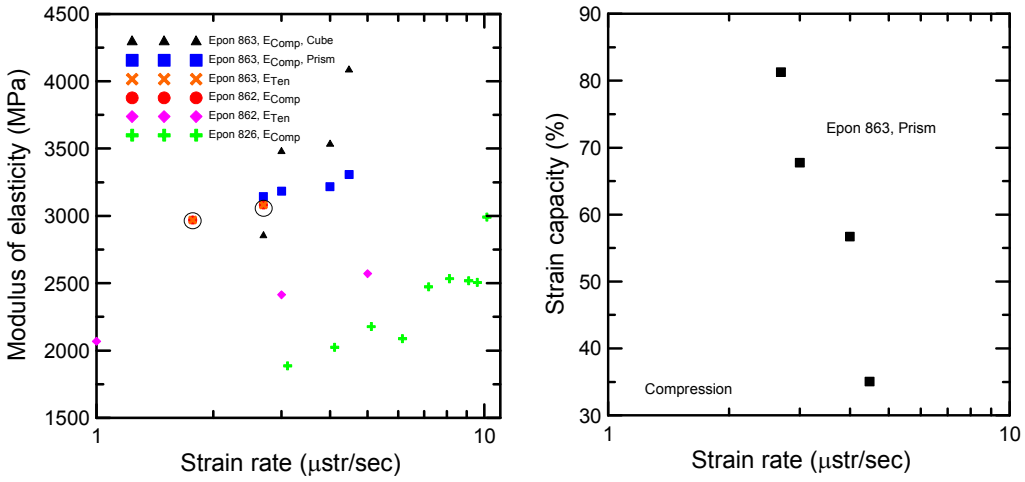

(a) (b)

Fig. 2.18 Variations of (a) modulus of elasticity; (b) failure strain with strain rates

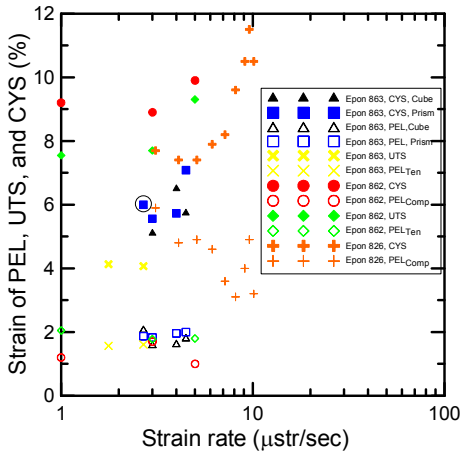

Fig. 2.19 Variations of strain at PEL, UTS, and CYS points with strain rates

2.7. Proportionality Elastic Limit and Peak Stress

Quantitative estimates of stress at the PEL point based on UTS and CYS points are presented in Figs. 2.20 and 2.21. Results in Fig. 2.20 show that PEL stress is around 59% of CYS and UTS in the strain rate range up to 0.03 s^{-1}.

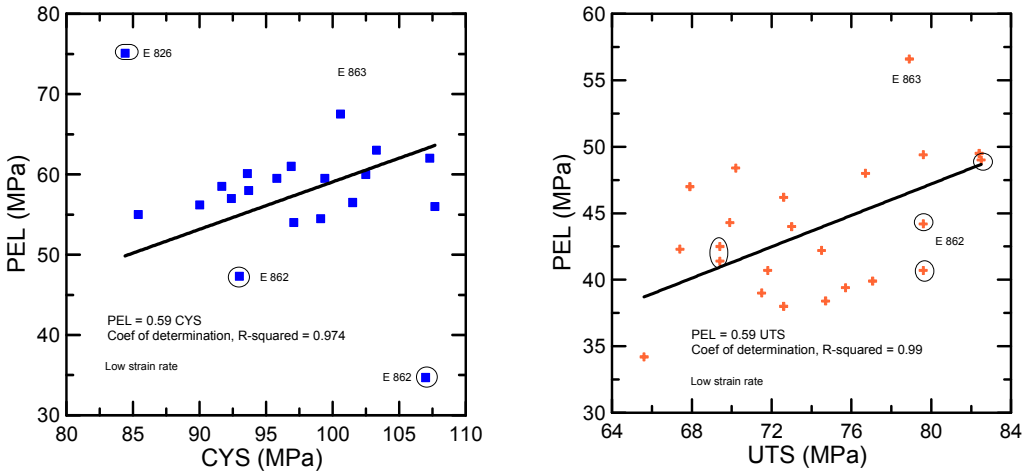

(a) (b)

Fig. 2.20 Variations of PEL with maximum stress in tension and compression for low strain rate range

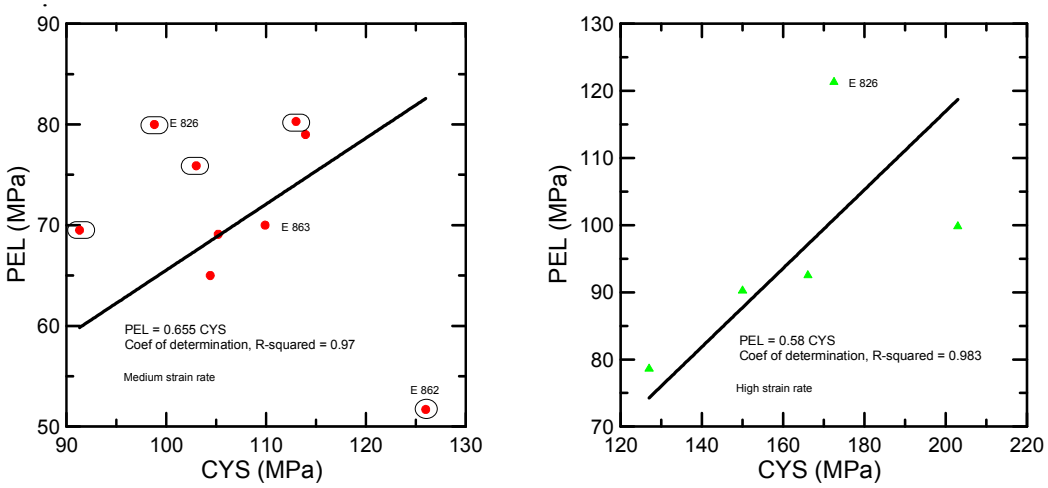

(a) (b)

Fig. 2.21Variations of PEL with CYS for (a) medium and (b) high strain rates

Figure 2.21 (a) shows that PEL is approximately 66% of CYS in the strain range between 0.03 s^{-1} and 100 s^{-1}. In the high strain rate range, PEL is around 58% of CYS as shown in Fig. 2.21 (b). Symbols enclosed in circle in Fig. 2.20 and 2.21 indicate overlapping.

2.8. Concluding Remarks

The tension and compression mechanical properties of epoxy resin with different specimen shapes and at different strain rates have been investigated. Initially, the stress strain response was found to be linear, indicating elastic behavior, followed by nonlinear plastic deformation. Plastic deformations were observed in thin samples when a non-contact technique was used for measuring deformation and strain. Epoxy resin Epon E 863 shows high failure strain in tension. However, considerable experimental scatter associated with fracture due to crazes was observed in tension samples. Failure due to crazing was observed while the material deformed plastically. Cubic, prismatic, and cylindrical samples showed different compression behavior. Cubic samples, after reaching the compressive yield stress, showed a gradual drop in the stress strain curve followed by strain stiffening at high strain values. The cubic samples reached a fracture stress higher than their yield stress. In the prismatic and cylindrical samples, the shape after the test was not barrel-like; therefore, it is correct to assume a pure uniaxial compressive state of stress due to minimum constrained areas. Results of the compression tests show that a prismatic sample with aspect ratio greater than two results in much better uniaxial compressive state of stress compared to cubic samples. An increase in the strain rate increases peak stress in tension and compression and modulus of elasticity. The strain at yield was found to be relatively less sensitive to strain rate in Epon E 863. Strain at failure of polymeric specimens decreases as speed of load increases. Results show that PEL in compression and tension could be estimated between 59% and 66% of CYS and UTS for low, medium, and high strain rates.

3. Three Point Bending (3PB) Flexural Behavior of Epoxy Resin Over a Range of Loading Rates Using Digital Image Correlation (DIC)

3.1. Introduction

In structural applications, large flexural loads are considered one of many critical loading cases considered in the design of polymer based composite structures. No study has been conducted thus far on the mechanical properties of compression, tension, and flexure of a polymer material and the relationship between the uniaxial stress strain curves and out-of-plane behavior. Additionally, there is the need to study the effect of stress gradient in tensile and compressive peak stress and the entire stress strain regime because of their importance in any analytical and numerical study. Mannocci et al. (2001) used three point bending (3PB) tests to study the different environmental and aging effects on mechanical properties of five different types of fiber posts. Fiber posts consist of fibers such as carbon, quartz, silica, or glass in a matrix based resin. Fergusson et al. (2006) used digital speckle photogrammetry techniques to study the effect of defects on flexural behavior of sandwich composite structures. Kozey and Kumar (1994), and Miwa et al. (1995) observed that the mechanical properties of similar epoxy materials can vary greatly with curing agents. Giannotti et al., (2003), and Vallo (2002) studied flexural stress of epoxy resins and PMMA materials using linear elastic formulation. In this chapter, strength and ductility of the un-reinforced epoxy resin under 3PB is investigated. A notch or groove in the middle of the beam is introduced to induce failure since the region at that location is subjected to high stress values. This makes it possible to determine the strain field at the location of the fracture using the digital image correlation (DIC) system. As stated before, DIC is a reliable technique for determining the strain field across an entire sample surface as opposed to a strain gage, and therefore is the

method employed in this investigation. Using this system, softening localization was determined, and an attempt was made to correlate the limit of proportionality (LOP) with the modulus of rupture (MOR) in flexure. The principal objectives discussed in this chapter are:

(a) Obtain the load deflection response of the flexural behavior of the epoxy resin material.

(b) Study the post-peak behavior of polymer material in flexure.

(c) Determine relations between LOP state and the MOR in the flexural response.

(d) Gather enough data to analyze the correlation between flexural strength, uniaxial tension, and compression strengths in the next chapter.

The work on flexural characterization is summarized in a peer reviewed journal article (Yekani Fard and Chattopadyay, 2011b).

3.2. Specimens, Experimental Set-up and Test Procedure

ASTM standard D790 (sections 7, 2003) were considered for the design of flexural samples. Thin polymer sheets were constructed, and samples were cut and machined from these sheets. Polymer sheets were preferred over thick resin sheets, which can crack, bubble, and warp. Flexural beams with length of 60 mm, width of 4 mm, height of 10 mm (B_1 with notch and B_1m with groove) and length of 90 mm, width of 4 mm, and height of 12 mm (B_2 with notch and B_2m with groove) were tested over a simply supported span of 50mm and 78mm, respectively. In flexural samples, the extent of deflection softening in the post-peak response was used to develop an analytical methodology for studying the stress gradient effects in epoxy resin polymeric materials. As in chapter 2, the symbolic notation X_Y-Z has been used here to describe the test and

sample types. “X” denotes the type of the test (B: bending), “Y” denotes the type of sample in each type of test. In flexure, “Y” is one of the {1, 1m, 2, 2m} where 1 and 2 refer to shorter and longer beams and “m” shows samples that originally had notches and were modified to grooves. “Z” is the serial number for identifying the samples. The geometry and dimensions of the samples and the modified samples are shown in Fig. 3.1 and Table 3.1. Bending tests were performed using a 3PB fixture, an electrical desktop testing machine, and the DIC technique (ARAMIS 4M) as shown in Fig. 3.2. An interface load cell (interface model SM-1000) was used to measure the axial load.

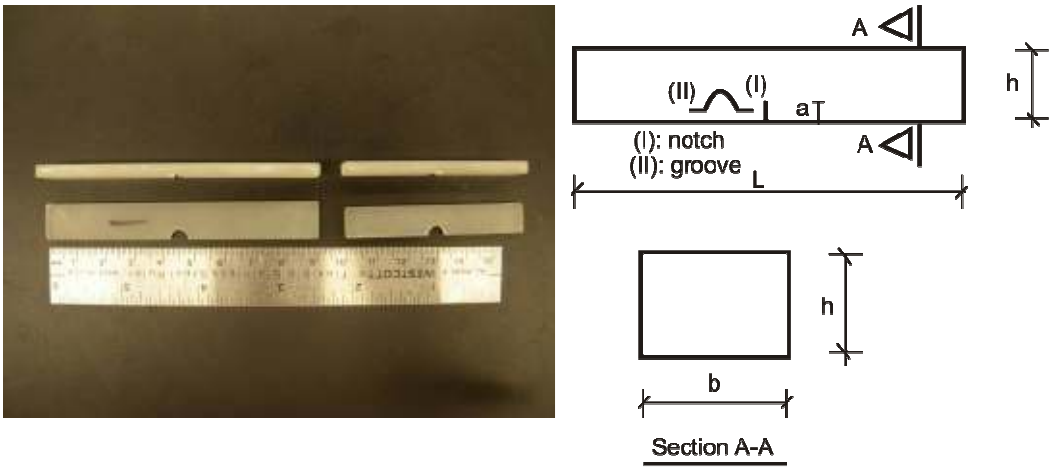

Fig. 3.1 Bending samples with rectangular cross sections

Table

3.1 Average dimension of flexural samples

Type	Initial Imperfection	b (mm)	h (mm)	a (mm)	L (mm)	S (mm)	S/h
B1,B1m	B1: notch B1m: groove	10	4	1 1.1	60	50	12.5
B2,B2m	B2: notch B2m: groove	4	10	3 3.2	60	50	5
B3,B3m	B3: notch	12	4	1	90	78*	19.5

	B3m: groove			1.1			
B4,B4m	B4: notch B4m: groove	4	12	3 3.2	90	78*	6.5

* Span is 68mm in samples B_3_1 and B_4_1.

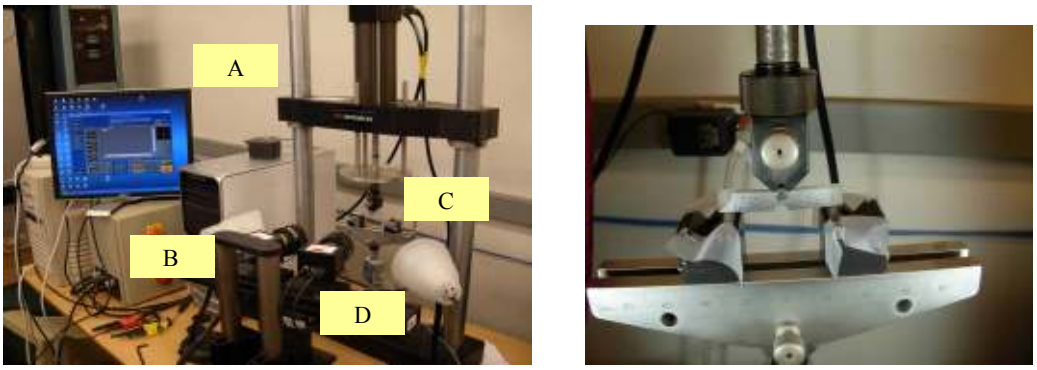

(a) (b)

Fig. 3.2 (a) Equipment setup: (A) electrical desktop machine; (B) ARAMIS; (C) 3PB fixture; and (D) interface load cell, (b) 3PB test

All tests were conducted in displacement control and ambient environmental conditions. Axial strain rates achieved ranges from 26 μstr/sec to 550 μstr/sec. Flexural tests were conducted at a nominal crosshead displacement rate. For a beam with dimensions of b (width) × h (thickness) × L (span between supports) and a notch or a small groove, the loading rates (dδ/dt) corresponding to desired strain rates were calculated approximately based on the elastic linear assumption and geometry of samples as

$$\frac{d\delta}{dt} = \frac{L^2}{6h}\frac{d\varepsilon}{dt}\left(\frac{h_1}{h}\right)^2 \tag{3.1}$$

where δ is deflection at the mid-span, ε is the axial strain, L is span, h is the thickness of the beam, h_1 is the thickness at the location of notch or groove, and dε/dt is the strain rate. The simplified form of the above equation for a beam without groove/notch is suggested by ASTM standard (2003). The loading rates corresponding to desired strain rates were calculated based on the elastic linear assumption and geometry of samples and summarized in Table 3.2.

Table

3.2 Plan for Experimental Monotonic Bending Tests

Sample type	Sample No.	Loading Speed (mm/min)	Longitudinal Strain Rate (μstr/sec)	Span (mm)	Deflection measuring tool
B_1	1	0.49	59	50	Op, Ac
B_1	2	4.11	493	50	Op, Ac
B_2	1,2	0.21	59	50	Op, Ac
B_2	3	1.76	493	50	Op, Ac
B_3	1	0.398	26	68	Op, Ac
B_3	2	1.2	59	78	Op, Ac
B_3	3	10	493	78	Op, Ac
B_4	1	0.398	78	68	Op, Ac
B_4	2,3	0.398	59	78	Op, Ac
B_1m	3	0.567	65	50	Op, Ac
B_1m	4,5	1.418	164	50	Op, Ac
B_1m	6	4.74	550	50	Op, Ac
B_2m	4	0.217	59	50	Op, Ac
B_2m	5	1.813	493	50	Op, Ac
B_2m	6	0.542	148	50	Op, Ac
B_3m	4	0.398	19	78	Op, Ac

B_3m	5	1.381	65.8	78	Op, Ac
B_3m	6	3.452	164	78	Op, Ac
B_4m	4	0.404	59	78	Op, Ac
B_4m	5,6	1.02	148	78	Op, Ac

A stochastic spray pattern was applied to the surface of the beam between two supports. This was done by first applying a white base coat with spray paint followed by a dispersion of fine black dots. The ARAMIS system and DIC technique was used, as in chapter 2, to study the displacement and strain fields. The load-deformation relationship was determined using the DIC system through a triggering option between the load cell and optical system.

3.3. 3PB Flexural Results

Beam bending theory provides a relationship between shear force and the differential of the bending moment within the beam, as well as the relationship between axial stress and applied load as shown in Equations 3.2 and 3.3 (Timoshenko and Gere, 2004).

$$V = \frac{dM}{dx} \tag{3.2}$$

$$\sigma = \frac{3PS}{2bh^2} \tag{3.3}$$

where V and M are the shear force and bending moment, respectively. P is the applied load in 3PB, S is the span of the beam, and b and h are the cross section dimensions. The shear force is constant in each half of the beam. The region with stress concentration lies directly below the loading nose due to surface

compression of the specimen by the loading nose. The bending moment would rise linearly from zero at the supports to the maximum value at the location of the loading nose. Figure 3.3 presents the deflection vs. time and load deflection curves of sample types B_1 and B_1m under monotonic 3PB test at different load speeds from 0.49 mm/min to 4.74 mm/min at room temperature. While samples B_1-1 and B_1-2 with a notch failed in the ascending part of the load deflection curve, modified samples B_1m-3, B_1m-5, and B_1m-6 with a groove failed after the modulus of rupture (MOR) point and at the start of the deflection softening regime. By comparing the deflection time curves, it is clear that samples B_1-2 and B_1m-4 failed prematurely. The same trend has been observed for bending sample types B_3 and B_3m, as shown in Fig. 3.4. A possible cause for the premature failure in samples B_1 and B_3 is the stress concentration at the location of notch, as fracture occurred along a straight line (see Fig. 3.5 and Fig. 3.6). Data of samples type 1 and 3 shows that deflection at failure in notched samples is around 60% of that in grooved samples. Figures 3.7 and 3.8 show the deflection vs. time for sample types B_2, B_2m, and B_4, B_4m, respectively. Initially, the load increases proportionally to deflection before passing through a knee point called limit of proportionality (LOP). The load keeps increasing with a reduced slope up to the maximum point known as MOR, followed by a deflection softening regime and final failure. Failure occurred in most of the samples after a considerable amount of plastic deformation.

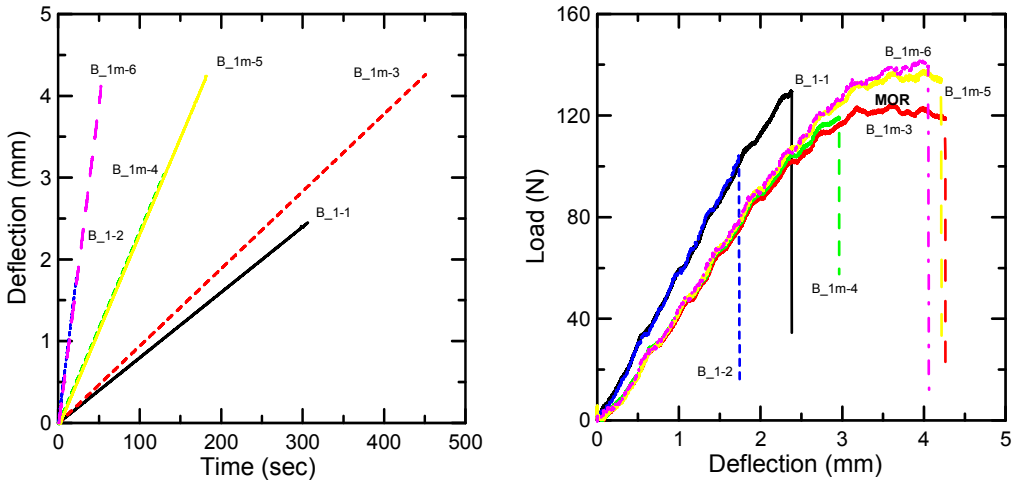

(a) (b)

Fig. 3.3 Deflection vs. time and load deflection for sample types B_1 & B_1m

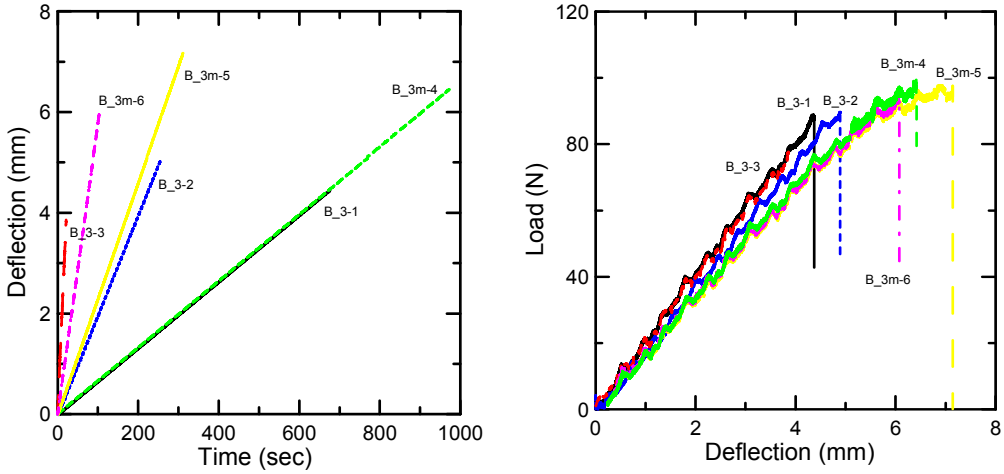

(a) (b)

Fig. 3.4 Deflection vs. time and load deflection for sample types B_3 and B_3m

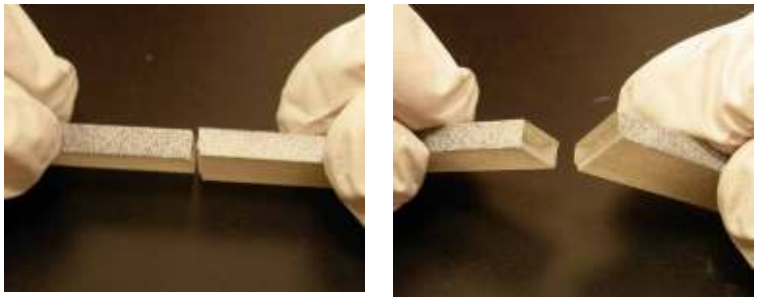

(a) (b)

Fig. 3.5 Fracture surface of the broken sample B_1-2

(a) (b)

Fig. 3.6 Fracture surface of the broken sample B_3-3

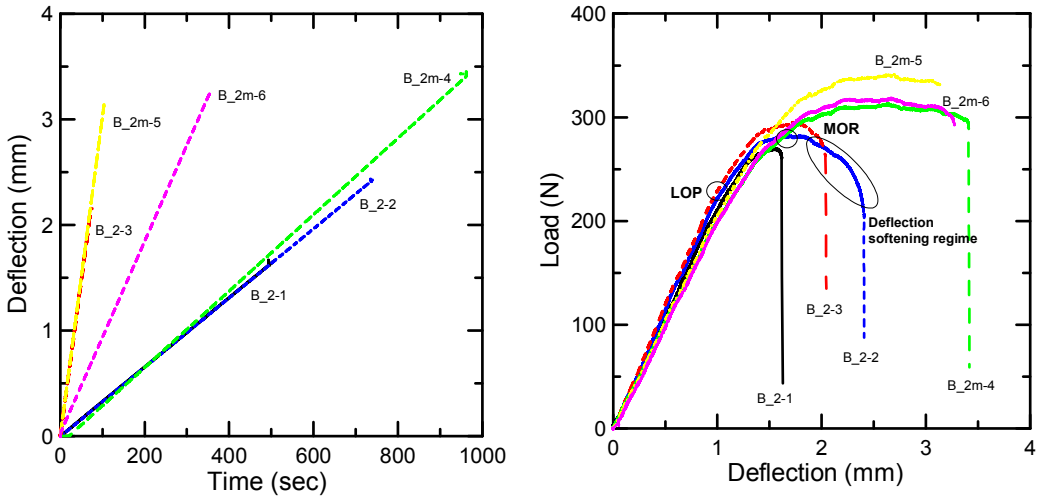

(a) (b)

Fig. 3.7 Deflection vs. time and load deflection sample types B_2 & B_2m

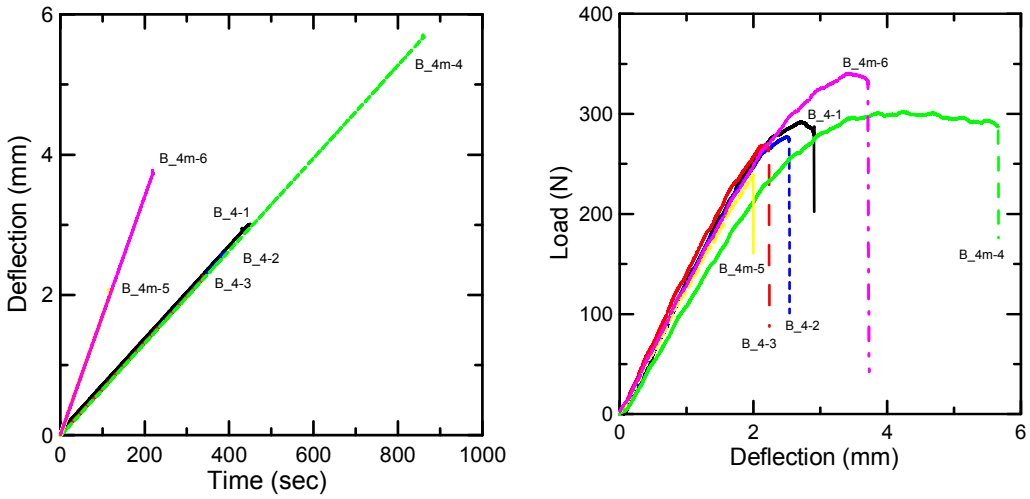

(a) (b)

Fig. 3.8 Deflection vs. time and load deflection for sample types B_4 & B_4m

The Mechanical characteristics of bending samples are shown in Table 3.3. The initial flexural stiffness is measured as the slope of the load deflection curve in the linear region between 0.3 mm and 1.00 mm. Samples with grooves show a lower initial stiffness than samples with notches even at the same speed as observed from B_1-2, B_1m-6, B_3-1, and B_3m-4. Beam types B_2, B_2m, B_4, and B_4m show more plastic deformation and less premature failure than the other types of samples. This is mainly due to the larger thickness of these samples and consequently, lower effect of stress concentration around the sharp notch at failure. This fact indicates that stress concentration plays a major role in the type of fracture and may overshadow the strain rate effect on MOR, the degree of nonlinearity, and the overall response of the material. Figure 3.7 shows that samples B_2m-4 to B_2m-6 illustrate more ductile behavior than samples B_2-1 to B_2-3. Results indicate that MOR of the material under higher loading rates is higher than its lower rate counterpart (111.9MPa in sample B_2-3 compared with 106.08MPa for sample B_2-2). Figures 3.7 and 3.8 show that increasing the speed of

loading increases the initial flexural stiffness slightly. Samples B_2 and B_2m were fractured after the peak load and after exhibiting a considerable amount of deflection softening. Beam type 4 with notch and groove (B_4, and B_4m) were tested at two speeds of 0.4 mm/min and 1.02 mm/min. Figure 3.8 shows that samples B_4-2, B_4-3, and B_4m-5 failed prematurely before reaching their load carrying capacity. Results of B_4m-4 and B_4m-6 show that a three-fold increase in loading speed, increases initial stiffness and MOR by approximately 13%.

Figure 3.9 shows the strain at the top and bottom layers in the middle of the beam vs. displacement at mid-span. As the ARAMIS system was unable to capture the surfaces at the very top and at the very bottom during deformation, strain readings provided by ARAMIS were taken as close to the surfaces as possible. As the axial strains in the layers decreases with distance from the surface, the strain observed by ARAMIS becomes slightly less precise than the actual/theoretical strains. Results show that increasing the displacement increases the axial strains at top and bottom layers of the beam. Increasing the strain at top and bottom layers is more symmetrical in beams with grooves than in beams with notches. Figure 3.10 shows the deformation of the beam B_2m-5 under load at a speed of 1.813 mm/min. Figure 3.11 shows the effect of stress concentration on the axial strain field in the middle of the beam B_2m-5 with groove, while Fig. 3.12 illustrates the extreme effect of stress concentration due to notch on axial and vertical strain distributions in the middle of beam B_2-2. These results show that axial strain distribution in notched samples do not follow the linear assumption due to stress concentration. Fig. 3.13 illustrates the fracture surface of beam B_2-2 and B_2m-4 after failure. Deflection softening regime was observed in these samples. It is clear that larger

thickness with a groove at the middle will increase the degree of nonlinearity and softening in the material behavior.

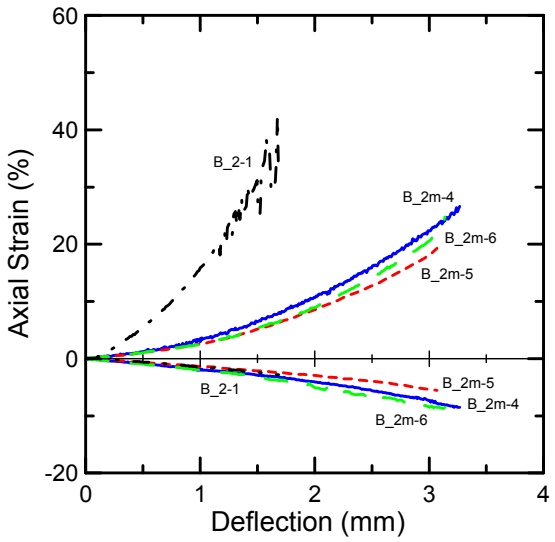

Fig. 3.9 Axial strain distribution in top & bottom layer vs. deflection at the middle of the beam for samples B_2-1, B_2m-4, B_2m-5, and B_2m-6

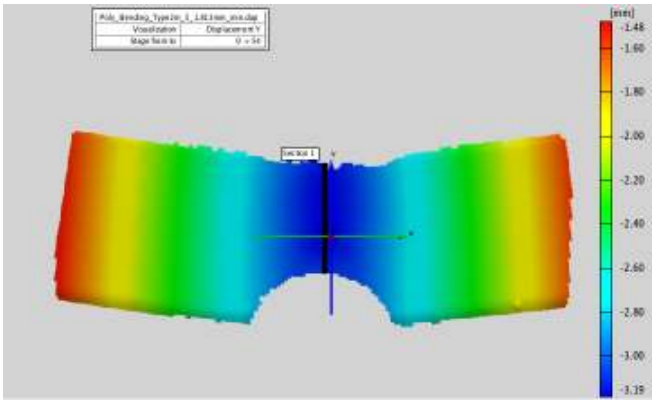

Fig. 3.10 Deflection of beam 2m-5 under loading and before failure

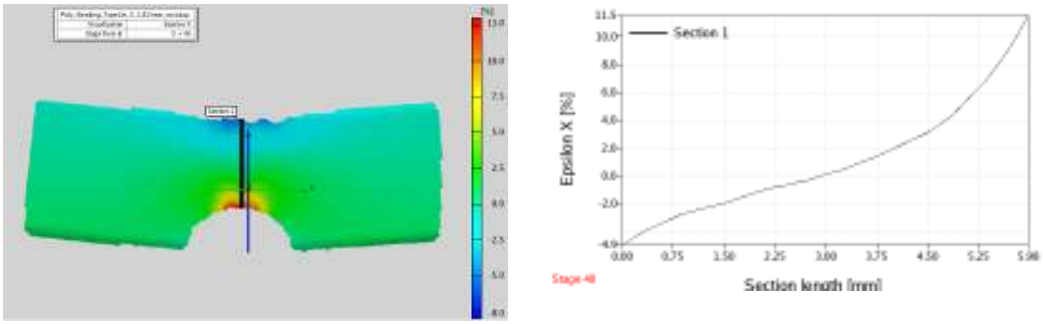

(a) (b)

Fig. 3.11 Effect of stress concentration on distribution of ε_x in beam 2m-5

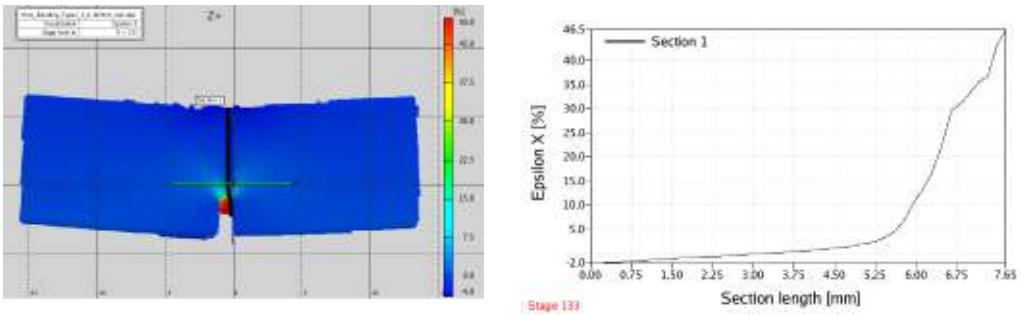

(a) (b)

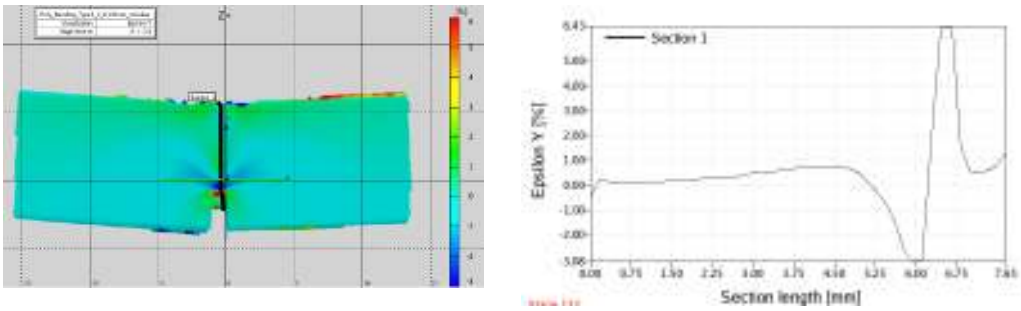

(c) (d)

Fig. 3.12 Distribution of strain in beam 2-2 (a), (b) εx; and (c), (d) εy

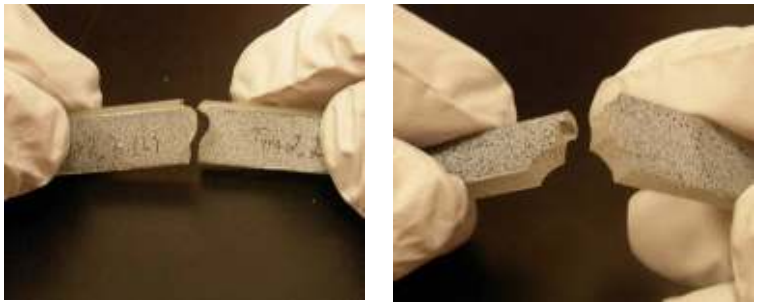

(a) (b)

Fig. 3.13 Fracture surface of the broken samples (a) B_2-2; and (b) B_2m-4

Table

3.3 Mechanical Characteristics of Flexural Load Deflection Response

Sample	Initial Slope (N/mm)	Slope of Post LOP (N/mm)	MOR (MPa)	Δ_{MOR} (mm)	LOP (MPa)	Δ_{LOP} (mm)	Deflection at Failure (mm)
B_1-1	57.49	n.a	n.a	n.a	87.2	1.90	2.45
B_1-2	60.00	n.a	n.a	n.a	n.a	n.a	1.77
B_1m-3	45.22	18.31	117.66	3.6	96.5	2.38	4.26
B_1m-4	45.62	n.a	n.a	n.a	97.77	2.39	3.01
B_1m-5	47.56	18.90	118.5	3.99	92.7	2.4	4.24
B_1m-6	48.11	21.99	120.13	3.94	90.3	2.34	4.12
B_2-1	219.93	115.04	100.3	1.54	73.9	0.92	1.67
B_2-2	224.09	90.7	106.08	1.69	81.4	0.96	2.44
B_2-3	230.8	96.6	111.9	1.72	83.3	0.94	2.16
B_2m-4	199.4	70.3	121.2	2.63	76.04	0.97	3.46
B_2m-5	202.05	76.9	132.2	2.7	83.3	1.05	3.14
B_2m-6	201.6	68.8	124.7	2.67	80.8	1.03	3.27
B_3-1	20.3	n.a	n.a	n.a	n.a	n.a	4.4
B_3-2	18.83	n.a	n.a	n.a	n.a	n.a	4.89
B_3-3	19.46	n.a	n.a	n.a	n.a	n.a	3.86
B_3m-4	17.2	12.07	115.44	6.41	93.44	4.83	6.41

B_3m-5	17.44	12.42	116.6	6.88	90.03	4.84	7.17
B_3m-6	18.27	13.2	110.46	6.6	88.9	4.67	6.6
B_4-1	141.2	79.7	91.96	2.7	61.02	1.47	3.01
B_4-2	135.7	n.a	n.a	n.a	63.7	1.34	2.61
B_4-3	141.19	n.a	n.a	n.a	65.3	1.29	2.29
B_4m-4	112.5	44.8	111.6	4.24	70.4	1.75	5.72
B_4m-5	120.0	n.a	n.a	n.a	n.a	n.a	2.07
B_4m-6	127.2	79.4	125.71	3.39	81.4	1.73	3.78

Figure 3.14 illustrates the shear strain distribution under the loading nose at the load capacity stage for beam B_2m-5. It is observed that the maximum shear strain is less than 1% in the beam. Figure 3.15 presents the nonlinearity and softening in the moment curvature response.

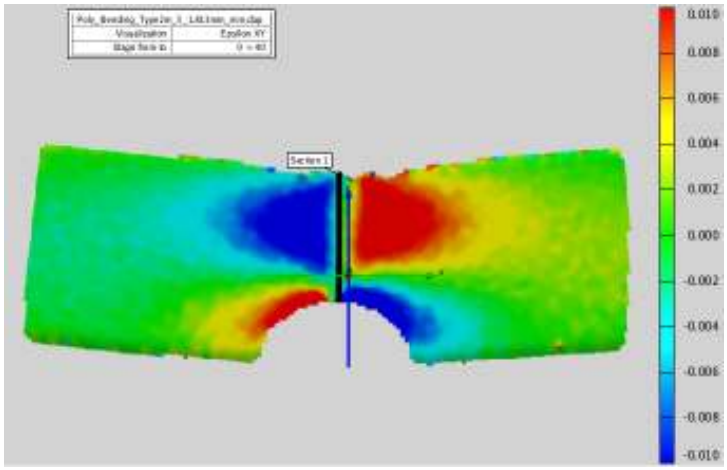

Fig. 3.14 Shear strain distribution at the maximum load capacity for B_2m-5

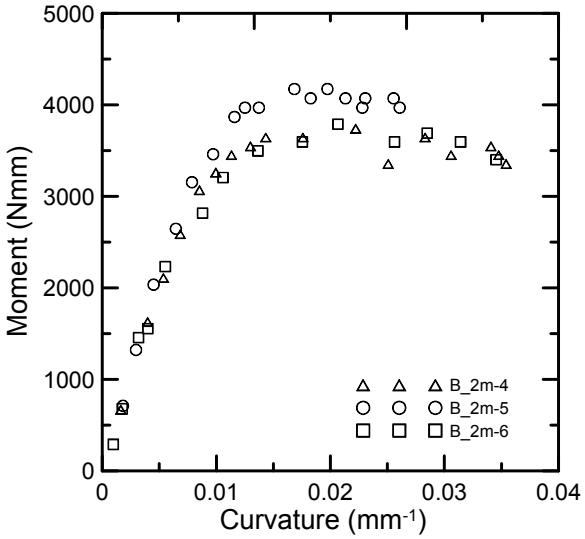

Fig. 3.15 Moment curvature response in beams B_2m-4, B_2m-5, and B_2m-6

3.4. Effect of Rate of Loading on 3PB Structural Response

Bending test specimens show a nonlinear material behavior and a considerable amount of plastic deformation. Figure 3.16 illustrates the relationships between initial slope of load deflection vs. rate of loading. Although the changes in the initial stiffness are not very visible from the load deflection curves, there is a slight increment in the initial slopes as rate of loading increases in most of the samples with the exception of samples B_3. It is to be noted that the span in samples B_3-1 and B_4-1 was 68 mm (10mm less than the other beams). The results illustrate that MOR increases approximately linearly with increasing loading rate except in B_3m where the increase in MOR is followed by a decrease at 3.45 mm/min, as shown in Fig. 3.17. This decrease might be due to the premature failure of sample B_3m-6. The results also show no specific trend in variation of LOP vs. speed of load. No specific trend is observed in variation of deflection at the failure point with respect to loading rate due to pre-mature

failure in some of the samples, as shown in Fig. 3.18. For example, while sample B_3m-5 failed in the deflection softening regime, samples B_3m-4 and B_3m-6 did not experience any softening behavior. Symbols enclosed in circles indicate overlapping data.

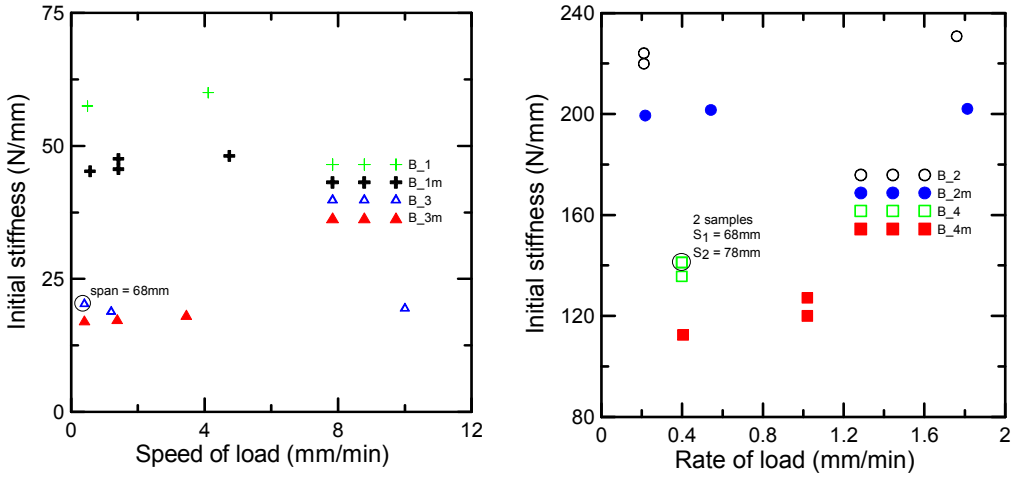

(a) (b)

Fig. 3.16 Variations of initial stiffness with respect to rate of loading

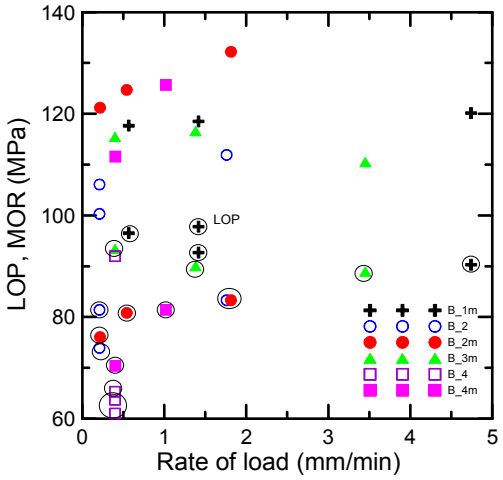

Fig. 3.17 Variations of LOP and MOR for different loading rates

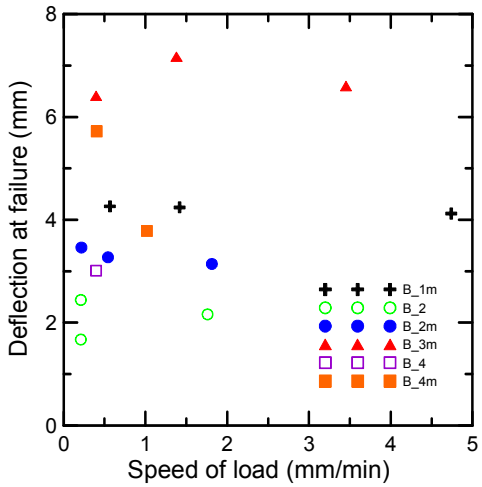

Fig. 3.18 Variations of deflection at failure with respect to load speed

3.5. Limit of Proportionality (LOP) vs. Modulus of Rupture (MOR)

A quantitative estimate of stress at the LOP point based on stress at the MOR point for all loading rates is presented in Fig. 3.19. The results show that LOP stress is around 72% of MOR stress. This can be compared to the limit of stress in the linear part of tension and compression stress strain curve under monotonic uniaxial loading, which was shown in chapter 2.

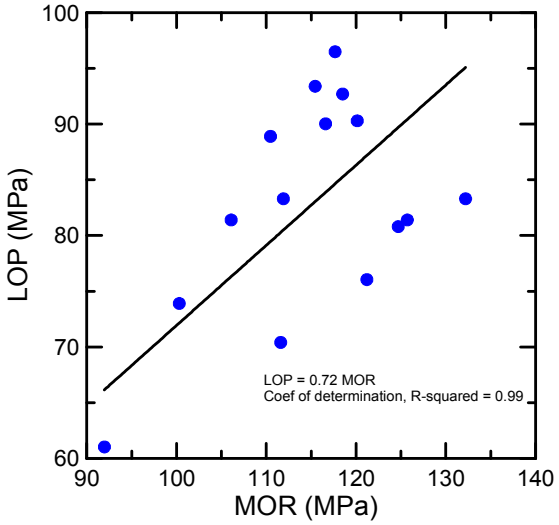

Fig. 3.19 Variations of LOP vs. MOR for flexural samples

3.6. Concluding Remarks

In this chapter, the flexural response of Epon 863 and hardener EPI-CURE 3290 has been investigated experimentally in three point bending (3PB) at different strain rates using the DIC technique. The DIC system was able to accurately provide strain field information in 3PB tests of polymeric materials. Stress concentration due to notch changes the strain distribution in the beams while groove reduces the stress concentration considerably. The results do agree with the beam bending theory. It is observed that an increase in rate of loading increases the initial stiffness and modulus of rupture (MOR). Nonlinear nature of moment curvature response and the effect of softening in the post-peak region is also demonstrated. The obtained moment curvature response can be used as material data for nonlinear analytical and numerical simulations. Quantitative estimates show that the stress at limit of proportionality (LOP) is around 72% of stress at MOR. The results of this chapter will be used as a validation tool in the constitutive model development for out-of-plane loading in polymeric materials in chapters 4 and 5.

4. Analytical Response for Flexural Behavior of Epoxy Resin Polymeric Materials

4.1. Introduction

Mechanical properties (stress strain relationship) of epoxy resin polymeric materials remain a challenge for researchers. Difficulty of a constitutive stress strain relationship in polymeric materials is mainly due to the characterization of its mechanical behavior. The hydrostatic component of stress has a significant effect on the load deformation response of resins even at low levels of stress. Hydrostatic stresses are known to affect the yield stress (i.e., the absolute value of yield stress in compression is different from the ultimate tensile stress). In order to develop a general model for epoxy resin polymeric materials, their behavior under different types of loadings has to be understood.

Several constitutive models have been proposed for polymeric materials over the past three decades. The most successful models were proposed by (Buckley and Jones, 1995; Buckley and Dooling, 2004; Boyce et al., 1989, 1994; Hasan and Boyce, 1995; Mulliken and Boyce, 2006; Tervoort, 1996, 1998; Govaert et al., 2000). Although these models differ in detail, they all combine three-dimensional, non-Newtonian viscoelastic flow and elastic strain softening. These models have been proposed in both large deformation and small deformation forms, and have been successful, especially, in fitting quasi-static test results. They have also been able to partially describe the material response at different high strain rates. Wineman and Rajagopal (2000) used a viscoplasticity model to capture the behavior of polymers. Zhang and Moore (1997) used the Bodner–Partom internal state variable model originally developed for metals to obtain the nonlinear uniaxial tensile response of polyethylene. By modifying the definitions of the effective stress and effective inelastic strain rate in the Drucker-Prager yield criteria, Li and Pan (1990), Chang and Pan (1997), and Hsu et al. (1999) developed a viscoplasticity approach for the

constitutive law of polymeric materials. Gilat et al. (2007) used an internal state variable approach to modify the Bodner model to capture the effects of hydrostatic stresses on the response. In their approach, a single unified strain variable is defined to represent all inelastic strains. Jordan et al. (2008) modified the original model of (Mulliken-Boyce, 2006) for one dimension to capture the compressive mechanical properties of polymer composites. The original model is a three dimensional strain rate and temperature-dependent model for thermoplastic polymers. Lu et al. (2001) used the viscoelastic, viscoplastic constitutive model developed by (Hasan and Boyce, 1995) to simulate the experimental results of the uniaxial compressive stress strain behavior of Epon E 828/T-403 at low and high strain rates. Some discrepancies were reported between the model and the experimental results at high strains where nearly perfect plastic flow was observed in experiments at low and medium strain rates. Chen et al. (1998) modeled the uniaxial compressive response of Epon E 828/T-403 using the Johnson-Cook model developed by Johnson (1983) at different strain rates. They simulated the experimental compression response up to 10% of true strain, but reported experimental stress strain curves showing elastic deformation, a yield-like peak, and a strain softening region up to approximately 35%. In most of these models, the majority of the parameters were determined by fitting the model to experimental tensile and compressive data. Naaman and Reinhardt (2006) used piecewise-linear stress strain and stress crack opening approaches to characterize the mechanical behavior of high-performance, fiber-reinforced cement composites. Soranakom et al. (2007a, 2007b, 2008) used piece-wise linear stress strain curve in tension and elastic perfectly plastic model in compression to study flexural behavior of cement-based composite materials. Hobbiebrunken et al. (2007) and Goodier (1993) studied the correlation between presence of defects (voids and micro-cracks) and

the volume under stress in epoxy resin glassy polymers. The crack initiation by void nucleation or a pre-existing flaw in epoxy resins was observed and the dependency of the failure behavior and strength on the size effect, stress state, and the volume of the body subjected to stress was studied (Hobbiebrunken et al., 2007; Bazant and Chen 1997; Odom and Adam 1992). Flexural strength distributions and ratio of flexural strength to tension strength of epoxy resin and PMMA materials were studied using the Weibull model (Giannotti et al., 2003; Vallo, 2002). Giannotti et al. (2003) used a modified two-parameter Weibull model to compare the effect of loading systems on the mean stress in polymeric materials, and observed that it can predict a mean flexural strength up to 40% higher than the mean tensile strength for Weibull modulus greater than 14.

In this Chapter, the flexural behavior is investigated in an attempt to establish a relationship between the tensile and compressive stress strain curves, as well as the moment curvature and load deflection response of epoxy resin material. In order to correlate tension and compression stress strain curves and flexural data, closed-form solutions have been developed to obtain moment curvature and load deflection response. A technique based on two different stress strain models has been developed to investigate the effect of out-of-plane loading on the stress strain response of the epoxy resin polymeric material. The first model is a complete strain softening model for tension and compression. The flexural behavior of polymeric materials with softening localization and strain softening in tension and compression, followed by a constant plastic flow up to failure, is studied. Local stress strain responses in tension and compression obtained for different strain rates using the results from the characterization in Chapter 2 are used as the material response for a forward solution technique. A piecewise-linear stress strain relationship is developed. The model comprises a bi-linear ascending curve up to peak,

strain softening behavior in the post-peak response, followed by constant plastic flow (Yekani Fard and Chattopadhyay, 2011[a], 2011[d]). The second model is a simplified piecewise-linear stress strain curve for tension and compression. This model is proposed for polymer materials which are considerably stronger in compression than in tension. The simplified model could be used to obtain flexural strength of polymeric materials when the complete post peak behavior of the material in tension and compression is not available. For tensile behavior, the model is bilinear up to the peak stress followed by constant plastic flow. The model for compression is bi-linear up to the peak stress followed by constant yield stress. The specific research tasks discussed in this Chapter are:

(a) Introduce a piecewise-linear tension and compression stress strain model with strain softening in post-peak response.

(b) Study the effect of different segments of uniaxial tension and compression stress strain curve on the flexural response.

(c) Develop a methodology to obtain the flexural load deflection response from uniaxial tension and compression stress strain curves for epoxy resin polymeric materials.

(d) Examine the influence of compression stress strain curves at high levels of strain on the flexural response.

(e) Evaluate the ratio of flexural strength to tension and compression peak stress.

(f) Introduce a simplified constitutive model for flexural behavior of epoxy resin polymeric materials.

(g) Study the location of the neutral axis for nonlinear phase of material behavior

The analytical approach based on softening model is summarized in a peer reviewed journal article (Yekani Fard and Chattopadyay, 2011d).

4.2. Strain Softening With Plastic Flow Model in Tension and Compression

4.2.1. Constitutive Model

Different types of epoxy resin materials share some similarities; while the compressive and tensile moduli are approximately equal, the first point showing deviation from linearity in the stress strain curve in tension is weaker than the corresponding one in the compression stress strain curve (Ward and Sweeney, 2004). It is important to observe that the general shapes of the stress strain curves in tension and compression in epoxy resin materials are similar, as they represent initial linear behavior followed by an ascending curve with reduced stiffness in the pre-peak region, and strain softening response in the post-peak region (G'Sell and Souahi, 1997; Boyce and Arruda, 1990; Buckley and Harding, 2001; Shah khan et al., 2001; Jordan et al., 2008; Littell et al., 2008; Chen et al., 2001). In general, epoxy resin materials exhibit the following distinct behavior in the tension and compression stress strain behavior: linearly elastic, nonlinearly ascending, yield-like (peak) behavior, strain softening, and nearly perfect plastic flow.

Figure 4.1 shows the proposed tension and compression stress strain curves. The two parameters characterizing the tensile response in the pre-peak region are Proportionality Elastic Limit (PEL) and Ultimate Tensile Strength (UTS). Post-peak region in tension model is expressed with slope of softening ($E_{soft,t}$), plastic flow (σ_f), and the ultimate strain (ε_{Ut}). Yield stress is often assumed to be equal to the first peak stress in the stress

strain curve. Pre-peak region in compression is characterized by Proportionality Elastic Limit in compression (PEL,c) and Compressive Yield Stress (CYS). The post-peak response in compression is determined by slope of softening ($E_{soft,c}$), compression plastic flow ($\sigma_{f,c}$), and compressive ultimate strain (ε_{Uc}). The tension and compression strain stress model is defined in Tables 4.1 and 4.2, respectively.

The complete tension and compression stress strain curves are defined uniquely by two material parameters and twelve normalized parameters: modulus of elasticity in tension (E), and strain at the tensile PEL (ε_{PEL}), and normalized strain and stiffness parameters (μ_{t1}, μ_{t2}, μ_{Ut}, μ_{co}, μ_{c1}, μ_{c2}, μ_{Uc}, α, η, γ, β, and ξ). The tensile and compressive stresses at the PEL point are related empirically to the stresses at the UTS and CYS points. Elastic modulus in tension and compression are practically identical (Foreman et al., 2010). However, bi-modulus material constants ($\gamma \neq 1$) are considered in tension and compression. Equations (4.1) to (4.3) show the definitions of the normalized parameters.

$$\mu_{c0} = \frac{\varepsilon_{PEL,c}}{\varepsilon_{PEL}},\ \mu_{c1} = \frac{\varepsilon_{CYS}}{\varepsilon_{PEL}},\ \mu_{c2} = \frac{\varepsilon_{Sc}}{\varepsilon_{PEL}},\ \mu_{t1} = \frac{\varepsilon_{Uts}}{\varepsilon_{PEL}},\ \mu_{t2} = \frac{\varepsilon_{St}}{\varepsilon_{PEL}} \tag{4.1}$$

$$\mu_{Uc} = \frac{\varepsilon_{Uc}}{\varepsilon_{PEL}},\ \mu_{Ut} = \frac{\varepsilon_{Ut}}{\varepsilon_{PEL}} \tag{4.2}$$

$$\gamma = \frac{E_c}{E},\ \beta = \frac{E_{PEL,c}}{E},\ \xi = \frac{E_{soft,c}}{E},\ \alpha = \frac{E_{PEL,t}}{E},\ \eta = \frac{E_{soft,t}}{E} \tag{4.3}$$

where μ_{co}, μ_{c1}, μ_{c2}, μ_{Uc} are normalized strain at the proportionality elastic limit point in compression, normalized strain at the CYS point, normalized strain at the end of compressive strain softening point, and normalized compressive strain at failure point, respectively. μ_{t1}, μ_{t2}, μ_{Ut} are normalized strain at UTS point, normalized strain at the end of tensile strain softening point, and normalized tensile strain at the failure point,

respectively. Stiffness parameters α, η, γ, β, and ξ are normalized stiffness at post PEL in tension, softening slope in tension, elastic stiffness in compression, post PEL in compression, and softening slope in compression.

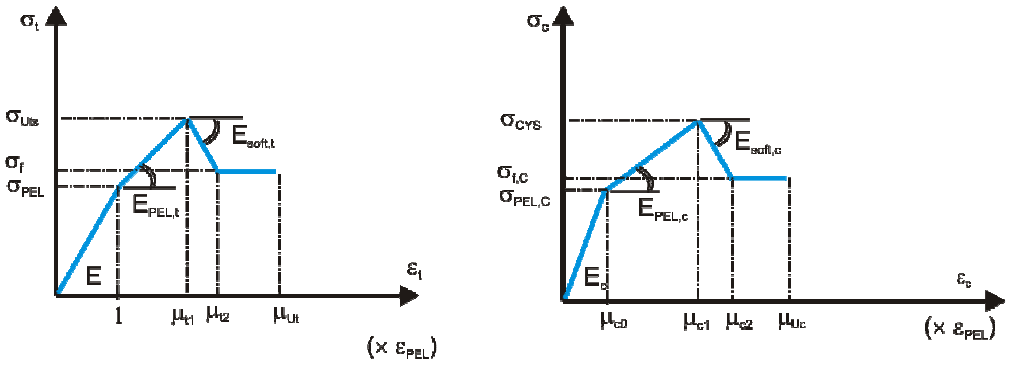

(a) (b)

Fig. 4.1 Bilinear ascending curve and strain softening post-peak response in (a) tension; and (b) compression.

Table

4.1 Definition of stress in tension

Stress	**Definition**	**Domain of strain**
$\sigma_t(\varepsilon_t)$	$E\varepsilon_t$	$0 \le \varepsilon_t \le \varepsilon_{PEL}$
	$E\,(\varepsilon_{PEL} + \alpha\,(\varepsilon_t - \varepsilon_{PEL}))$	$\varepsilon_{PEL} < \varepsilon_t \le \mu_{t1}\,\varepsilon_{PEL}$
	$E\,(\varepsilon_{PEL} + \alpha\,\varepsilon_{PEL}\,(\mu_{t1}-1) + \eta\,(\varepsilon_t - \mu_{t1}\varepsilon_{PEL}))$	$\mu_{t1}\,\varepsilon_{PEL} < \varepsilon_t \le \mu_{t2}\,\varepsilon_{PEL}$
	$E\,(\varepsilon_{PEL} + \alpha\,\varepsilon_{PEL}\,(\mu_{t1}-1) + \eta\varepsilon_{PEL}\,(\mu_{t2} - \mu_{t1}))$	$\mu_{t2}\,\varepsilon_{PEL} < \varepsilon_t \le \mu_{Ut}\,\varepsilon_{PEL}$
	0	$\mu_{Ut}\,\varepsilon_{PEL} < \varepsilon_t$

Table

4.2 Definition of stress in compression

Stress	Definition	Domain of strain
$\sigma_c(\varepsilon_c)$	$\gamma E\ \varepsilon_c$	$0 \le \varepsilon_c \le \mu_{c0}\ \varepsilon_{PEL}$
	$E(\gamma\ \mu_{c0}\ \varepsilon_{PEL} + \beta(\ \varepsilon_c - \mu_{c0}\ \varepsilon_{PEL}))$	$\mu_{c0}\ \varepsilon_{PEL} < \varepsilon_c \le \mu_{c1}\ \varepsilon_{PEL}$
	$E(\gamma\ \mu_{c0}\ \varepsilon_{PEL} + \beta\ \varepsilon_{PEL}\ (\mu_{c1} - \mu_{c0}) + \xi(\varepsilon_c - \mu_{c1}\varepsilon_{PEL}))$	$\mu_{c1}\ \varepsilon_{PEL} < \varepsilon_c \le \mu_{c2}\ \varepsilon_{PEL}$
	$E(\gamma\ \mu_{c0}\ \varepsilon_{PEL} + \beta\ \varepsilon_{PEL}\ (\mu_{c1} - \mu_{c0}) + \xi\ \varepsilon_{PEL}\ (\mu_{c2} - \mu_{c1}))$	$\mu_{c2}\ \varepsilon_{PEL} < \varepsilon_c \le \mu_{Uc}\ \varepsilon_{PEL}$
	0	$\mu_{Uc}\ \varepsilon_{PEL} < \varepsilon_c$

4.2.2. Moment Curvature Response

Strain compatibility in bending is considered to derive moment curvature relationship for a rectangular cross section with the width of *b* and the depth of *h*. Using the stress strain relationships in Fig. 4.1 and the known applied compressive strain at the top fiber ($\lambda\varepsilon_{PEL}$), 16 different cases of strain and stress distributions are shown in Fig. 4.2. The development of the stress strain relationship across a cross section, and the possibilities of tension or compression failures are presented in Fig. 4.3. In this approach, moving through different stages depends on the transition points (tp_{ij}), which are functions of material parameters as shown in Equation (4.4),

$tp_{12} = \text{Min}\ (\mu_{c0}, A)$

$tp23 = Min\ (\mu c0, C)\ or\ Min\ (\mu c1, B)$

$tp34 = Min\ (\mu c0, F)\ or\ Min\ (\mu c1, E)\ or\ Min\ (\mu c2, D)$

$tp45 = Min\ (\mu c0, J)\ or\ Min\ (\mu c1, I)\ or\ Min\ (\mu c2, H)\ or\ Min\ (\mu Uc, G)$ (4.4)

$tp56 = Min\ (\mu c1, M)\ or\ Min\ (\mu c2, L)\ or\ Min\ (\mu Uc, K)$

tp67 = Min ($\mu c2$, O) or Min (μUc, N)

tp78 = Min (μUc, P)

where indices *i* and *j* refer to origin and destination stages, respectively. Stress develops at least up to stage 4, where compressive failure is possible if $\lambda_{max} = \mu_{Uc}$ in case 10, or tensile failure may happen in case 9 when $\lambda_{max} = J$.

Characteristic points *A* to *P* are calculated as functions of material parameters to satisfy the following relation at each load step.

$$\varepsilon_t \leq \Omega \varepsilon_{PEL} \tag{4.5}$$

where ε_t is the tensile strain at the bottom fiber and Ω, depending on the case of stress distribution, is one of the following: 1, μ_{t1}, μ_{t2}, μ_{Ut}. ε_t is expressed as a linear function of the applied compressive strain at the top fiber (ε_c)

$$\varepsilon_t = \frac{1-\kappa}{\kappa}\varepsilon_c \tag{4.6}$$

where ε_c is equal to $\lambda\ \varepsilon_{PEL}$ and κ is the depth of the neutral axis, which is a function of material parameters. Characteristic points *A* and *B* are presented in Equation (4.7) as an example,

$$A = \frac{\sqrt{\gamma}-1}{\gamma-\sqrt{\gamma}},\ B = \frac{\mu_{c0}(\beta-\gamma)+\sqrt{\mu_{c0}^2\gamma(\gamma-\beta)+\beta}}{\beta} \tag{4.7}$$

As the applied strain parameter λ is incrementally imposed, the strain and stress distribution is determined, and the internal tension and compression forces are computed, e.g., the internal forces for the tension and compression subzones for case 16 Fig. 4.2(q) normalized to the tension force at the PEL point ($bhE\varepsilon_{PEL}$) is as shown in Equations (4.8) to (4.15).

$$\frac{F_{t1}}{bhE\varepsilon_{PEL}} = \frac{\kappa}{2\lambda} \tag{4.8}$$

$$\frac{F_{t2}}{bhE\varepsilon_{PEL}} = \frac{\left(2+\alpha\mu_{t1}-\alpha\right)\left(\mu_{t1}-1\right)\kappa}{2\lambda} \tag{4.9}$$

$$\frac{F_{t3}}{bhE\varepsilon_{PEL}} = \frac{\left(2+2\alpha\left(\mu_{t1}-1\right)+\eta\left(\mu_{t2}-\mu_{t1}\right)\right)\left(\mu_{t2}-\mu_{t1}\right)\kappa}{2\lambda} \tag{4.10}$$

$$\frac{F_{t4}}{bhE\varepsilon_{PEL}} = \frac{\left(1+\alpha\left(\mu_{t1}-1\right)+\eta\left(\mu_{t2}-\mu_{t1}\right)\right)\left(-\lambda-\mu_{t2}\right)\kappa}{\lambda} + 1+\alpha\left(\mu_{t1}-1\right)+\eta\left(\mu_{t2}-\mu_{t1}\right) \tag{4.11}$$

$$\frac{F_{c1}}{bhE\varepsilon_{PEL}} = \frac{\gamma\mu_{c0}^{2}\kappa}{2\lambda} \tag{4.12}$$

$$\frac{F_{c2}}{bhE\varepsilon_{PEL}} = \frac{\left(\mu_{c1}-\mu_{c0}\right)\left(2\gamma\mu_{c0}+\beta\left(\mu_{c1}-\mu_{c0}\right)\right)\kappa}{2\lambda} \tag{4.13}$$

$$\frac{F_{c3}}{bhE\varepsilon_{PEL}} = \frac{\left(\mu_{c2}-\mu_{c1}\right)\left(2\gamma\mu_{c0}+2\beta\left(\mu_{c1}-\mu_{c0}\right)+\xi\left(\mu_{c2}-\mu_{c1}\right)\right)\kappa}{2\lambda} \tag{4.14}$$

$$\frac{F_{c4}}{bhE\varepsilon_{PEL}} = \frac{\left(\lambda-\mu_{c2}\right)\left(\gamma\mu_{c0}+\beta\left(\mu_{c1}-\mu_{c0}\right)+\xi\left(\mu_{c2}-\mu_{c1}\right)\right)\kappa}{\lambda} \tag{4.15}$$

where F_{ci} and F_{ti} for (i = 1,…,4) are tension and compression forces calculated from the stress diagrams. The net force is calculated as the difference between the tension and compression forces for each case. By applying internal equilibrium, the value of κ is obtained. The expressions of net force in some stages result in more than one solution for κ. For an isotropic material, the first κ value is 0.5 as the neutral axis coincides with the centroid of the rectangular section. The neutral axis changes incrementally; as a result, the next value of κ is the closest to the previous neutral axis. Using several numerical tests for possible ranges of material parameters, the correct expression for κ is

determined, yielding a valid value of $0 < \kappa < 1$. For instance, the κ for case 16 Fig. 4.2(q) is as below

$$\kappa_{16} = \left(\begin{array}{c} \dfrac{(\lambda-\mu_{c0})^2(\gamma-\beta)+(\lambda-\mu_{c1})^2(\beta-\xi)+\xi(\lambda-\mu_{c2})^2+(\lambda+\mu_{t1})^2(\eta-\alpha)}{-2\lambda(1+\alpha(\mu_{t1}-1)+\eta(\mu_{t2}-\mu_{t1}))} + \\ \dfrac{-\eta(\lambda+\mu_{t2})^2+\alpha(\lambda+1)^2-\gamma\lambda^2-2\lambda-1}{-2\lambda(1+\alpha(\mu_{t1}-1)+\eta(\mu_{t2}-\mu_{t1}))} \end{array} \right)^{-1} \tag{4.16}$$

Figure 4.4, which uses the correct expression for the neutral axis location during loading, shows the amount of unbalanced normalized net force. For a beam with a cross section of 4 mm × 7 mm, E = 3049 MPa, and ε_{PEL}= 0.0162, the amount of unbalanced internal force is 1.4×10^{-12} N, which is negligible. Moment expressions are obtained by taking the first moment of the compression and tension forces about the neutral axis. Curvature is calculated by dividing the top compressive strain by the depth of the neutral axis κh. The general equations for normalized moment and curvature are

$$M = M_{PEL}\, M'(\lambda,\gamma,\beta,\xi,\alpha,\eta,\mu_{c0},\mu_{c1},\mu_{c2},\mu_{t1},\mu_{t2},\mu_{Ut},\mu_{Uc}) \tag{4.17}$$

$$\varphi = \varphi_{PEL}\, \varphi'(\lambda,\gamma,\beta,\xi,\alpha,\eta,\mu_{c0},\mu_{c1},\mu_{c2},\mu_{t1},\mu_{t2},\mu_{Ut},\mu_{Uc}) \tag{4.18}$$

$$\varphi_i'(\lambda,\gamma,\beta,\xi,\alpha,\eta,\mu_{c0},\mu_{c1},\mu_{c2},\mu_{t1},\mu_{t2},\mu_{Ut},\mu_{Uc}) = \frac{\lambda}{2\kappa_i}, \quad i = 1,2,3,\ldots,16 \tag{4.19}$$

where *M' and φ'* are normalized moment and curvature. M_{PEL} and φ_{PEL} are moment and curvature (for $\gamma = 1$) at the tensile PEL and are defined in Equation (4.20). Normalized moment for case 16 Fig. 4.2(q) is defined as

$$M_{PEL} = \frac{bh^2 E\varepsilon_{PEL}}{6}, \quad \varphi_{PEL} = \frac{2\varepsilon_{PEL}}{h} \tag{4.20}$$

$$M'_{16} = -\frac{\kappa_{16}^2}{\lambda^2}(1 + \xi\mu_{c2}^3 - 3\eta\mu_{t2}\lambda^2 + \alpha\mu_{t1}^3 + 3\eta\mu_{t1}\lambda^2 + 3\beta\mu_{c0}\lambda^2 - 3\lambda^2 + 3\mu_{c1}\xi\lambda^2 - 3\beta\mu_{c1}\lambda^2 - \eta\mu_{t1}^3 - 3\xi\mu_{c2}\lambda^2$$
$$- \xi\mu_{c1}^3 + 3\alpha\lambda^2 - \alpha + \eta\mu_{t2}^3 - 3\alpha\mu_{t1}\lambda^2 - 3\gamma\mu_{c0}\lambda^2 + \beta\mu_{c1}^3 - \beta\mu_{c0}^3 + \gamma\mu_{c0}^3) -$$
$$\frac{(-6\alpha\lambda^2 + 6\lambda^2 + 6\eta\mu_{t2}\lambda^2 + 6\alpha\mu_{t1}\lambda^2 - 6\eta\mu_{t1}\lambda^2)\kappa_{16}}{\lambda^2} - \frac{-3\alpha\mu_{t1}\lambda^2 + 3\alpha\lambda^2 - 3\eta\mu_{t2}\lambda^2 + 3\eta\mu_{t1}\lambda^2 - 3\lambda^2}{\lambda^2} \tag{4.21}$$

Normalized heights of compression and tension sub-zones with respect to beam depth *h* are shown in A.1 and A.2. A.3 and A.4 present the normalized stress at the vertices of the tension and compression sub-zones with respect to tensile stress at the PEL point. The internal forces in each compression and tension sub-zone for the 16 stress distribution cases are calculated from the stress diagram. The normalized forms with respect to the tension force at the PEL point ($bhE\varepsilon_{PEL}$) are presented in A.5 and A.6, where P_1 to P_9 are auxiliary variables. A.7 summarizes the results of characteristic point calculations based on Equations (4.5) and (4.6). The closed form solutions for the location of neutral axis κ_i and normalized moment M'_i for all the cases are presented in Tables A.8 and A.9. The normalized ultimate moment for a like-resin material at very large λ values (M_∞') is computed by substituting $\lambda = \infty$ in the expression for depth of neutral axis in case 16 in Equation (4.16), then by the substitution of $\lambda = \infty$ and κ_∞ in the normalized moment expression in Equation (4.21). Equation (4.22) presents the value of κ for very large λ values.

$$\kappa_\infty = \frac{\overbrace{1 + \alpha(\mu_{t1} - 1) + \eta(\mu_{t2} - \mu_{t1})}^{\text{tension term}}}{\underbrace{1 + \alpha(\mu_{t1} - 1) + \eta(\mu_{t2} - \mu_{t1})}_{\text{tension term}} + \underbrace{\gamma\mu_{c0} + \beta(\mu_{c1} - \mu_{c0}) + \xi(\mu_{c2} - \mu_{c1})}_{\text{compression term}}} \tag{4.22}$$

As it is logically expected, the numerator is a function of material parameters in tension while the denominator is a function of both tension and compression parameters. The normalized ultimate moment is obtained as a function of tension and compression material parameters as follows:

$$M'_{\infty} = \frac{\overbrace{3\left(1+\alpha\left(\mu_{t1}-1\right)+\eta\left(\mu_{t2}-\mu_{t1}\right)\right)}^{\text{tension term}}\overbrace{\left(\gamma\mu_{c0}+\beta\left(\mu_{c1}-\mu_{c0}\right)+\xi\left(\mu_{c2}-\mu_{c1}\right)\right)}^{\text{compression term}}}{\underbrace{\left(1+\alpha\left(\mu_{t1}-1\right)+\eta\left(\mu_{t2}-\mu_{t1}\right)\right)}_{\text{tension term}}\underbrace{+\left(\gamma\mu_{c0}+\beta\left(\mu_{c1}-\mu_{c0}\right)+\xi\left(\mu_{c2}-\mu_{c1}\right)\right)}_{\text{compression term}}} \quad (4.23)$$

Equation (4.19) clearly shows that normalized curvature would be a very large number for very large λ values. For elastic perfectly plastic materials with equal tensile and compressive elastic moduli and equal yield stress and strain ($\eta = \xi = 0$, $\alpha = \gamma = \beta = 1$, $\mu_{t1} = \mu_{c1} = 1$), Equations (4.22) and (4.23) yield to $\kappa = 0.5$ and $M' = 1.5$, respectively. This means that the plastic moment capacity is 1.5 times of its elastic yield strength for a rectangular cross-section (Gere 2001; Salmon and Johnson, 1990).

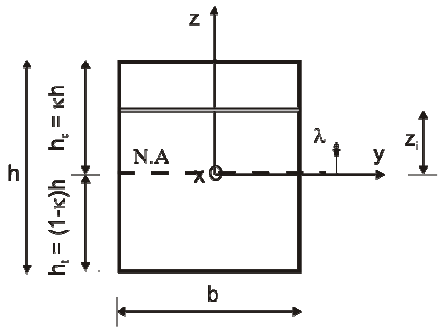

(a) rectangular section

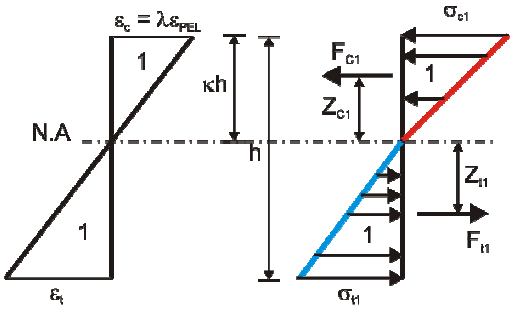

(b) case one

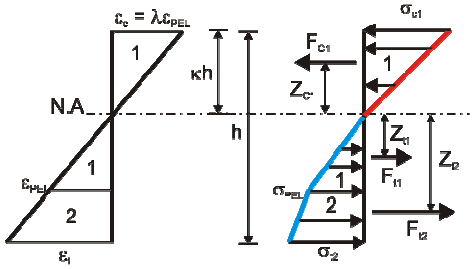

(c) case two

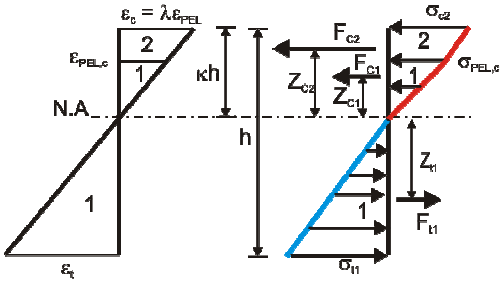

(d) case three

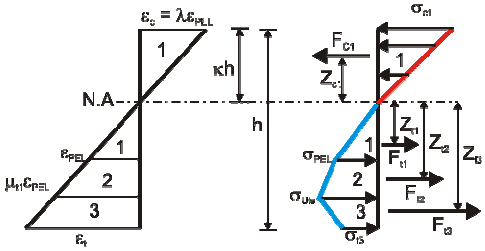

(e) case four

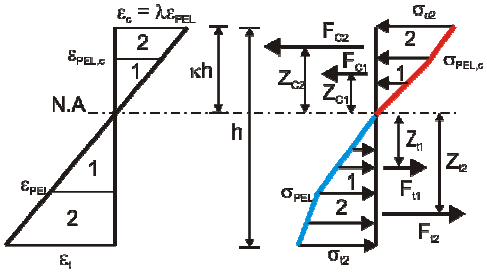

(f) case five

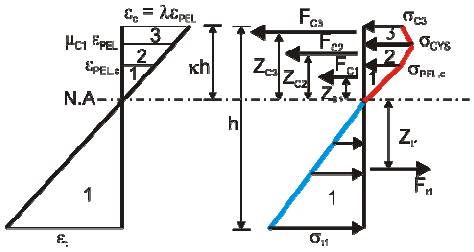

(g) case six

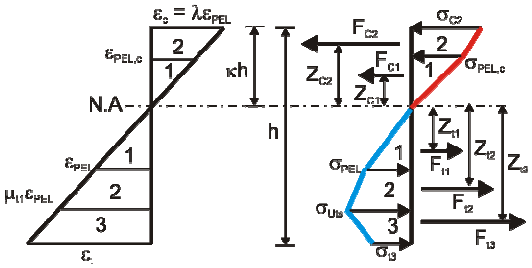

(h) case seven

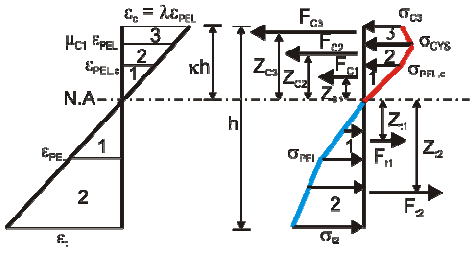

(i)case eight

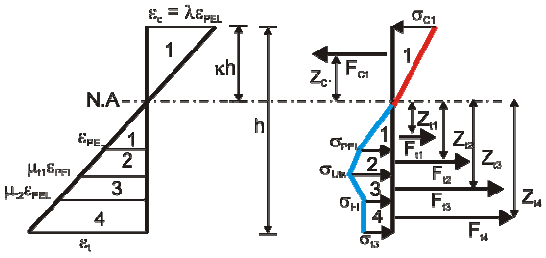

(j) case nine

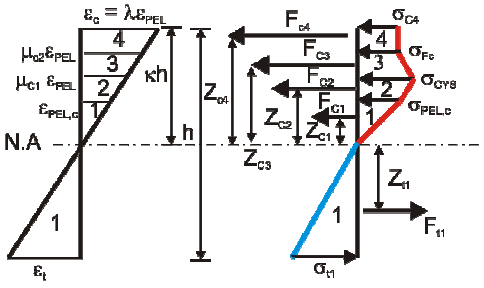

(k) case ten

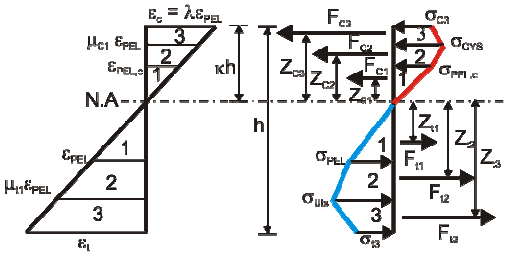

(l) case eleven

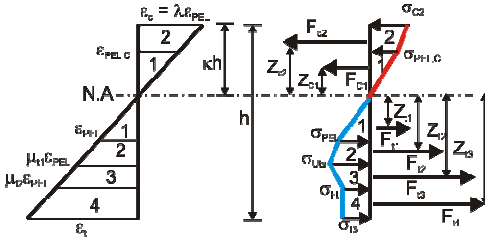

(m) case twelve

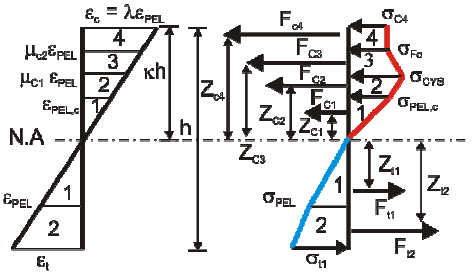

(n) case thirteen

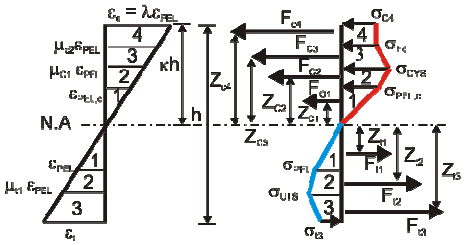

(o) case fourteen

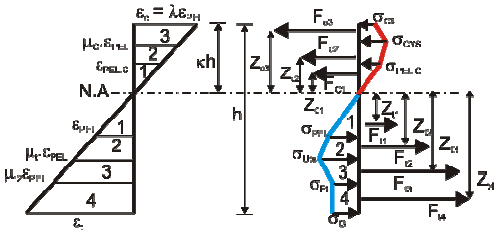

(p) case fifteen

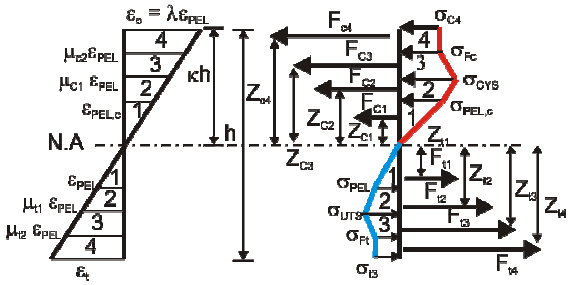

(q) case sixteen

Fig. 4.2 (a) Rectangular cross section, (b) to (q) sixteen cases of strain and stress distributions.

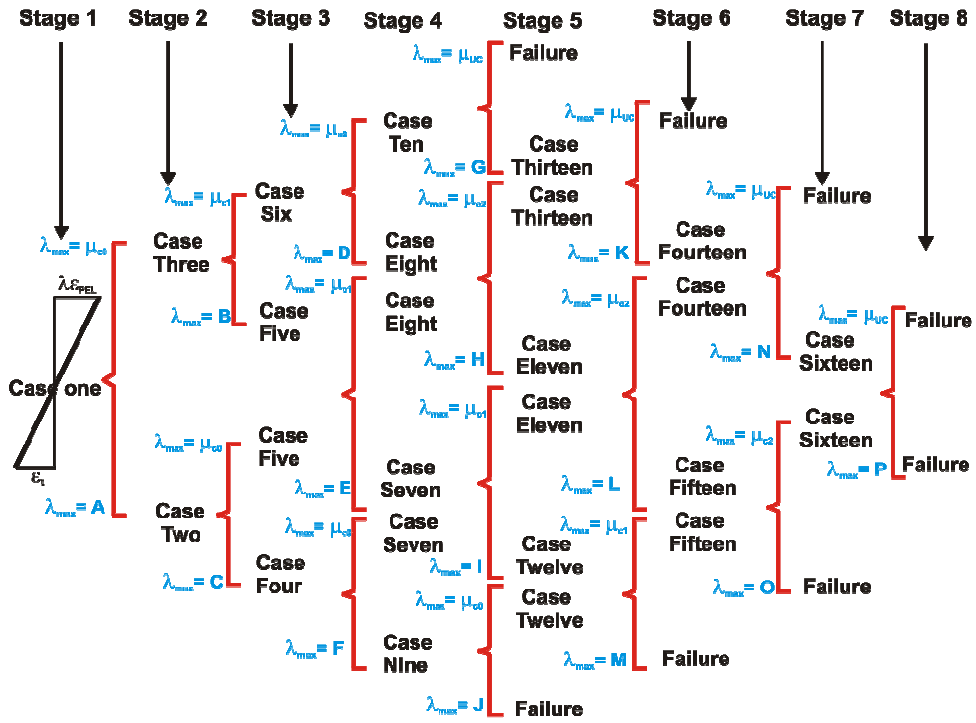

Fig. 4.3 Stress development in a cross section at different stages of loading

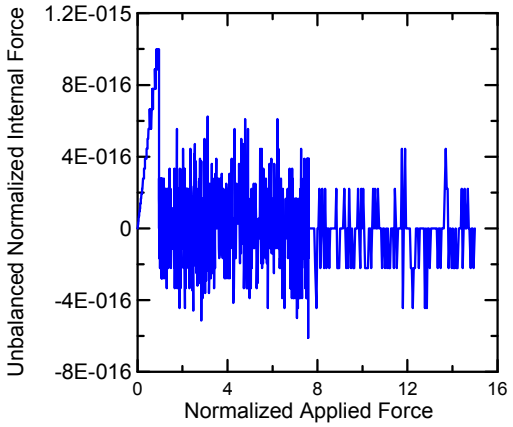

Fig. 4.4 Unbalanced normalized internal force using the correct expression for the neutral axis location during loading

4.2.3. Parametric Study

A set of analytical parametric studies based on the developed closed-form solutions for moment curvature response is presented. Although polymeric materials show strain softening behavior with a percentage of the UTS, a complete set of parametric studies is conducted to examine the effect of post-peak behavior on flexural response. The base set of parameters was defined through curve fitting to represent the material behavior of Epon E 862 studied by (Littell et al., 2008): E = 2069 MPa, Ec = 2457 MPa, ε_{PEL} = 0.0205, ε_{Uts} = 0.076, ε_{St} = 0.16, ε_{Ut} = 0.24, $\varepsilon_{PEL,c}$ = 0.019, ε_{CYS} = 0.092, ε_{Sc} = 0.15, ε_{Uc} = 0.35, σ_{Uts} = 70 MPa, σ_f = 60.5 MPa, σ_{CYS} = 93 MPa, $\sigma_{f,c}$ = 87 MPa.

Figure 4.5 shows the effect of tensile flow stress on the moment curvature and the location of the neutral axis. η = 0.3 and η = 0.001 correspond to tensile plastic flow, which equals to 25% and almost 100% of the UTS, respectively. Figure 4.5 shows that moment curvature response is extremely sensitive to the variations in constant tensile flow as the location of maximum flexure and the post-peak regime completely changes with changing tensile plastic flow stress. For the given parameters, Equation (4.23) yields to η = 0.306 for M' =1; values of η > 0.306 leads to moment capacity at failure less than elastic moment capacity at PEL. In order to obtain the bending moment at large compressive strains at the top fiber equal to or greater than the elastic bending capacity, the required tensile plastic flow should be equal to or greater than 25% of the UTS. η = 0.05 exactly characterizes the material behavior of Epon E 862, for which Equation (4.23) indicates M' = 2.55 at the ultimate point. Figure 4.5 also shows that decreasing the level of tensile flow decreases the neutral axis depth, especially for η values greater than 0.2. η = 0.2 corresponds to a tensile plastic flow stress equal to 50% of σ_{UTS}. It is

observed that the strain softening region of tensile response contributes to the flexural load carrying capacity and energy dissipation, when subjected to the flexural stress.

Figure 4.6 shows the effect of different values of σ_{UTS} at constant ε_{UTS} on the moment curvature and neutral axis location. Since the flow stress in tension is constant, the post PEL and the softening slopes are calculated for different σ_{UTS} values. The strength gain is almost proportional to σ_{UTS}; there is almost no change in stiffness, while ductility slightly increases. However, the amount of M'_{∞} is not as affected as the flexural strength, since for cases $\alpha = 0.4,\ \eta = 0.16$ and $\alpha = 0.5,\ \eta = 0.226$ the moment at infinity (for a flawless material) is less than the flexural strengths. Figure 4.6 illustrates that by increasing the UTS, the neutral axis moves downward and exceeds $\kappa = 0.5$ for the case of $\alpha = 0.5$ and $\eta = 0.226$. The effects of different post PEL slopes, strain at UTS point, and softening slopes with constant σ_{UTS} on flexural response was shown in Fig. 4.7. Results show that changes in the location of the UTS point with a constant value lead to a slight change in the moment curvature response. It is observed that the location of the UTS point, for a wide range of normalized compressive strains at top fiber between one and four, changes the location of the neutral axis and stress distributions. Figure 4.8 illustrates the effect of compressive plastic flow on moment curvature and the location of the neutral axis. Since the epoxy resin Epon E 862 is stronger in compression than tension, changes in compressive plastic flow do not change the moment capacity, but considerably affect the moment at failure. This illustrates that a decrease in compression plastic flow increases the neutral axis depth for top compressive strains greater than 0.103. Figure 4.9 shows the effects of σ_{CYS} values at constant strain. Like tension, increase of peak strength in compression at constant strain increases the flexural capacity of the epoxy resin. It is

observed that change in σ_{CYS} values at constant strain affects moment at failure less than flexural capacity. Results show that an increase of compression peak stress decreases the neutral axis depth considerably.

Researchers have observed different compression behavior in post-peak response for epoxy resins with different specimen shapes and dimensions. Strain softening at yield, followed by strain stiffening at higher strains in compression for different low and high strain rates have been reported (Littell et al. 2008; Jordan et al. 2008; Fiedler et al. 2001; Behzadi and Jones 2005; G'Sell and Souahi 1997; Boyce and Arruda 1990; Buckley and Harding 2001). However, Shah Khan et al. (2001) and Chen et al. (2001) did not observe any strain stiffening at high strains. Figure 4.10 illustrates the effect of tension and compression behavior at high strains at stress development at a point of material for epon E 862 under flexural loading. Tensile failure is the governing mechanism for all cases. Materials with $\eta \geq 0.2$ do not experience compression plastic flow and their stress strain relationship in the compression side is always in the ascending region and/or the first part of the softening regime. This is the reason that their neutral axis depth and moment capacity drop sharply thereby increasing the top compressive strain. Results show that the shape of stress strain curve for high strain values in compression do not influence the flexural response of materials in which compression is stronger than tension. Table 4.3 summarizes the effects of different parts of the tension and compression stress strain model on the flexural response of epoxy resin Epon E 862.

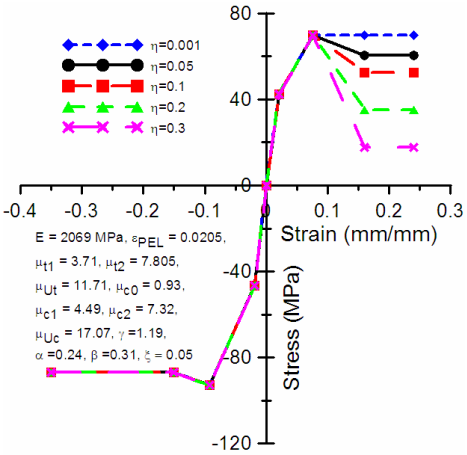

(a)

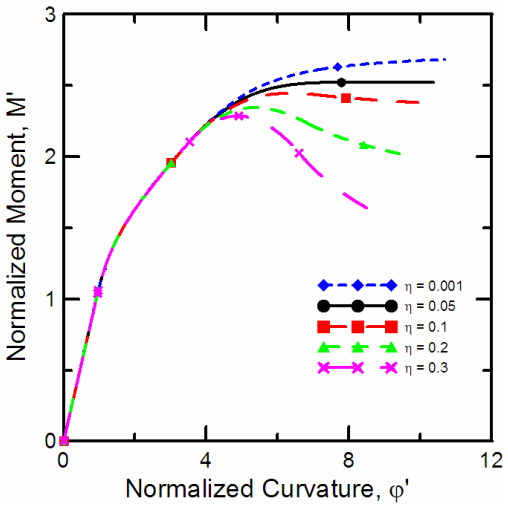

(b)

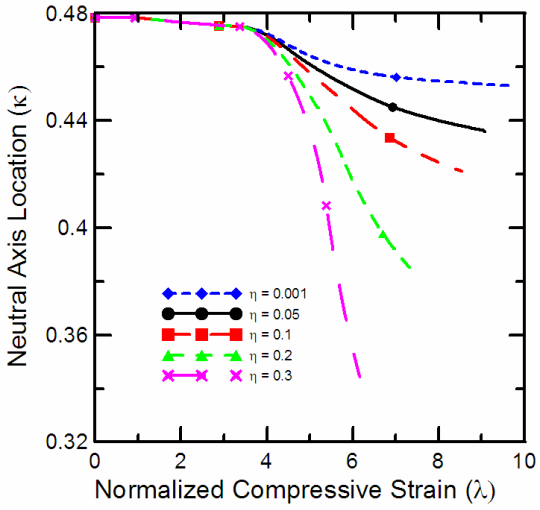

(c)

Fig. 4.5 Effect of tensile flow stress on moment curvature and location of neutral axis

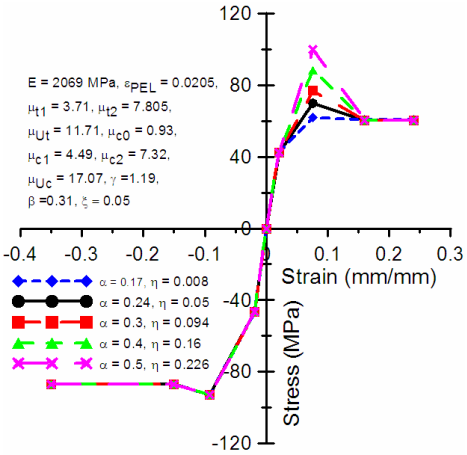

(a)

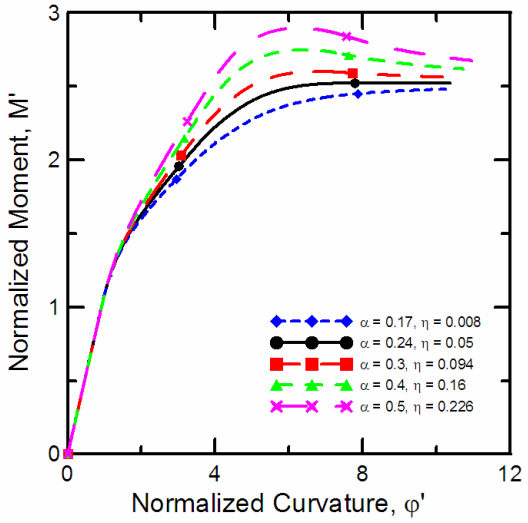

(b)

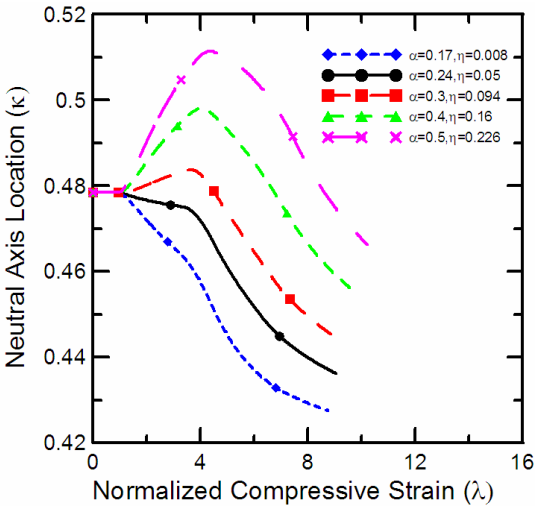

(c)

Fig. 4.6 Effect of σ_{Uts} at constant ε_{Uts} on moment curvature and neutral axis

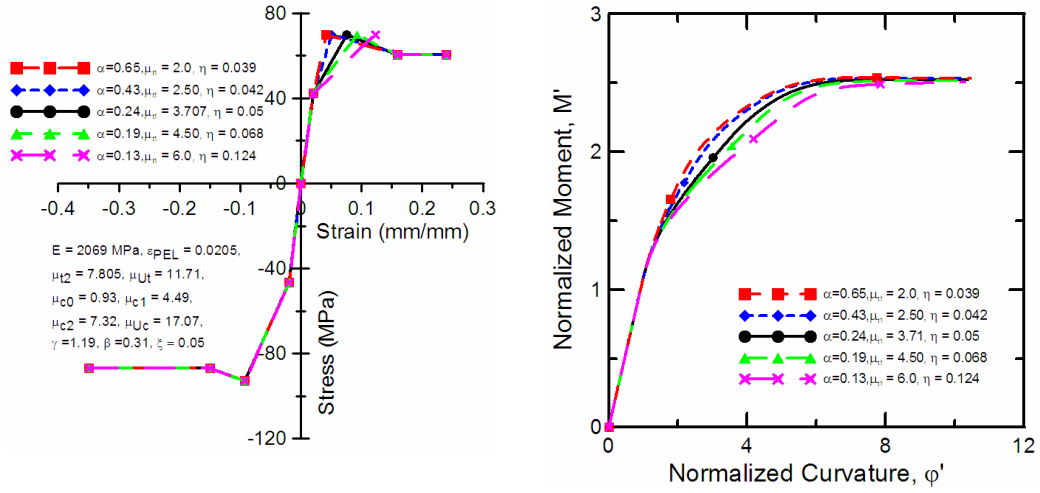

(a) (b)

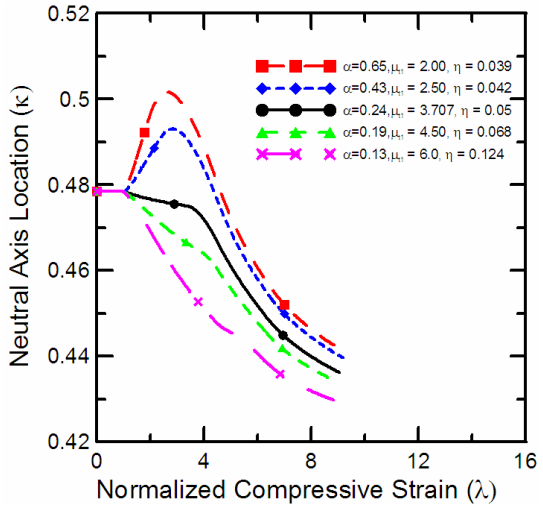

(c)

Fig. 4.7 Effect of post PEL and strain softening slopes at constant σ_{Uts} on flexural response

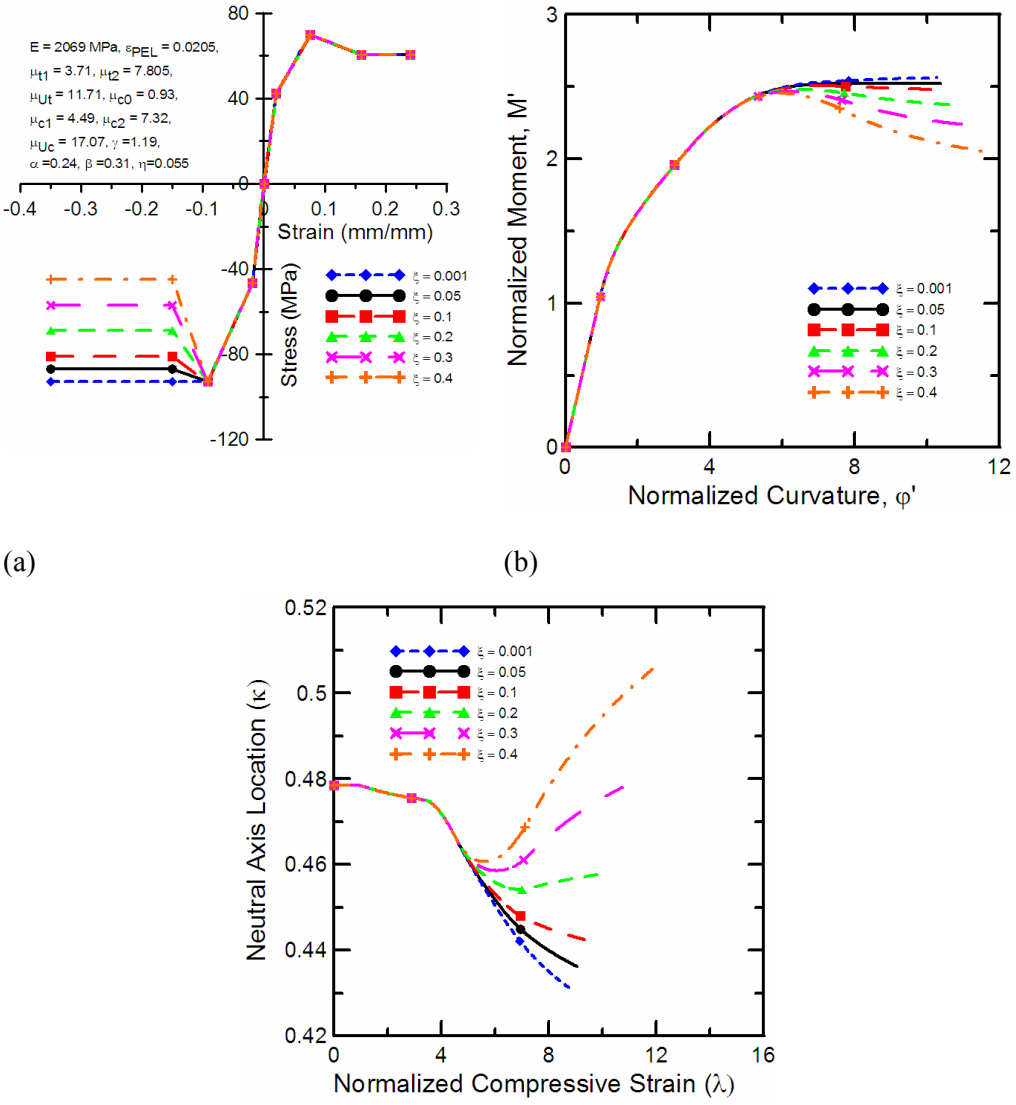

Fig. 4.8 Effect of compression flow stress on moment curvature and neutral axis.

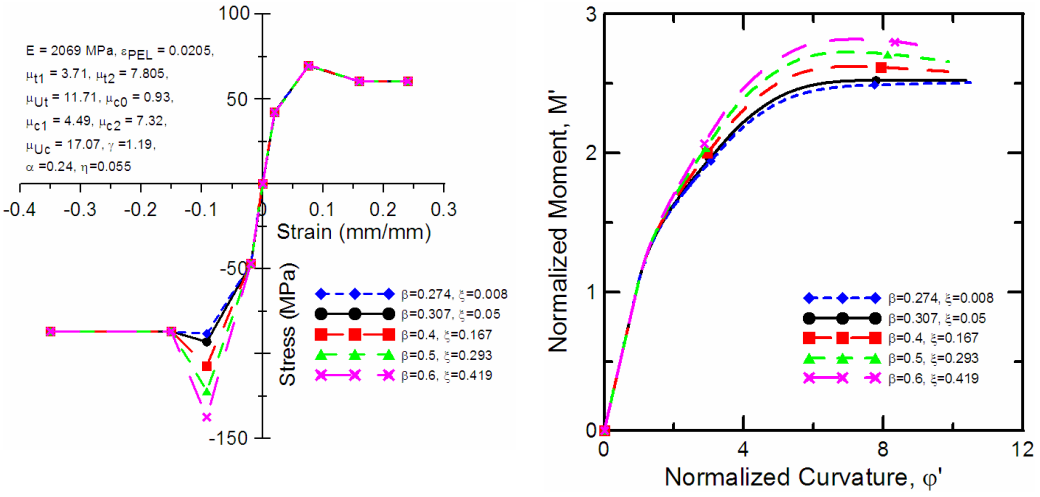

(a) (b)

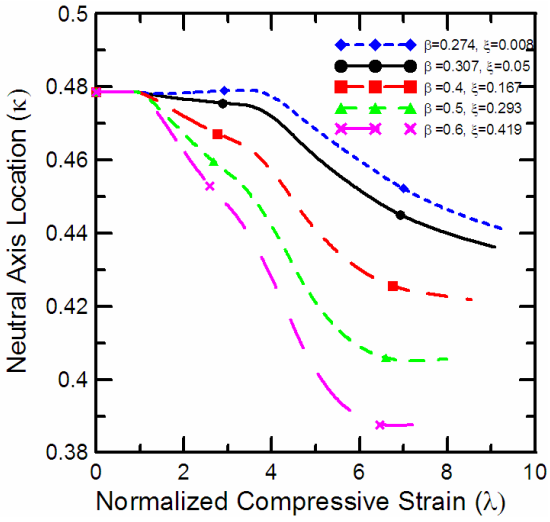

(c)

Fig. 4.9 Effect of σ_{CYS} at constant ε_{CYS} on moment curvature and neutral axis

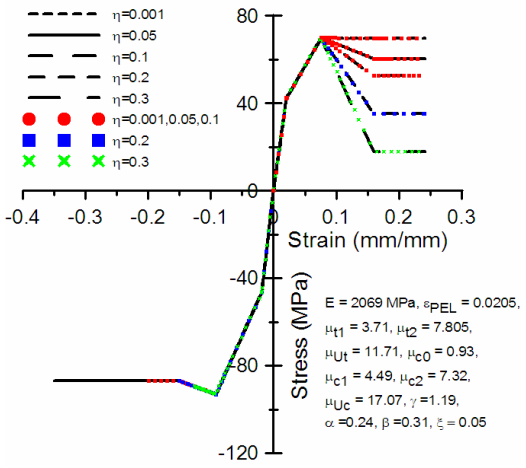

Fig. 4.10 Effect of tension plastic flow on stress development at a point of material

Table

4.3 Effects of Uniaxial Constitutive Models on Flexural Response

Parameter in Flexural response	**Parameters in compression tension model with primary effect**	**Parameters in compression tension model with secondary effect**
Flexural capacity	• tensile plastic flow • UTS at constant strain • UTS at constant post PEL slope • CYS at constant strain • strain of CYS at constant CYS	• CYS at constant post PEL slope
Moment at failure	• tensile plastic flow • compression plastic flow • CYS at constant strain	• UTS at constant strain • UTS at constant post PEL slope

		• CYS at constant post PEL slope • strain of CYS at constant CYS
Elastic moment		• compressive elastic stiffness and CYS
κ at elastic regime	• compression elastic stiffness and CYS • compression elastic stiffness	
κ at high strains	• tensile plastic flow • UTS at constant strain • strain of UTS at constant UTS • compression plastic flow • CYS at constant strain • strain of CYS at constant CYS	• UTS at constant post PEL slope • CYS at constant post PEL slope • compressive elastic stiffness & CYS • compressive elastic stiffness

4.3. Constant Post-peak Response in Tension and Constant Yield in Compression Model

4.3.1. Simplified Constitutive Model

Results of uniaxial tests in Chapter 2 showed the bilinear ascending stress strain curve in tension and compression followed by strain softening and almost a constant flow in

post-peak response. In cubic samples, strain stiffening at high strains was observed due to triaxiality effects. However, study of stress development in Epon E 863 subject to flexural loading showed that the material never experiences compression plastic flow, and the stress strain relationship in the compression side is always in the ascending region and/or in the first part of the softening regime. This is mainly due to the fact that Epon E 863 is stronger in compression than in tension. This fact will help to simplify the post-peak behavior of tension and compression stress strain model for flexural behavior of epoxy resin materials in which compression is stronger than tension. This simplified model could be used to obtain the load carrying capacity of polymeric materials when sufficient information about post-peak behavior of uniaxial tension and compression stress strain curve is not available. In compression, the strain softening and constant plastic flow is replaced by a plastic curve with no hardening. In tension, the strain softening slope and the constant plastic flow is replaced by a constant softening curve. Therefore, a simplified piecewise-linear stress strain curve for tension and compression, as shown in Fig. 4.11 is proposed in this section.

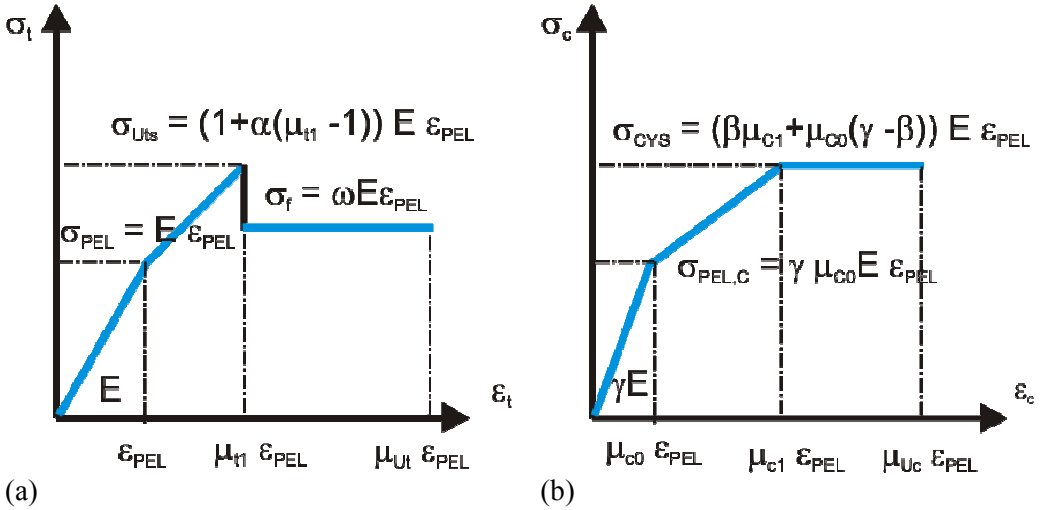

Fig. 4.11 (a) Constant flow in tension and (b) constant yield in compression

In this model, the tension and compression curves are defined uniquely by the parameters E, ε_{PEL}, μ_{t1}, μ_{Ut}, α, ω, γ, β, μ_{co}, μ_{c1}, and μ_{Uc}. ω is normalized tensile softening stress and other parameters were defined in section 4.2.1 and in nomenclature. The tensile stress at PEL point is related empirically to the stress at UTS point. Like the strain softening model, the ascending part of the tension and compression stress strain diagrams consist of two linear parts: a) 0 to PEL and PEL to UTS in tension and b) 0 to PEL and PEL to CYS in compression. The curve in post-peak response is idealized as horizontal with σ_f as the post-peak sustained stress in tension and σ_{CYS} constant yield strength in compression. The constant post-peak tensile stress level ω shows the ability of the model to represent different levels of softening response. The post-peak response in tension and compression terminates at the ultimate tension strain level ($\varepsilon_{Ut} = \mu_{Ut}\ \varepsilon_{PEL}$) and ultimate compression strain level ($\varepsilon_{Uc} = \mu_{Uc}\ \varepsilon_{PEL}$), respectively. In the elastic range, elastic modulus in tension and compression for epoxy resin materials are practically identical (Foreman et al., 2010). However, the material model could be treated as a bi-modulus in tension and compression. The tension and compression stress strain relationship are defined in 4.4. The nine normalized parameters used in the definition of the constitutive stress strain curves are defined by

$$\mu_{c0} = \frac{\varepsilon_{PEL,c}}{\varepsilon_{PEL}},\ \mu_{c1} = \frac{\varepsilon_{CYS}}{\varepsilon_{PEL}},\ \mu_{Uc} = \frac{\varepsilon_{Uc}}{\varepsilon_{PEL}},\ \mu_{t1} = \frac{\varepsilon_{Uts}}{\varepsilon_{PEL}},\ \mu_{Ut} = \frac{\varepsilon_{Ut}}{\varepsilon_{PEL}} \tag{4.24}$$

$$\gamma = \frac{E_c}{E},\ \beta = \frac{E_{PEL,c}}{E},\ \alpha = \frac{E_{PEL,t}}{E} \tag{4.25}$$

$$\omega = \frac{\sigma_f}{\sigma_{PEL}} \tag{4.26}$$

Table

4.4 Definition of Simplified Tension and Compression Stress Strain Model

Stress	Definition	Domain of strain
$\sigma_t(\varepsilon_t)$	$E\varepsilon_t$	$0 \le \varepsilon_t \le \varepsilon_{PEL}$
	$E(\varepsilon_{PEL} + \alpha(\varepsilon_t - \varepsilon_{PEL}))$	$\varepsilon_{PEL} < \varepsilon_t \le \mu_{t1}\ \varepsilon_{PEL}$
	$\omega E\ \varepsilon_{PEL}$	$\mu_{t1}\ \varepsilon_{PEL} < \varepsilon_t \le \mu_{Ut}\ \varepsilon_{PEL}$
	0	$\mu_{Ut}\ \varepsilon_{PEL} < \varepsilon_t$
$\sigma_c(\varepsilon_c)$	$\gamma E\ \varepsilon_c$	$0 \le \varepsilon_c \le \mu_{c0}\ \varepsilon_{PEL}$
	$E(\gamma\mu_{c0}\ \varepsilon_{PEL} + \beta(\varepsilon_c - \mu_{c0}\ \varepsilon_{PEL}))$	$\mu_{c0}\ \varepsilon_{PEL} < \varepsilon_c \le \mu_{c1}\ \varepsilon_{PEL}$
	$E\ \varepsilon_{PEL}(\beta\mu_{c1} + \mu_{c0}(\gamma - \beta))$	$\mu_{c1}\ \varepsilon_{PEL} < \varepsilon_c \le \mu_{Uc}\ \varepsilon_{PEL}$
	0	$\mu_{Uc}\ \varepsilon_{PEL} < \varepsilon_c$

4.3.2. Moment Curvature Response for Simplified Model

A rectangular cross section beam with width *b* and depth *h* is assumed. Since there are three distinct stress strain curves for each tension and compression stress strain relationship, there would be 9 different cases of stress distribution across the section as shown in Fig. 4.12. Although some of the cases are unlikely to happen for epoxy resin materials, the algorithm has been developed for any possible case so that any kind of material with uniaxial tension and compression stress strain could be modeled, as shown in Fig. 4.11. Linear strain distribution has been assumed in all the cases. Load is applied by imposing a normalized compressive strain (λ) at top fiber. Table B.1 presents the normalized height for each sub-zone with respect to beam depth *h*. Tables B.2 and B.3 present the stresses at the vertices of the tension and compression sub-zones normalized to tension stress at the PEL point. Areas under the stress curves represent tension and compression forces, which are normalized to tension force at the PEL point ($bhE\varepsilon_{PEL}$) and

are summarized in Tables B.4 and B.5. The centroid of each sub-zone represents the line of action, and the normalized moment arm with respect to the neutral axis is presented in Tables B.6 and B.7.

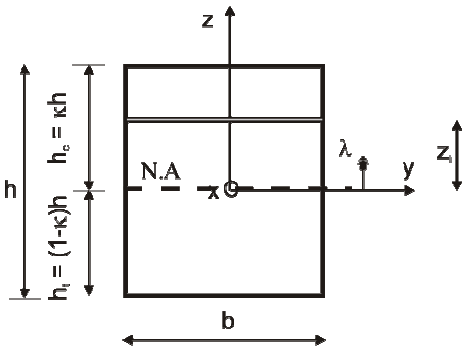

(a) rectangular cross section

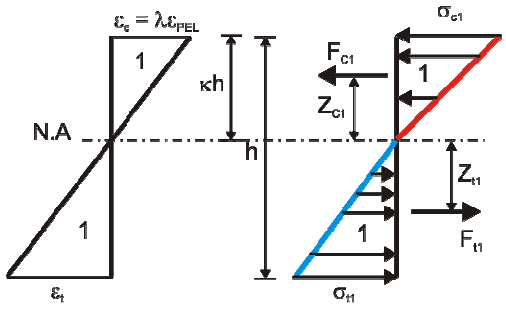

(b) case one

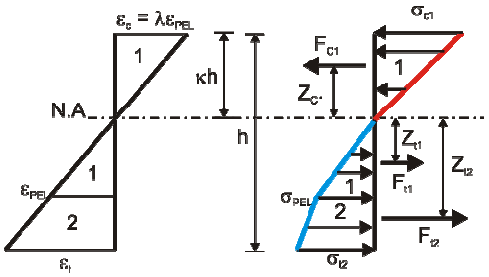

(c) case two

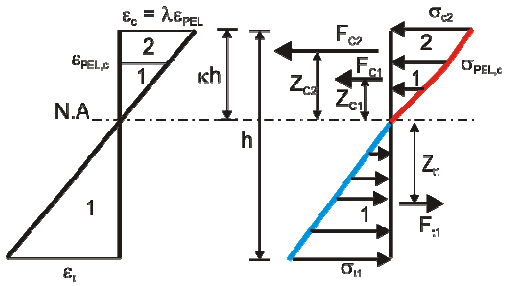

(d) case three

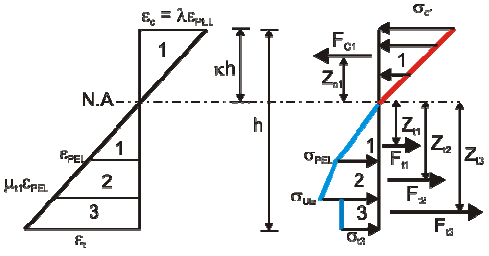

(e) case four

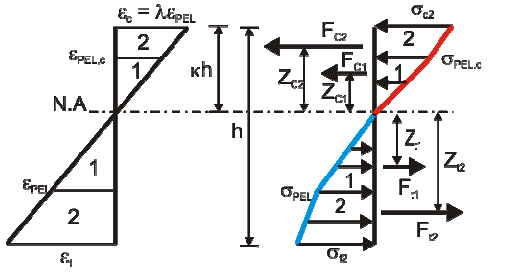

(f) case five

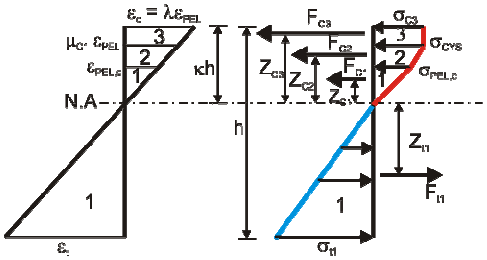

(g) case six

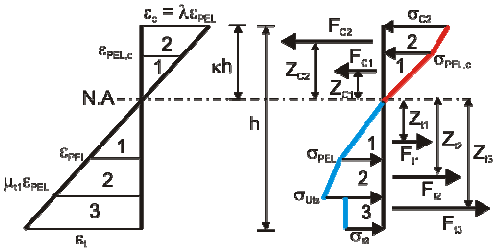

(h) case seven

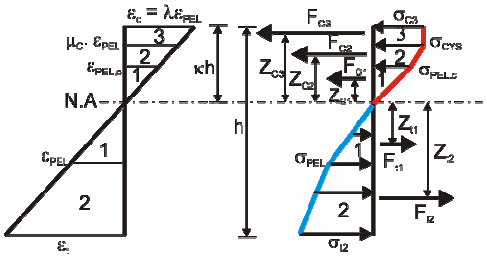

(i)

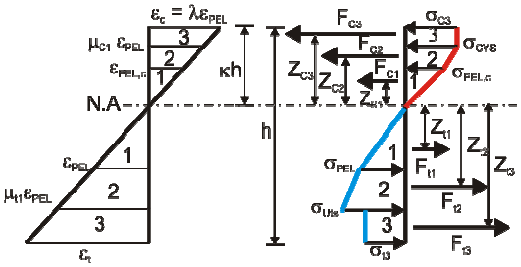

(j)

Fig. 4.12 Rectangular cross section and nine cases of strain and stress distribution across the cross section

As the load is increased through normalized compressive strain in the top fiber, the stress distribution changes from elastic linear to inelastic nonlinear. Figure 4.13 illustrates the stress profile in the cross-section based on the simplified model. It shows that stress develops at least to stage four, where compressive failure is possible if $\lambda_{max} = \mu_{Uc}$ in case six, or tensile failure may happen when $\lambda_{max} = F$ in case four.

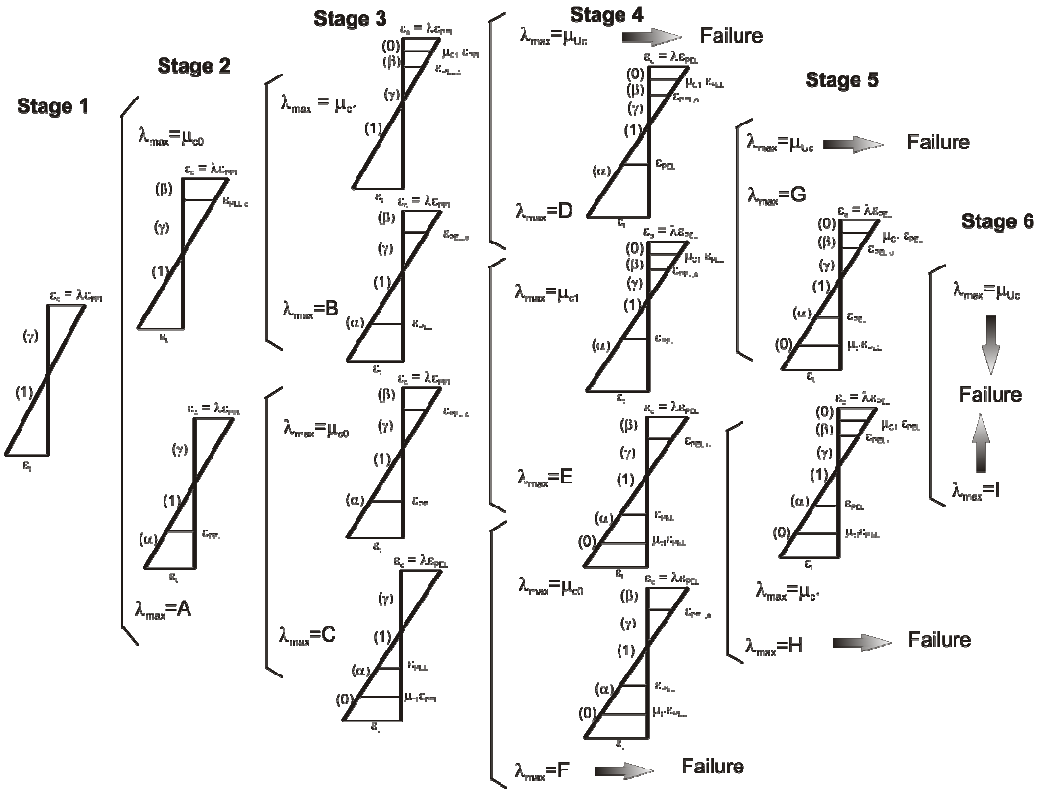

Fig. 4.13 Strain profile at different stages of loading based on simplified model

Stress evolution through the stages, shown in Fig. 4.13, depends on the controlling value λ_{max}. Characteristic points in Fig. 4.13 are functions of the material parameters and are defined in Table B.8. Transition points, defined by the parameter tp_{ij} between different stages in Fig. 4.13, are described as follows.

$$
\begin{aligned}
tp_{12} &= Min(\mu_{c0}, A) \\
tp_{23} &= Min(\mu_{c0}, C) \ \ or \ Min(\mu_{c1}, B) \\
tp_{34} &= Min(\mu_{Uc}, D) \ or \ \ Min(\mu_{c1}, E) \ or \ \ Min(\mu_{c0}, F) \\
tp_{45} &= Min(\mu_{Uc}, G) \ or \ \ Min(\mu_{c1}, H) \\
tp_{56} &= Min(\mu_{Uc}, I)
\end{aligned}
\tag{4.27}
$$

where indices i and j refer to origin and destination stage, respectively. The location of the neutral axis, κ, throughout the loading is obtained by imposing the equilibrium condition at each case for every normalized load (λ_m) as shown in Equation 4.28.

For λ_m (m = 0 to $n_{failure}$),

$$\sum_{i=1}^{3} F_{ti} - \sum_{j=1}^{3} F_{cj} = 0 \Rightarrow \kappa_m(\alpha, \beta, \gamma, \omega, \mu_{t1}, \mu_{c0}, \mu_{c1}, \lambda) \tag{4.28}$$

Similar to the case of the softening model in tension and compression, the equilibrium governing equation in some cases may result in more than one solution for κ. The valid value of κ is between 0 and 1, and the correct expressions for κ presented in Table B.9 are determined based on several cases of numerical tests covering all possible ranges of material parameters. Figure 4.14 shows the negligible unbalanced normalized internal force using the correct expressions for κ.

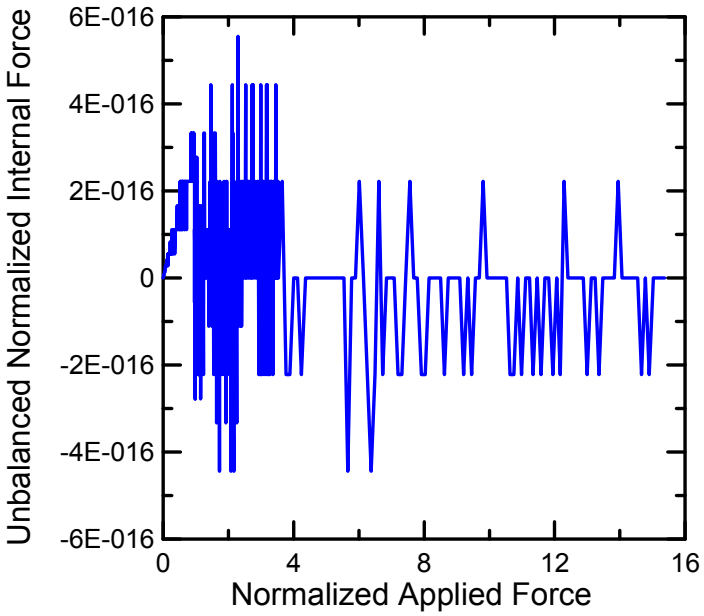

Fig. 4.14 Negligible unbalanced normalized internal force during loading

For each case and over the entire loading process, the moment is calculated up to failure point. Also, curvature is determined as the ratio of compressive strain at top fiber to the depth of neutral axis. The steps to obtain the normalized moment and curvature expressions for case nine in Fig. 4.12 (j) are explained in details in Equations (4.29) to (4.55).

$$Fc_{91} = \frac{\gamma E\, b\kappa h\, \mu_{c0}^2\, \varepsilon_{PEL}}{2\lambda} \tag{4.29}$$

$$Fc_{92} = \frac{E\, b\kappa h \left(\mu_{c1} - \mu_{c0}\right)\left(2\gamma\mu_{c0} + \beta\left(\mu_{c1} - \mu_{c0}\right)\right)\varepsilon_{PEL}}{2\lambda} \tag{4.30}$$

$$Fc_{93} = E\, b\kappa h\left(1 - \frac{\mu_{c1}}{\lambda}\right)\left(\gamma\, \mu_{c0} + \beta\left(\mu_{c1} - \mu_{c0}\right)\right)\varepsilon_{PEL} \tag{4.31}$$

$$Ft_{91} = \frac{E\, b\kappa h\ \varepsilon_{PEL}}{2\lambda} \tag{4.32}$$

$$Ft_{92} = \frac{E\, b\kappa h \left(\mu_{t1} - 1\right)\left(2 + \alpha\left(\mu_{t1} - 1\right)\right)\varepsilon_{PEL}}{2\lambda} \tag{4.33}$$

$$Ft_{93} = E\, bh\omega\left(1 - \kappa - \frac{\kappa\, \mu_{t1}}{\lambda}\right)\varepsilon_{PEL} \tag{4.34}$$

$$Zc_{91} = \frac{2\, \mu_{c0}\, \kappa h}{3\lambda} \tag{4.35}$$

$$Zc_{92} = \frac{\mu_{c0}\, \kappa h}{\lambda} + \frac{\kappa h \left(\mu_{c1} - \mu_{c0}\right)\left(3\gamma\mu_{c0} + 2\beta\left(\mu_{c1} - \mu_{c0}\right)\right)}{3\lambda\left(2\gamma\mu_{c0} + \beta\left(\mu_{c1} - \mu_{c0}\right)\right)} \tag{4.36}$$

$$Zc_{93} = \frac{\mu_{c1}\, \kappa h}{\lambda} + \frac{1}{2}\kappa h\left(1 - \frac{\mu_{c1}}{\lambda}\right) \tag{4.37}$$

$$Zt_{91} = \frac{2\ \kappa h}{3\lambda} \tag{4.38}$$

$$Zt_{92} = \frac{\kappa h}{\lambda} + \frac{\kappa h\left(\mu_{t1} - 1\right)\left(3 + 2\alpha\left(\mu_{t1} - 1\right)\right)}{\lambda\left(6 + 3\alpha\left(\mu_{t1} - 1\right)\right)} \tag{4.39}$$

$$Zt_{93} = \frac{\mu_{t1}\kappa h}{\lambda} + \frac{1}{2}h\left(1 - \kappa - \frac{\mu_{t1}\kappa}{\lambda}\right) \tag{4.40}$$

$$fcn_{91} = \frac{\gamma\kappa\,\mu_{c0}^{2}}{2\lambda} \tag{4.41}$$

$$fcn_{92} = \frac{\kappa\left(\mu_{c1} - \mu_{c0}\right)\left(2\gamma\mu_{c0} + \beta\left(\mu_{c1} - \mu_{c0}\right)\right)}{2\lambda} \tag{4.42}$$

$$fcn_{93} = \kappa\left(1 - \frac{\mu_{c1}}{\lambda}\right)\left(\gamma\,\mu_{c0} + \beta\left(\mu_{c1} - \mu_{c0}\right)\right) \tag{4.43}$$

$$ftn_{91} = \frac{\kappa}{2\lambda} \tag{4.44}$$

$$ftn_{92} = \frac{\kappa\left(\mu_{t1} - 1\right)\left(2 + \alpha\left(\mu_{t1} - 1\right)\right)}{2\lambda} \tag{4.45}$$

$$ftn_{93} = \omega\left(1 - \kappa - \frac{\kappa\,\mu_{t1}}{\lambda}\right) \tag{4.46}$$

$$zcn_{91} = \frac{2\,\mu_{c0}\,\kappa}{3\lambda} \tag{4.47}$$

$$zcn_{92} = \frac{\kappa\left(3\gamma\mu_{c0}^{2} + \beta\mu_{c1}\left(2\mu_{c1} - \mu_{c0}\right) - \beta\mu_{c0}^{2} + 3\gamma\mu_{c0}\mu_{c1}\right)}{3\lambda\left(2\gamma\mu_{c0} + \beta\left(\mu_{c1} - \mu_{c0}\right)\right)} \tag{4.48}$$

$$zcn_{93} = \frac{\kappa\left(\lambda + \mu_{c1}\right)}{2\lambda} \tag{4.49}$$

$$ztn_{91} = \frac{2\,\kappa}{3\lambda} \tag{4.50}$$

$$ztn_{92} = \frac{\kappa\left(3\left(\mu_{t1}+1\right)+\alpha\mu_{t1}\left(2\mu_{t1}-1\right)-\alpha\right)}{\lambda\left(6+3\alpha\left(\mu_{t1}-1\right)\right)} \tag{4.51}$$

$$ztn_{93} = \frac{1}{2} - \frac{1}{2}\left(\kappa - \frac{\mu_{t1}\kappa}{\lambda}\right) \tag{4.52}$$

$$\sum_{i=1}^{3} F_{ti} - \sum_{j=1}^{3} F_{cj} = 0 \Rightarrow \kappa_9 =$$

$$\frac{2\omega\lambda}{\left(1-2\mu_{t1}-\alpha\left(\mu_{t1}^2+1\right)+2\omega\left(\lambda+\mu_{t1}\right)+2\alpha\mu_{t1}-\beta\mu_{c1}^2+\left(\beta-\gamma\right)\mu_{c0}^2+2\gamma\lambda\mu_{c0}+2\beta\lambda\left(\mu_{c1}-\mu_{c0}\right)\right)} \tag{4.53}$$

$$mm_9 = \frac{6}{b\,h^2\,E\varepsilon_{PEL}}\left(\sum_{i=1}^{3} Fc_{9i}Zc_{9i} + \sum_{i=1}^{3} Ft_{9i}\,Zt_{9i}\right)$$

$$mm_9 = \frac{\kappa^2}{\lambda^2}\left(\mu_{c0}^3\left(\beta-\gamma\right)+3\mu_{c0}\lambda^2\left(\gamma-\beta\right)-1+3\mu_{t1}^2\left(1-\alpha\right)+\alpha+3\beta\mu_{c1}\lambda^2+3\omega\left(\lambda^2-\mu_{t1}^2\right)\right)$$
$$+\frac{\kappa^2}{\lambda^2}\left(2\alpha\mu_{t1}^3-\beta\mu_{c1}^3\right)-6\omega\kappa+3\omega \tag{4.54}$$

$$\varphi_9 = \frac{h}{2\varepsilon_{PEL}}\frac{\lambda\varepsilon_{PEL}}{\kappa_9\,h} = \frac{\lambda}{2\kappa_9} \tag{4.55}$$

where Fc_{9i} and Ft_{9i} (i = 1,2,3) are compression and tension forces. fcn_{9i} and ftn_{9i} (i = 1,2,3) are the normalized tension and compression forces. Moment arms and their normalized values are represented by Zc_{9i}, Zt_{9i}, zcn_{9i}, and ztn_{9i}. The closed form solutions for normalized moment M_i with respect to the values at PEL points are presented in Table B.9.

The general definitions for normalized moment and curvature are shown in Equations (4.56) through (4.58) where M_{PEL} and φ_{PEL}, defined in Equation (4.20), are moment and curvature (for a material with the same modulus of elasticity in tension and compression) at the PEL.

$$M(\lambda,\gamma,\beta,\alpha,\mu_{c0},\mu_{c1},\mu_{t1},\mu_{Ut},\mu_{Uc},\omega)=M_{PEL}\,M'(\lambda,\gamma,\beta,\alpha,\mu_{c0},\mu_{c1},\mu_{t1},\mu_{Ut},\mu_{Uc},\omega) \tag{4.56}$$

$$\varphi(\lambda,\gamma,\beta,\alpha,\mu_{c0},\mu_{c1},\mu_{t1},\mu_{Ut},\mu_{Uc},\omega)=\varphi_{PEL}\,\varphi'(\lambda,\gamma,\beta,\alpha,\mu_{c0},\mu_{c1},\mu_{t1},\mu_{Ut},\mu_{Uc},\omega) \tag{4.57}$$

$$\varphi'_i(\lambda,\gamma,\beta,\alpha,\mu_{c0},\mu_{c1},\mu_{t1},\mu_{Ut},\mu_{Uc},\omega)=\frac{\lambda}{2\kappa_i},\quad i = 1,2,3,\ldots,9 \tag{4.58}$$

If there is no intrinsic flaw in a material, M_u could approach M_∞ for very large λ values. For this ideal situation, the normalized moment at very large λ values, M'_∞ is computed by substituting $\lambda = \infty$ in the expression for κ in case nine of Table B.9, and by substituting $\lambda = \infty$ and κ_∞ in the normalized moment expression. Equations (4.59) through (4.61) present the values of the neutral axis depth, normalized moment, and curvature for very large λ values.

$$\kappa_\infty=\frac{\omega}{\omega+\gamma\mu_{c0}-\beta\mu_{c0}+\beta\mu_{c1}} \tag{4.59}$$

$$M'_\infty=\frac{3\omega(\gamma\mu_{c0}-\beta\mu_{c0}+\beta\mu_{c1})}{\omega+\gamma\mu_{c0}-\beta\mu_{c0}+\beta\mu_{c1}} \tag{4.60}$$

$$\varphi'_\infty=\infty \tag{4.61}$$

The neutral axis depth and normalized moment are a function of material parameters (ω, γ,β,μ_{c0}, μ_{c1}). It is interesting to note that the only tensile material parameter in

Equations (4.59) and (4.60) is tension softening stress. Expression $\gamma\mu_{c0} + \beta (\mu_{c1} - \mu_{c0})$ is the definition of normalized σ_{CYS}. For flawless epoxy resin material with very low softening stress in tension with respect to normalized σ_{CYS}, the normalized moment is almost 3 times the softening stress in tension. For an elastic perfectly plastic material, Equations (4.59) and (4.60) yield $\kappa = 0.5$ and M' = 1.5, respectively. For a set of parameters, $\gamma,\beta,\mu_{c0}, \mu_{c1}$, the critical value of ω can be found, which results in a flexural capacity at infinity (i.e., failure) greater than the flexural capacity at the tensile PEL point. By equating the normalized moment for large compressive strain in top fiber to unity ($M'_{\infty} = 1$) the critical value of post-peak tension flow, $\omega_{critical}$, is expressed as

$$\omega_{critical} = \frac{\gamma\mu_{c0} - \beta\mu_{c0} + \beta\mu_{c1}}{3(\gamma\mu_{c0} - \beta\mu_{c0} + \beta\mu_{c1}) - 1} \tag{4.62}$$

The required parameters for Epon E 862 were defined through curve fitting to the tension and compression stress strain curve provided by (Littell et al., 2008). For Epon E 863, the parameters were obtained from tension and compression stress strain curves at 493 μstr/sec in Chapter 2. Table 4.5 indicates that the minimum required level for normalized tension softening stress for E 862 and E 863 is 0.4 in order for the moment at the post-peak response to be greater than the elastic moment.

Table

4.5 Minimum Tension Softening Stress

Epoxy Resin	γ	β	μ_{co}	μ_{c1}	$\omega_{critical}$
E 862	1.19	0.307	0.93	4.49	**0.39**
E 863	1.09	0.298	1.148	3.52	**0.4**

4.3.3. Parametric Study

In a continuation of the examination of strain softening epoxy resin material from section 4.2.3, a set of parametric studies is conducted here to further study the effects of different segments of tension and compression stress strain curves on flexural behavior. Similar to strain softening with constant plastic flow model, material parameters of Epon E 862 epoxy resin (Littell et al., 2008) are extracted as the base material: E = 2069 MPa, Ec = 2457 MPa, ε_{PEL} = 0.0205, ε_{Uts} = 0.076, ε_{Ut} = 0.24, $\varepsilon_{PEL,c}$ = 0.019, ε_{CYS} = 0.092, ε_{Uc} = 0.35, σ_{Uts} = 70 MPa, σ_f = 60.5 MPa, σ_{CYS} = 93 MPa.

Figure 4.15 (a) through (c) presents the effect of tensile softening stress on the moment curvature and the location of neutral axis depth. In Fig. 4.15 (a), the normalized plastic flow stress (ω) is 0.017 and 1.63, equal to 1% and 100% of the ultimate tensile strength. In Epon E 862 as compression peak and softening stresses are stronger than tension stresses, moment carrying capacity (maximum moment) is sensitive to tensile softening stress as the location of maximum moment and the post-peak regime completely changes with ω. Calculations showed that for Epon E 862 $\omega_{critical}$ is 0.39. Figure 4.15 (b) also shows that in order to obtain bending moment at large compressive strains equal to or greater than elastic bending capacity, the required tensile softening stress should be at least 25% of the ultimate tensile strength ($\omega_{critical}$ =0.39). The curve with ω=1.42 accurately characterizes the material behavior of Epon E 862 and it shows that moment carrying capacity of E 862 is 2.58 times higher than its elastic moment.

Figure 4.15 (c) shows that a decrease in tensile softening stress decreases the neutral axis depth, especially for ω values less than 0.5 (30% of UTS). For a resin material without any intrinsic flaw, tensile failure is the governing failure mechanism. Cases with

ω = 0.08 and ω = 0.017 do not experience compression yield during flexure, and their stress strain relationship are in the compression ascending region. This is the reason that their neutral axis depth and moment capacity drops sharply by increasing load, and they show a more brittle material behavior. Tracing the stress development algorithm in Fig. 4.13 with the material parameters of E 862 shows that the stress development in the cross section is completely independent of tensile plastic flow in stages 1-3. Stage 4 would also be independent of ω if $tp_{23} \neq C$ in stage 3. Calculation of the transition points indicates that $tp_{12} = A$ = 0.9167 in case 2, $tp_{23} = \mu_{c0}$ = 0.93 in case 5, $tp_{34} = E$ = 3.358 in case 7, and for all ω values. For ω = 0.017 and 0.08, $tp_{45} = H$ (H (ω=0.017) = 3.43, H (ω=0.08) = 3.70), and tensile failure happens in stage 5. However, for ω = 0.393, 0.5, 0.83, 1.16, 1.42, 1.49, and 1.62, tp_{45} would be equal to μ_{c1} = 4.49 in case nine. Comparison of I(ω) with μ_{Uc} shows that all cases will fail in tension in stage 6.

Figure 4.16 (a) through (c) depicts the effect of ultimate tensile stress with constant PEL slope and constant tensile softening stress on the moment curvature and neutral axis location. Figure 4.16 (b) reveals that an increase in μ_{t1} considerably increases flexural strength. However, the amount of moment at failure is not affected as much as the flexural strength since for $\mu_{t1} > 6$, the moment at infinity is less than the flexural strength. Figure 4.16 (c) shows an increase in the ultimate tensile strength increases the neutral axis depth, and κ approaches 0.5. It is possible to look at the variation of μ_{t1} as the variation of σ_{CYS} to σ_{UTS} ratio, which is defined as $\frac{\gamma\mu_{c0} + \beta(\mu_{c1} - \mu_{c0})}{1 + \alpha(\mu_{t1} - 1)}$. By substituting γ = 1.19, β = 0.3, α =0.24, μ_{c0} = 0.93, μ_{c1} = 4.49, it is clear that changes in μ_{t1} from 2.75 to 8 will change the σ_{CYS} to σ_{UTS} ratio from 1.53 to 0.81.

Figure 4.17 (a) illustrates the effect of strain at constant ultimate tensile stress on the flexural behavior. The compression and tension models with different post tensile PEL slope and strain of UTS points, varying from 0.15 to 0.6 and 5.33 to 2.083, respectively, are considered. Stress strain models of three sets of α and μ_{t1} are shown in Fig. 4.17 (a). Figures 4.17 (b) and (c) reveals that changes in parameters α and μ_{t1} have a slight effect on the moment, but an extreme effect on the position of the neutral axis for a wide range of normalized top compressive strains between one and four, which in turn, will change the stress distribution in the cross section between elastic and post-peak range.

In order to study the influence of strain at constant compressive yield stress on flexural behavior, a range of parameters, β and $\mu_{c1,}$ was used while σ_{CYS} is constant. The compressive and tensile stress strain models are shown in Fig. 4.18 (a). Like the post-tensile PEL stiffness, analysis of Fig.4.18 (b) depicts that moment carrying capacity is not sensitive to changes in parameters β and μ_{c1}, but curvature at the maximum moment changes with changing β and μ_{c1}. Fig. 4.18 (c) shows the profile of the neutral axis position versus the applied top compressive strain. Curves of (β = 0.1, μ_{c1} = 11.61) and (β = 0.2, μ_{c1} = 6.27) are completely different from others. After λ exceeds the compressive PEL, the neutral axis depth sharply increases to statically equilibrate the axial forces in the cross section, but since σ_{CYS} is greater than σ_{UTS} and tensile softening stress, the neutral axis depth starts to decrease in the post-peak regions. Material with (β = 0.1, μ_{c1} = 11.61) do not experience any yield in compression, and all the curves fail in tension.

Figure 4.19 (a) shows the compressive and tensile stress strain relationship with different compressive yield stresses. σ_{CYS} is from 62.04 MPa for β = 0.1 to 137.54 MPa for β = 0.6. The value of σ_{UTS} is 70.2 MPa and constant for all cases. Increasing the

compressive yield strength by 100% increases the flexural capacity around 40% as shown by the normalized moment curvature plots in Fig. 4.19 (b). Figure 4.19 (c) depicts that for $\beta = 0.1$ and 0.2, as σ_{CYS} is in the range of σ_{UTS}, the neutral axis is almost in the middle of the section throughout the loading. An analysis indicates that tension is the governing failure mechanism in all cases while compression strain exceeds just the yield point.

In order to study the effect of proportionality elastic limit in compression, a range of parameters, γ and $\mu_{c0,}$ were coupled at a fixed compressive PEL to tensile PEL ratio of $\gamma\mu_{c0} = 1.107$ as shown in Fig. 4.20 (a) through (c). Figure 4.20 (b) and (c) reveal that changes in the location of compressive PEL point slightly affect the moment curvature and the location of the neutral axis, especially in the nonlinear phase. Analyses show that all the cases experience yielding in compression and failure in tension.

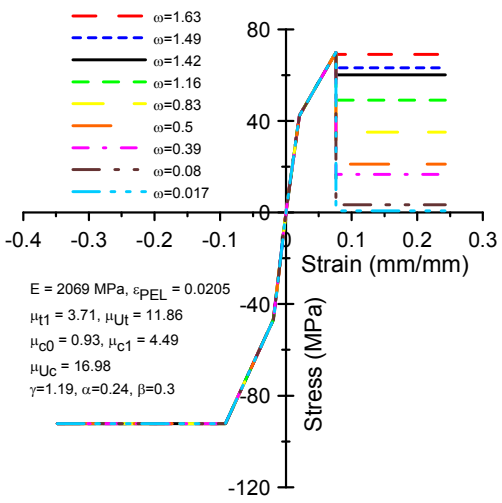

(a)

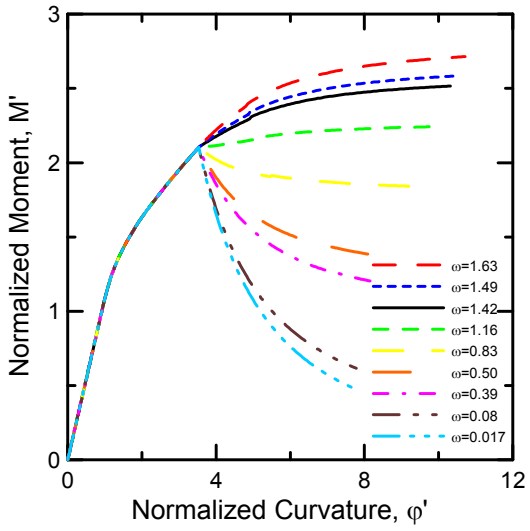

(b)

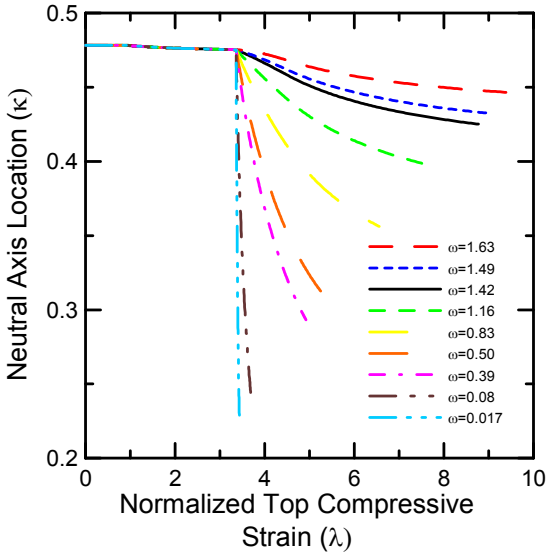

(c)

Fig. 4.15 Effect of constant tensile softening stress on moment curvature and neutral axis location

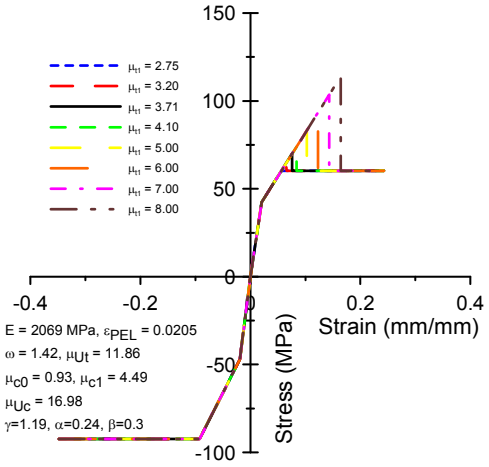

(a)

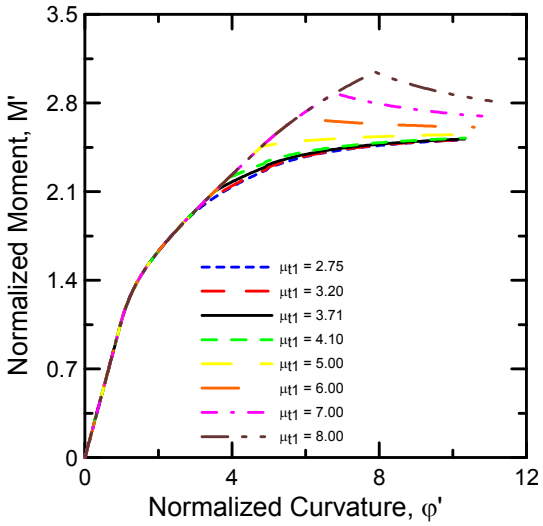

(b)

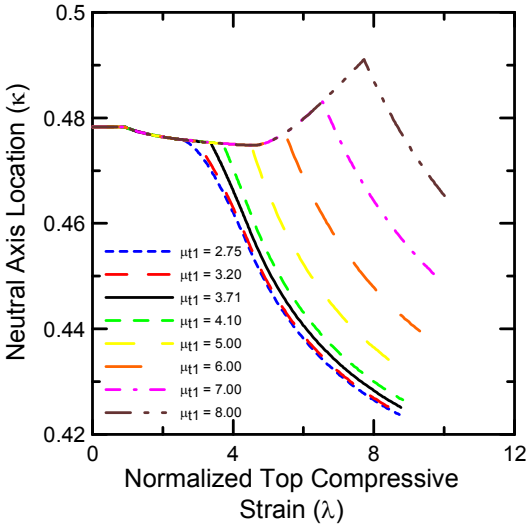

(c)

Fig. 4.16 Effect of ultimate tensile stress at constant post PEL slope and constant tensile softening stress

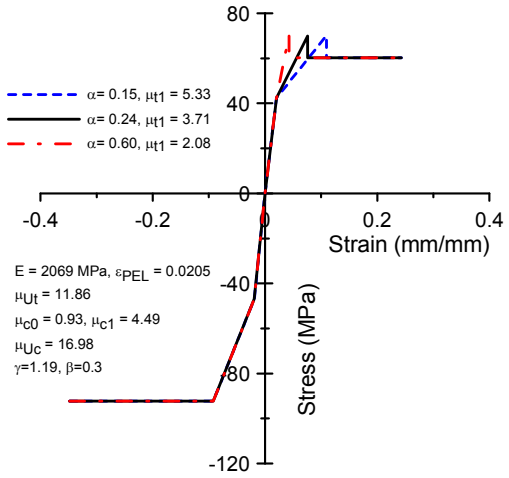

(a)

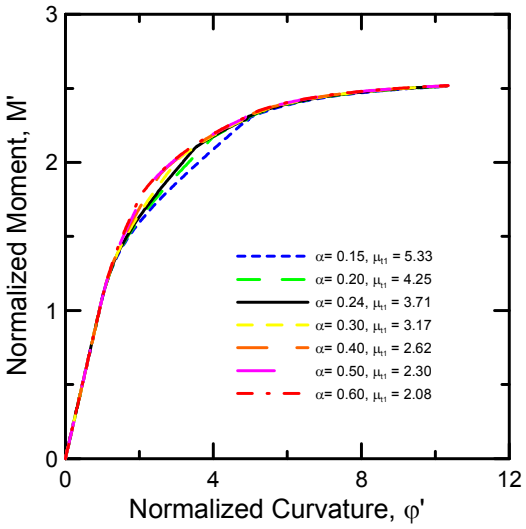

(b)

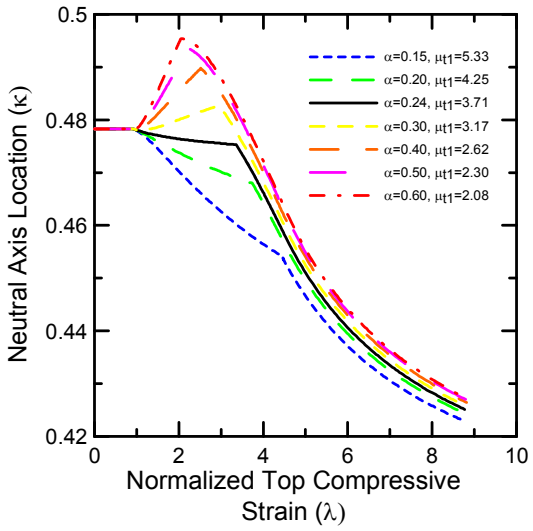

(c)

Fig. 4.17 Effects of strain at constant ultimate tensile stress on moment curvature and location of neutral axis

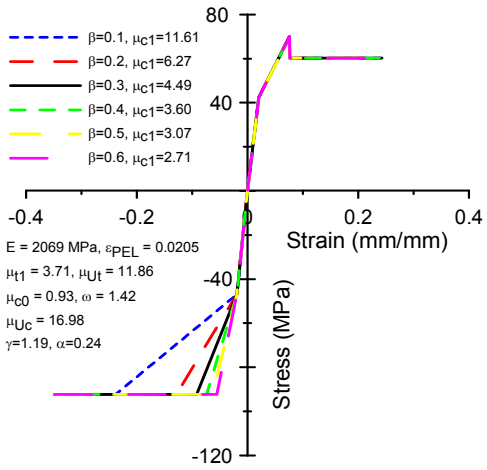

(a)

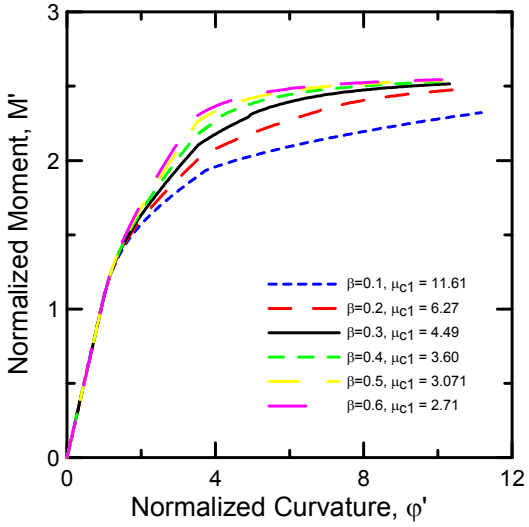

(b)

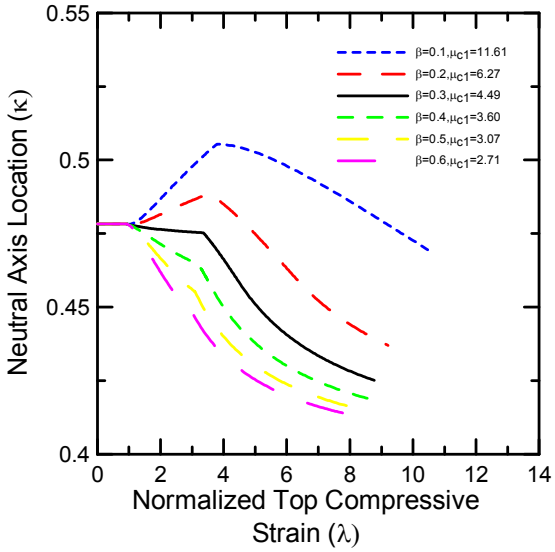

(c)

Fig. 4.18 Effects of strain at constant compression yield stress on moment curvature and neutral axis location

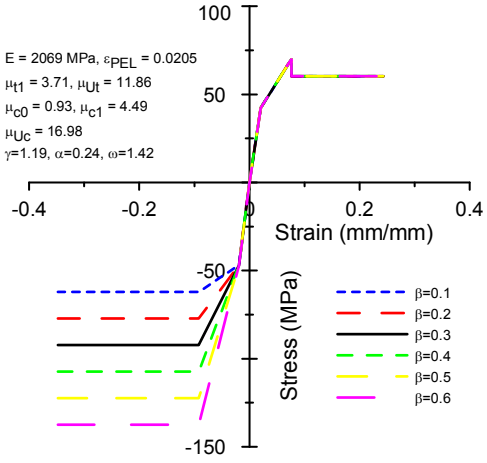

(a)

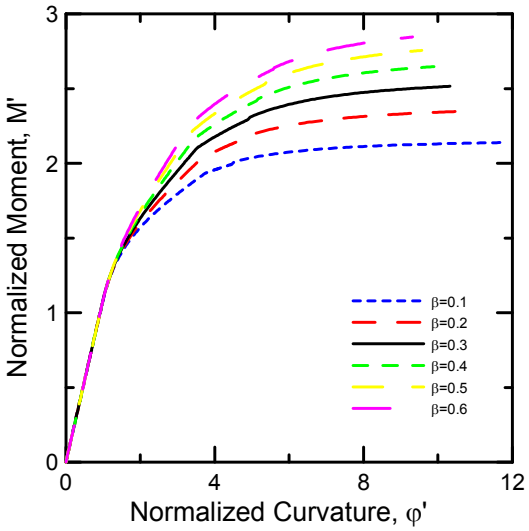

(b)

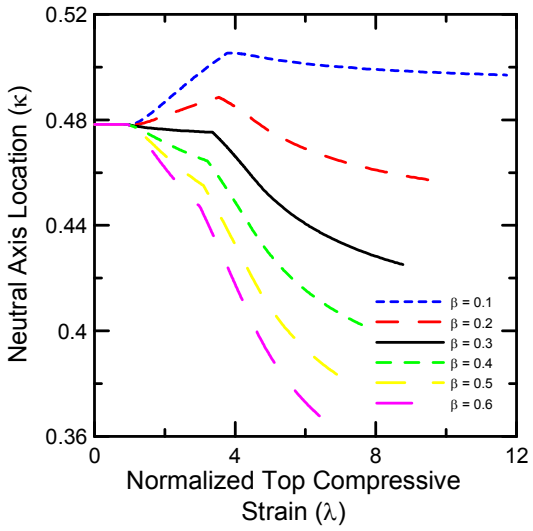

(c)

Fig. 4.19 Effects of compressive yield stress at constant strain on moment curvature and location of neutral axis

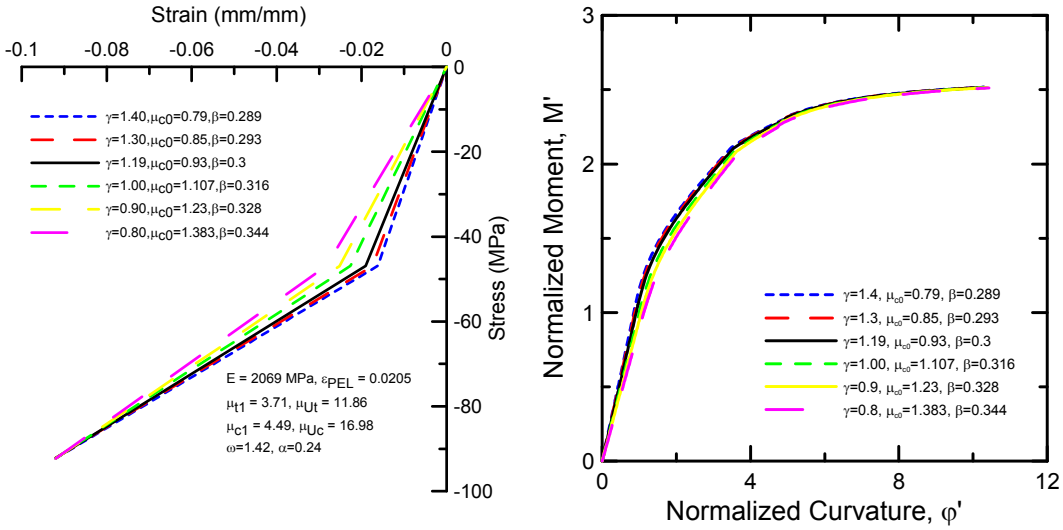

(a) (b)

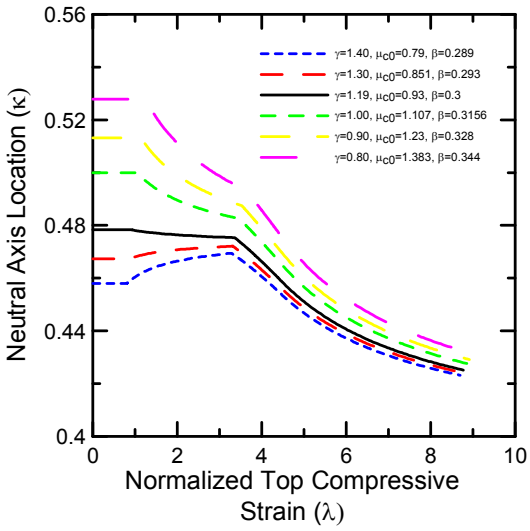

(c)

Fig. 4.20 Effect of strain at constant proportionality elastic limit stress in compression on moment curvature and location of neutral axis

4.3.4. Simplified Model vs. Strain Softening with Plastic Flow Model

Tension, compression, and flexural behaviors of Epon E 863 were studied experimentally in Chapters 2 and 3. It was shown that Epon E 863 demonstrates strain softening behavior followed by almost a constant plastic flow in tension and compression. Also, for this resin material, yield and softening stresses in compression is higher than ultimate and softening stresses in tension. The 14 parameters of strain softening with plastic flow model are defined through curve fitting to represent tension and compression material behavior as shown in Fig. 4.21. These parameters are: E = 3049 MPa, ε_{PEL} = 0.0162, μ_{c0} = 1.148, μ_{c1} = 3.52, μ_{c2} = 6.79, μ_{Uc} = 15.70, μ_{t1} = 2.55, μ_{t2} = 8.64, μ_{Ut} = 20.98, γ = 1.09, α = 0.395, β = 0.298, η = -0.0385 and ξ = -0.117.

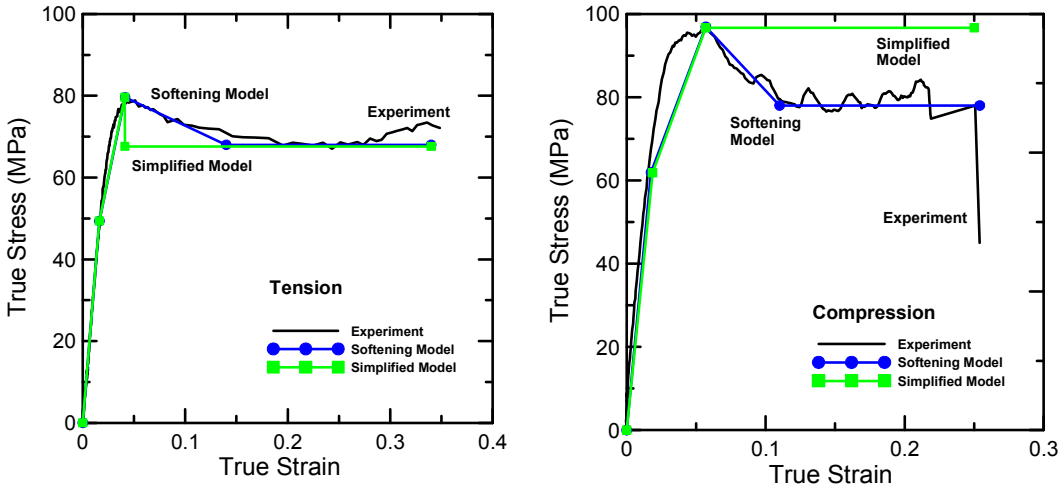

(a) (b)

Fig. 4.21 Experiment, strain softening and simplified stress strain models for E 863 at 493 μstr/sec for (a) tension; and (b) compression

Figure 4.21 also illustrates the simplified tension and compression stress strain curves for E 863 at 493 μstr/sec. The 11 parameters of the simplified models are: E = 3049 MPa, ε_{PEL} = 0.0162, μ_{c0} = 1.148, μ_{c1} = 3.52, μ_{Uc} = 15.70, μ_{t1} = 2.55, μ_{Ut} = 20.98, γ = 1.09, α = 0.395, β = 0.298, and ω = 0.85. Figure 4.22 compares the normalized moment curvature diagram obtained from the full softening model and the constant flow tension and compression stress strain model at 493 μstr/sec. The constant flow stress model slightly differs from the precise full softening model in the pre-peak response. However, it cannot capture the deflection softening behavior observed in the full softening model. Both models show the same moment carrying capacity for E 863, but at different curvatures.

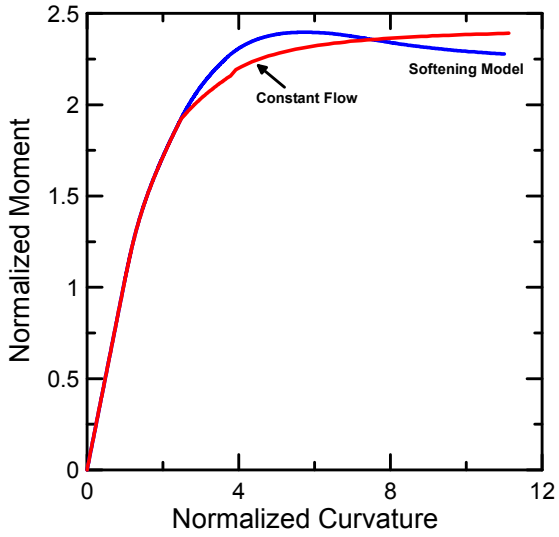

Fig. 4.22 Normalized moment curvature diagram from full softening and constant flow models

The moment curvature response of a beam with groove in the middle in the 3PB setup, obtained through the DIC system is presented in Fig. 4.23. The DIC system shows the location of the neutral axis throughout the loading. Thus, curvature at each step is computed as longitudinal strain at top fiber divided by depth of the neutral axis.

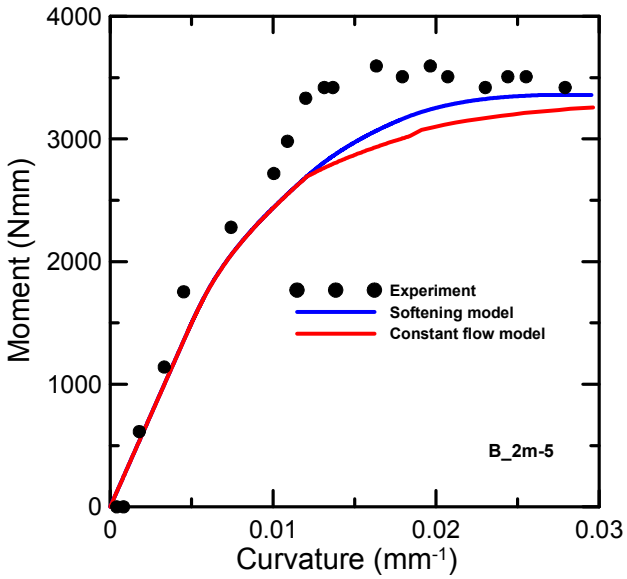

Fig. 4.23 Moment curvature response for B_2m-5 obtained from piecewise-linear uniaxial constitutive models and from DIC system

Figure 4.23 also shows the moment curvature response curves obtained from piecewise-linear uniaxial tension and compression stress strain curves. The full softening model accurately captures tension and compression post-peak stress strain behavior of epoxy resin polymeric materials. However, the moment curvature response shows over-strength in the flexural response. This phenomenon will be explained in more detail in the next sections in an examination of the load deflection response curves. In the domain of the curvature presented in Fig. 4.23, the constant flow tension and compression stress strain model underestimates the experimental curve by approximately 16%.

4.4. Softening Localization

The load deflection response is obtained by using the nonlinear moment curvature response, static equilibrium, and the softening localization concept. In displacement

control, the normalized top compressive strain is incrementally imposed to generate a stress distribution profile in a given cross section. For resins, if the compressive strength is greater than the tensile strength, the shape of the moment curvature diagram greatly depends on the value of the post-peak tensile stress, as observed in the parametric study presented in section 4.2.3. Figure 4.24 shows a typical nonlinear moment curvature diagram for epoxy resins consisting of a linear elastic portion from 0 to $M_{LOP,}$ followed by an ascending curve with reduced stiffness from M_{LOP} to M_{max} in the pre-peak region, and a descending curve from M_{max} to $M_{failure}$ in the post-peak region.

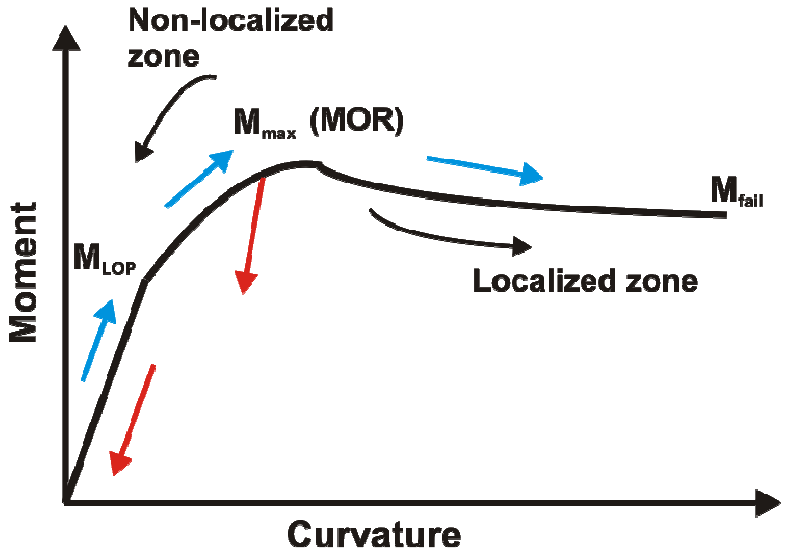

Fig. 4.24 Typical moment curvature for epoxy resin polymeric materials

The first deviation from linearity in a moment curvature or load deflection curve is called Limit of Proportionality (LOP), and the first peak moment or load is called Modulus of Rupture (MOR), as determined in Fig. 4.24. When a beam is loaded beyond MOR in a material exhibiting strain softening behavior, an increase in the deformation decreases load. Polymeric materials are characterized by the existence of a fracture

process zone with distributed cracking damage (Bazant and Chen, 1997) therefore locating the softening zone is extremely important. Figure 4.25 (a) shows a simply supported beam with groove in three point bending (3PB) configuration, with softening localization in the cracking region at the vicinity of the load (region 2). While the material in region 2 experiences softening, other parts of the beam outside the groove (region 1) undergo unloading. Figure 4.25 (b) illustrates the formation of softening localization in 4PB setup. The length of the localization zones has been determined from a strain field analysis using the DIC system.

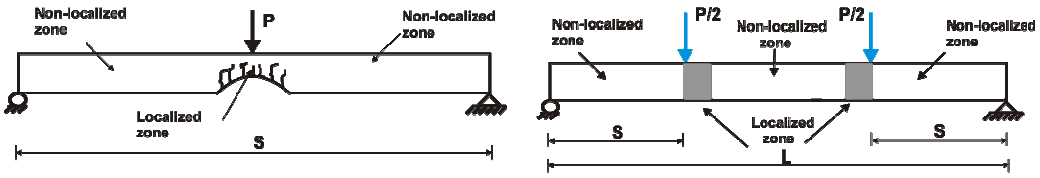

(a) (b)

Fig. 4.25 Softening localization for (a) 3PB; (b) 4PB

4.5. Load Deflection Response

In displacement control quasi-static flexural tests, the deflection is incrementally imposed up to the point of failure. For resins, if no premature failure occurs, the load deflection curve shows a deflection softening behavior in the post-peak part of the response. Chapter 3 showed that a typical nonlinear load deflection response for epoxy resins consists of a linear elastic part from 0 to P_{LOP} followed by an ascending curve with reduced stiffness from P_{LOP} to P_{max} in the pre-peak region and a descending curve from P_{max} to $P_{failure}$ in the post-peak region. In the deflection softening regime, an increase in the deformation decreases load. In the localized softening portions of a structure, the

material follows the descending part of the moment curvature curve shown in Fig. 4.24. For any statically determinate structure, if the complete range of moment in the moment curvature diagram is incrementally imposed on a structure, a complete series of load steps can be obtained. For each load step, the moment diagram along the length of the structure is calculated and the corresponding curvature is obtained from the moment curvature relationship. For a 3PB setup, deflection is calculated using the moment area method or the virtual work method for curvature points at each load step. This procedure is repeated for the number of load steps until a complete load deflection response is obtained.

In the elastic part between 0 and P_{LOP}, the curvature is determined directly from the moment curvature diagram. Beyond the LOP and as the specimen undergoes softening, the curvature distribution depends on the localized or non-localized zones and the prior strain history. If the section is loaded beyond M_{LOP}, the unloading curvature of the damaged section follows an unloading path, as observed by Littell et al. (2008) for E 862 in the cyclic tests. However, since analytical simulation and the experiment are done for 3PB under displacement control, no elastic recovery is assumed. For sections located in the localized zone, the unloading curvature is determined from the descending curve of the moment curvature diagram, from M_{max} to $M_{failure}$. The main steps to calculate load deflection response is summarized as follows:

1. Calculate the transition points to determine the possible cases of stress distribution based on material properties for a piecewise-linear model,

2. Impose load incrementally by increasing the normalized top compressive strain to obtain the nonlinear moment curvature response using closed-form expressions for moment and curvature relevant to the cases in step 1.

3. Calculate the applied load vector (P = 2M/S where S is the span and the distance between a support and adjacent load for the 3PB and 4PB, respectively).

4. Calculate moment diagram along the structure for any load in step 3.

5. Determine curvature diagram for any load in step 3 along the structure using moment curvature relationship, softening localizations, and the percentage of the elastic recovery.

6. Calculate the amount of deflection using one of the methods for statically determinate structures (e.g., virtual work method).

7. Repeat steps 3 to 6 for each load.

4.6. Forward Solution and Inverse Analysis of Load Deflection

Tension and compression constitutive stress strain curves and 3PB bending load deflection curves for epoxy resin Epon E 863 at different strain rates were shown in Chapters 2 and 3. Black solid curves in Fig. 4.26 and 4.27 illustrate the tension and compression stress strain relationship at 493 μstr/sec and 59 μstr/sec, respectively. Distribution of longitudinal plastic strain in the post-peak regime was examined using the DIC system to determine the softening localization. Sections 1 and 2 in Fig. 4.28 shows that the lengths of softening localization at 493 μstr/sec and 59 μstr/sec in the softening stage are 5 mm and 4.5 mm, respectively. The load deflection response of Epon E 863 was simulated using strain softening and constant flow models to evaluate the influences of out-of-plane loading on the constitutive stress strain models.

Blue solid curves in Fig. 4.26 and 4.27 show the strain softening tension and compression models built upon experimental curves through curve fitting. The two main parameters and the 12 non-dimensional parameters for the models at 493 μstr/sec and 59 μstr/sec are: E = 3049 MPa, ε_{PEL} = 0.0162, μ_{c0} = 1.148, μ_{c1} = 3.52, μ_{c2} = 6.79, μ_{Uc} = 15.70, μ_{t1} = 2.55, μ_{t2} = 8.64, μ_{Ut} = 20.98, γ = 1.09, α = 0.395, β = 0.298, η = -0.0385 and

ξ = -0.117 for 493 μstr/sec and E = 2877 MPa, ε_{PEL} = 0.0154, μ_{c0} = 1.331, μ_{c1} = 3.896, μ_{c2} = 6.79, μ_{Uc} = 19.48, μ_{t1} = 2.753, μ_{t2} = 8.05, μ_{Ut} = 19.87, γ = 0.83, α = 0.33, β = 0.285, η = -0.0352 and ξ = -0.122 for 59 μstr/sec.

Green solid curves in Fig. 4.26 and 4.27 show the tension and compression constant flow models. The two main parameters and the 9 normalized parameters for the models at 493 μstr/sec and 59 μstr/sec are: E = 3049 MPa, ε_{PEL} = 0.0162, μ_{c0} = 1.148, μ_{c1} = 3.52, μ_{Uc} = 15.70, μ_{t1} = 2.55, μ_{Ut} = 20.98, γ = 1.09, α = 0.395, β = 0.298, and ω = 1.369 for 493 μstr/sec and E = 2877 MPa, ε_{PEL} = 0.0154, μ_{c0} = 1.331, μ_{c1} = 3.896, μ_{Uc} = 19.48, μ_{t1} = 2.753, μ_{Ut} = 19.87, γ = 0.83, α = 0.33, β = 0.285, and ω = 1.393 for 59 μstr/sec. Since the experimental compression stress strain curve was not available at 59 μstr/sec, the model was built based on the linear relationship between the mechanical properties and the logarithm of the strain rate.

Figures 4.29 and 4.30 show the 3PB load deflection curve compared with the simulation results. These figures illustrate that the tension and compression stress strain curves from both models underestimate the load deflection response due to the difference between the stress distribution profile in the uniaxial tests and the bending test. Simulated load deflection curves obtained from the softening model accurately captures the material behavior showing a bilinear ascending curve to the peak, followed by deflection softening. It must be noted that load deflection curve from the constant flow model cannot capture the post-peak deflection softening response due to an assumption of high compressive flow stress.

In tension and compression tests, the entire volume of the sample is subjected to the same load and has the same probability of failure. However, in a bending test, only a

small fraction of the tension and compression regions are subjected to the maximum peak stress, as shown in Fig. 4.31. Therefore, the probability of crack nucleation, propagation, and failure development in tension and compression samples is higher than in bending samples. Results of the parametric study show that simulation of the flexural response can be improved by changing the ultimate tensile and compressive level and further adjustments to the remaining parameters. In order to quantify these effects, and based on the results of the parametric study, a scaling factor (C_1) is defined as the flexural over-strength factor that modifies the strength of the material.

Imperfections in the material directly affect C_1. However, inverse analyses of the load deflection response showed that C_1 for Epon E 863 for 493 μstr/sec and 59 μstr/sec based on softening model is around 1.14 and 1.24, respectively. Inverse analyses of the load deflection response using the constant flow model indicates higher flexural over-strength factors as 1.3 for 493 μstr/sec and 1.5 for 59 μstr/sec. Blue and green dash lines in Figs. 4.26 and 4.27 show the back calculated tension and compression stress strain curves for strain softening and constant flow models.

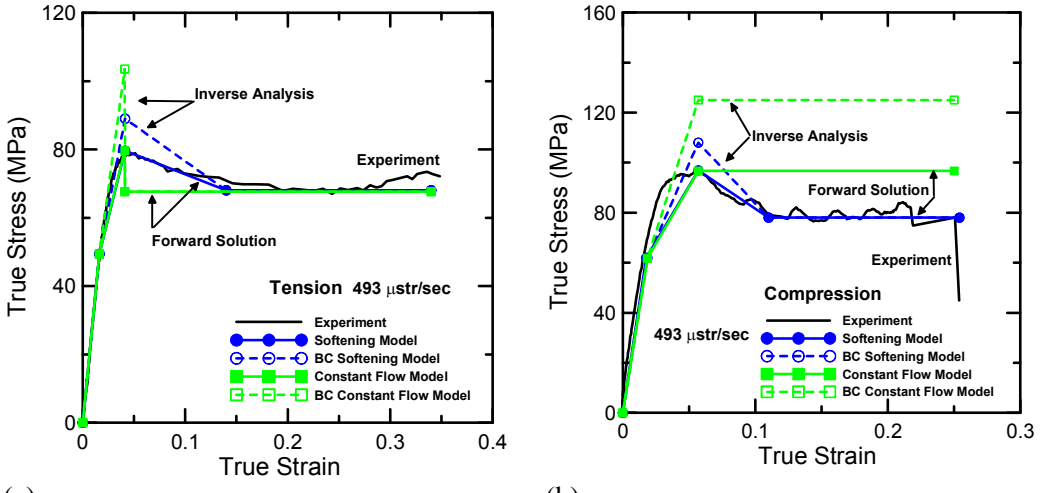

(a) (b)

Fig. 4.26 Experimental and analytical models for tension and compression for E 863 at 493 μstr/sec

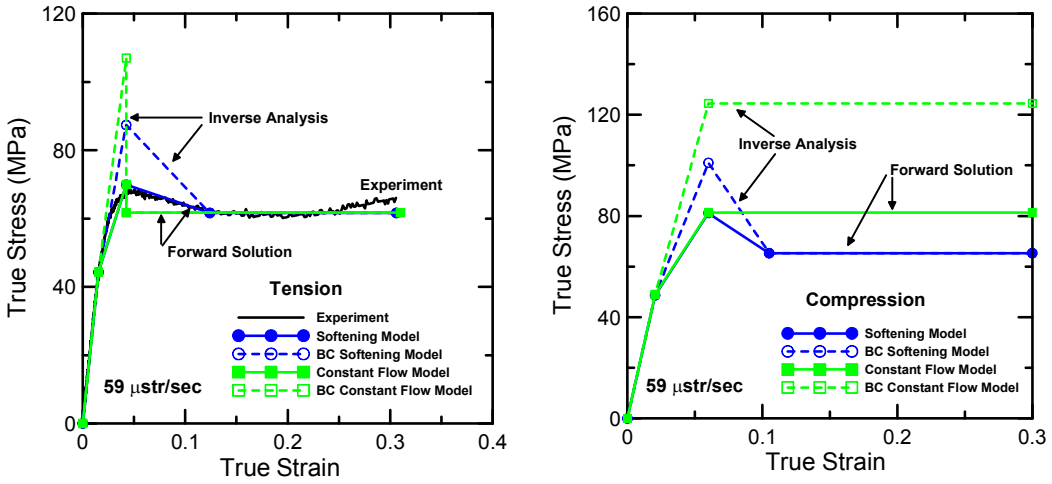

(a) (b)

Fig. 4.27 Experimental and analytical models for tension and compression for E 863 at 59 μstr/sec

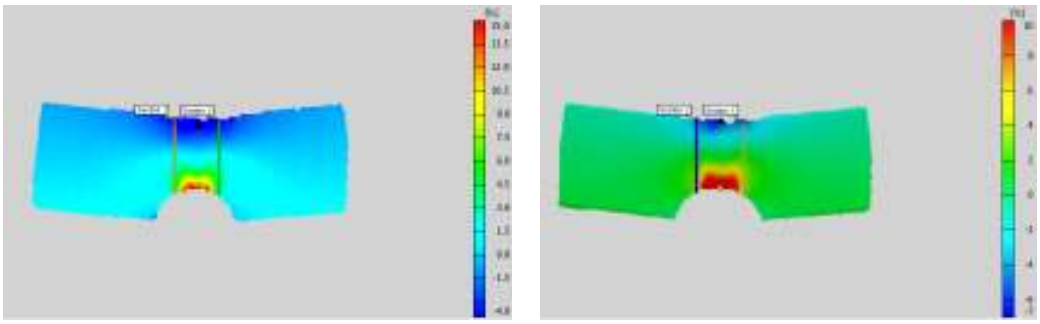

(a) (b)

Fig. 4.28 Softening localization area (a) 493 μstr/sec; (b) 59 μstr/sec

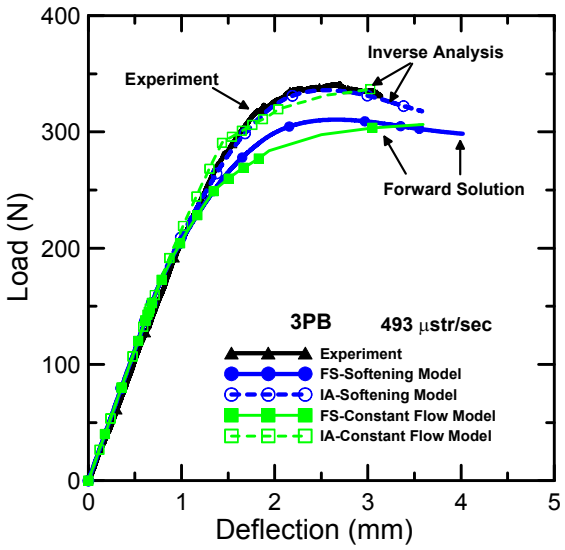

Fig. 4.29 Forward solutions and inverse analysis of load deflection for E 863

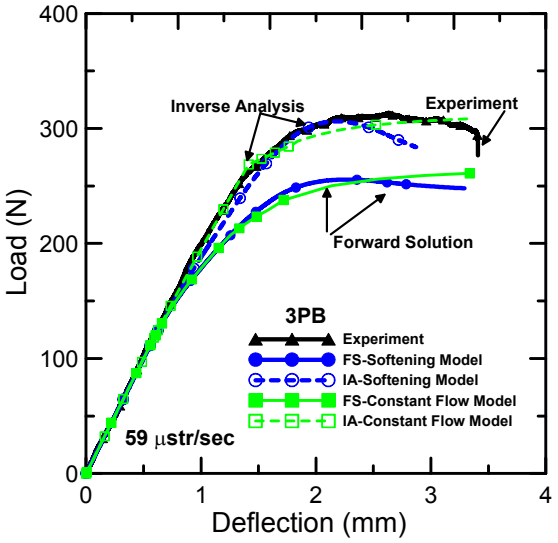

Fig. 4.30 Forward solutions and inverse analysis of load deflection for E 863

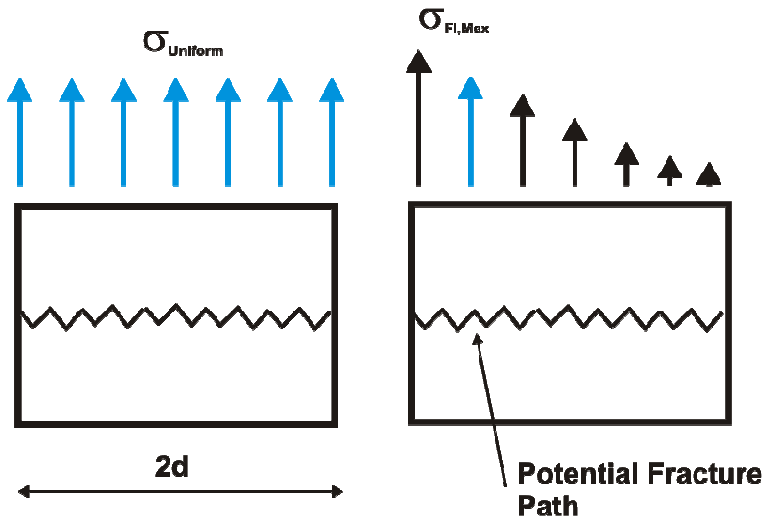

Fig. 4.31 Stress gradient effect on maximum flexural strength

4.7. Location of Neutral Axis in Nonlinear Phase

The location of the neutral axis during loading is an important parameter in the fracture mechanics study of a material. As solving for the static equilibrium during the nonlinear material response, the location of the neutral axis from beginning of loading up to point of failure could be determined. It is possible to experimentally locate the neutral axis by studying the stain field using the DIC system. Figure 4.32 shows the location of the neutral axis in the middle of the beam beneath the loading nose at 493 μstr/sec. The results indicate that the location of neutral axis directly depends on tension and compression strengths in the nonlinear phase. The softening model obtained from the inverse analysis matches with the results obtained from the DIC system.

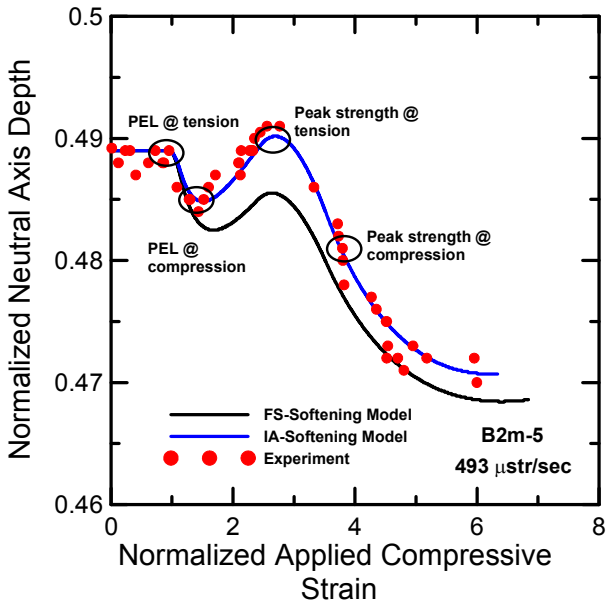

Fig. 4.32 Location of the neutral axis based on the softening model and experiment for E 863 at 493 μstr/sec

4.8. Concluding Remarks

In this chapter, explicit moment curvature equations using nonlinear tension and compression stress strain models for epoxy resin materials have been developed. The first model is a piecewise-linear stress strain relation for epoxy resin materials, consisting of strain softening and flow stress in tension and compression. In this model, the material response is described by two intrinsic material parameters (tensile modulus of elasticity and tensile strain at the PEL point) in addition to five non-dimensional parameters for tension and seven non-dimensional parameters for compression. A parametric study showed that the moment curvature response is primarily controlled by the post-peak tensile and compressive strengths, σ_{UTS}, and σ_{CYS}. It was concluded that compression stress strain parameters have less effect on flexural behavior than tension parameters as

long as compression strength is higher than tension strength. For materials with small post-peak tensile strength values, moment at failure is much less than the moment carrying capacity and the response terminate at a relatively low compressive strain. Materials with higher normalized post-peak tensile strength have a gradual reduction in the height of the compressive zone; therefore, larger deformations are possible. Epoxy resin materials with a considerable amount of post-peak tensile strength have a moment capacity around 2.5 times the moment at the PEL point. An increase of σ_{CYS} by increasing the post-compressive PEL stiffness at high CYS values, marginally affects the moment capacity in polymeric materials. It is observed that the flexural response in polymeric materials that are stronger in compression than in tension is independent of the shape of the compression stress strain curve at high strain values. As a result, a second model is proposed. This model is a piecewise-linear stress strain curve simplified in the post-peak response. It consists of constant flow stress in tension and constant yield stress in compression. While this model captures the pre-peak flexural response, it cannot show the deflection softening for epoxy resin materials. Simulation of the load deflection response of epoxy resins in a 3PB test using the strain softening model revealed the effect of stress gradient on material behavior. Results indicate that direct use of tension and compression data underestimates flexural strength. By applying a flexural scaling factor (C_f) to uniaxial tension and compression strength in stress strain curves, flexural behavior of epoxy resins can be predicted accurately.

5. Mechanical Response of Epoxy Resin Polymeric Structures

5.1. Introduction

It has been shown in chapter 4 that the direct use of tension and compression stress strain models underestimates the flexural strength of epoxy resin materials in 3PB setup. In order to better evaluate the degree of flexural over strength; it is required to analytically and experimentally simulate the flexural behavior of epoxy resin material in other configurations. For accurate analysis of a determinate structure, four point bending (4PB) and round plates supported on three symmetrically arranged pivot points on a circle have been chosen. Dupont and Vandewalle (2004) investigated the use of round plate test as a possible standard test for fiber reinforced concrete composites. Bernard (2006) conducted experiment on plate elements subject to point loading and observed that plasticity in the immediate post-crack range can influence the peak in load resistance. Vandewalle et al. (2009) used round panel mechanical tests to avoid the large scatter in the results of three point bending (3PB) and four point bending (4PB) tests.

There are two main methods of structural analysis which are commonly used to predict the ultimate load. The first method involves a numerical elastic analysis in which calculated stresses are compared to strength of the epoxy resin based on a yield criterion. The second method is the virtual energy-based line method in which the uniaxial flexural capacity of the material at failure (upon cracking) is used together with an assumed pattern of failure to predict the point load capacity. However, the yield line method was originally developed for nominally plastic materials so its application to the prediction of ultimate load in structures made of epoxy resins exhibiting semi-brittle behavior has to be studied. In this chapter, the second method is used to analyze the structural behavior of round plates.

5.2. Four Point Bending (4PB) Structure

5.2.1. *Experiment*

Small beams with the width of 4 mm, thickness of 10 mm, and length of 60 mm (50 mm span) were selected to conduct 4PB tests at loading speed of 493 μstr/sec. Digital image correlation technique (ARAMIS 4M) was used to study the strain fields. The middle span was 25 mm in the 4PB setup. Figure 5.1 shows 4PB experimental setup. Figure 5.2 illustrates the load deflection curves from the experiment with the average and the standard deviations. Curves "Avg." and "Avg.-std" are used as the representative experimental curves for the simulation in the next sections.

Fig. 5.1. Experimental setup in 4PB tests

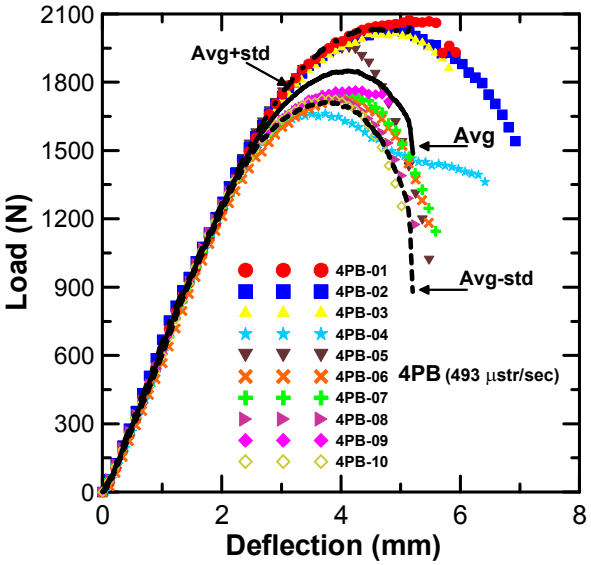

Fig. 5.2. Load deflection response in 4PB configuration at 493 μstr/sec

5.2.2. Load Deflection Response for 4PB

As stated before, the first deviation from linearity in a moment curvature or load deflection curve is called Limit of Proportionality (LOP). The specimen is loaded from 0 to P_{LOP} in the linear portion of the moment curvature diagram. The curvature for this portion is determined directly from the moment curvature diagram. Beyond the LOP, the curvature is obtained from the nonlinear portion of the moment curvature diagram. Static equilibrium is used to obtain a series of load steps in 4PB setup from the moment curvature diagram. The main steps to calculate load deflection response in 4PB are summarized as following.

1. Specify tension and compression stress strain curves having assumed material properties for the piecewise-linear models and calculate the transition points to determine the possible cases of stress distribution as it was shown for 3PB

2. Use the strain compatibility analysis to calculate the neutral axis location and to obtain the moment curvature diagram

3. Calculate the applied load vector (P_i) using static equation P = 2M/S from discrete points along the moment curvature diagram where S is the distance between a support and the adjacent load for the 4PB

4. Divide beam into number of sections

5. Calculate moment M(i,j) at discrete sections along the beam for any load in step 3

6. Determine curvature from moment curvature diagram for each discrete section (j) and for any load step (i) considering the softening localization length and the percentage of the material recovery

7. Calculate the amount of deflection using one of methods for statically determinate structures (e.g. virtual work method)

8. Repeat steps 3 to 7 for each load.

Softening localization zone is determined using DIC system. Figure 5.3 shows the distribution of the longitudinal strain (ε_x) and the development of softening localization throughout applying load. Sections in Fig. 5.3 show the location of the loading noses and the center of the beam. The marked areas around the loading noses show that plastic length is around 4.7 mm in 4PB beams. Plastic length obtained from DIC is used for the simulations. Figure 5.4 (a) shows the locations of the softening zone in the model. It must be noted that the part of the softening localization in the middle span has been considered for the simulation. Figure 5.4 (b) exhibits the curvature distribution at yield, maximum, and failure stages along the beam. It illustrates the effect of the softening localization on the amount of curvature in the post-peak response.

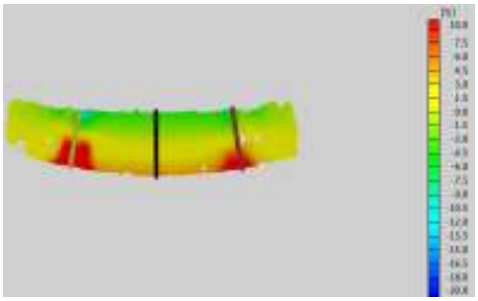

(a) stage 80

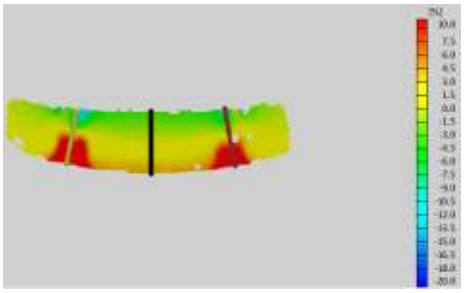

(b) stage 90

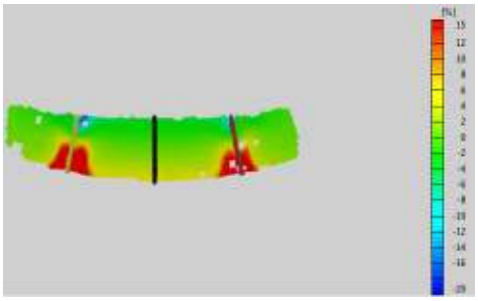

(c) stage 100

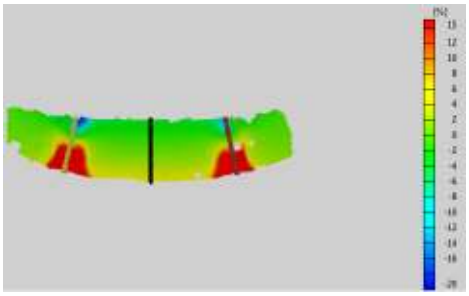

(d) stage 110

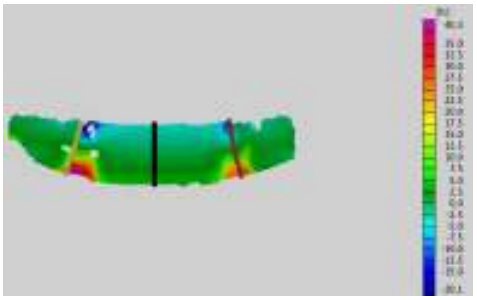

(e) stage 115

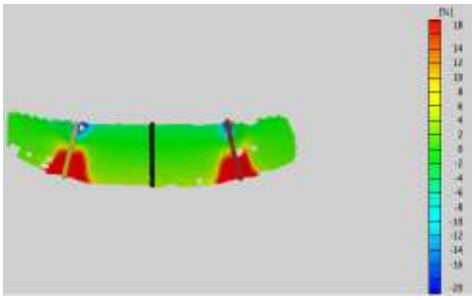

(f) stage 120

Fig. 5.3. Development of softening localization throughout applying load

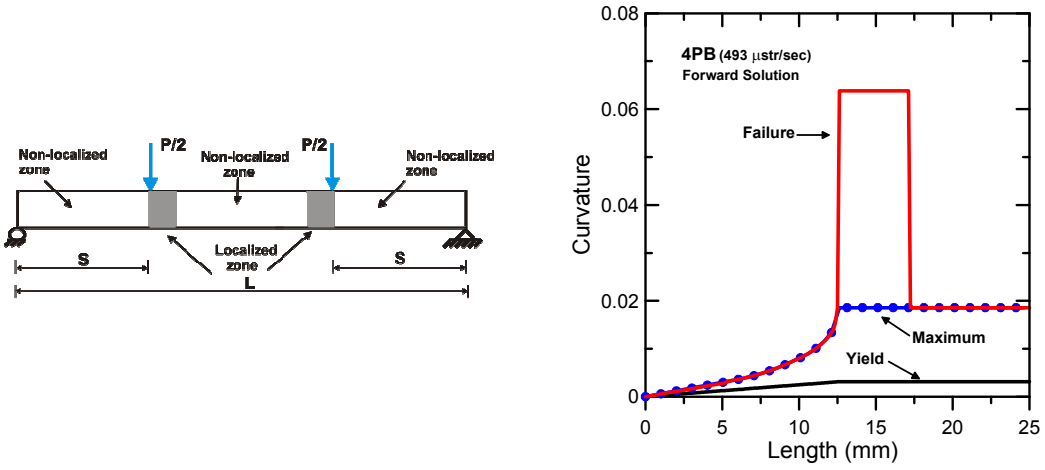

(a) (b)

Fig. 5.4. (a) Model of the softening localized zone in 4PB beam; (b) Curvature distribution at yield, maximum and failure stage

5.2.3. Forward Solution and Inverse Analyses of 4PB Structural Response

Figure 5.5 illustrates the representative experimental tension and compression true stress strain curves at 493 μstr/sec. As stated before, Epon E 863 has a strain softening behavior in tension and compression. Therefore, the softening model was built through curve fitting as shown in black solid line in Fig. 5.5. The two main parameters and nine non-dimensional parameters for the model at 493 μstr/sec are: E = 3049 MPa, ε_{PEL} = 0.0162, μ_{c0} = 1.148, μ_{c1} = 3.52, μ_{c2} = 6.79, μ_{Uc} = 15.70, μ_{t1} = 2.55, μ_{t2} = 8.64, μ_{Ut} = 20.98, γ = 1.09, α = 0.395, β = 0.298, η = -0.0385 and ξ = -0.117. Simulations were made to study the flexural load deflection response of epon E 863 and to evaluate the flexural over-strength factor in 4PB response. Figure 5.6 show the load deflection curves obtained from forward solution, inverse analysis, calibrated parameters from 3PB, and the experiments. As stated before, the uniaxial tension and compression stress strain curves underestimate the load deflection response due to the difference between stress

distribution profile in uniaxial tests and the bending test. Figures 5.5 and 5.6 showed that the proposed flexural over-strength factor (parameter C_1) to modify the uniaxial tension and compression stress strain curves for flexural simulation is higher in 4PB comparing to the 3PB with groove.

Inverse analysis of the 4PB load deflection response showed that the value of C_1 for Epon E 863 is around 1.52. The reason for having a higher factor in 4PB than 3PB is that in 3PB with a groove or notch at the center, the beam is forced to fracture at the location of groove or notch due to some stress concentration. However, center of the beam may not be the weakest point in the beam so groove and notch may influence the actual strength of the material.

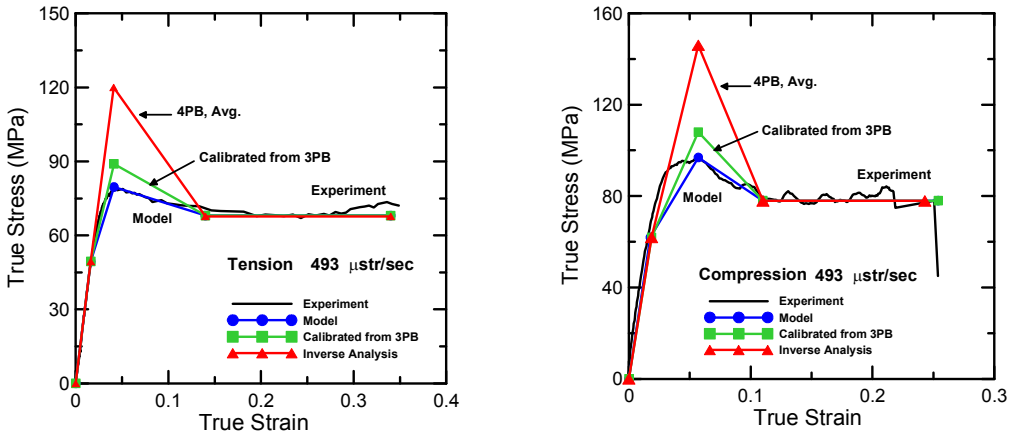

(a) (b)

Fig. 5.5. Tension and compression stress strain models from experiment, model, parameters calibrated from 3PB, and inverse analysis of 4PB

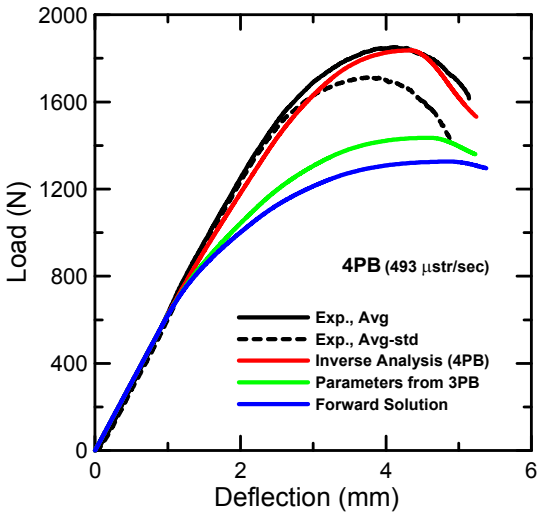

Fig. 5.6. Load deflection response obtained from forward solution, calibrated parameters from 3PB and the inverse analysis

5.3. Structural Response of Epoxy Resin Plates

5.3.1. Experiments

The experimental study involves production of round epoxy resin plates. The round panel test is performed on polymeric specimens with diameters of 56 mm and 29 mm and a thickness of approximately 2.9 mm as shown in Fig. 5.7(a). A support has been fabricated for the round plate tests. Plates are supported on three symmetrically arranged pivot points on a circle as shown in Fig. 5.7 (b). Plates are loaded with a point load at the center in displacement control as shown in Fig. 5.8. While testing, the load carried by the polymeric plate is recorded by means of a load cell. The displacement of the actuator is also recorded. The test is displacement controlled by means of the central displacement. The cast and cure procedure used previously in chapters 2 and 3 were used to fabricate the round plates to ensure that the mechanical properties developed were very similar. Figure 5.9 shows the experimental load deflection curves of round plates at 493 μstr/sec.

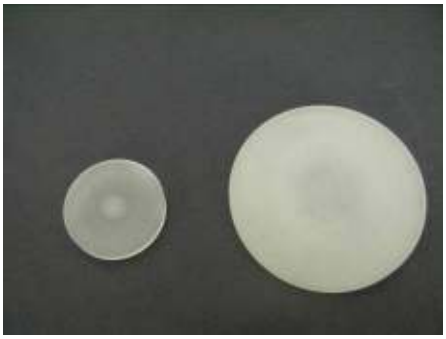

(a) (b)

Fig. 5.7. (a) Round plate specimens; (b) Fixture for round plate tests on three symmetric supports

Fig. 5.8. Deflection of round plate with diameter of 29 mm under point load

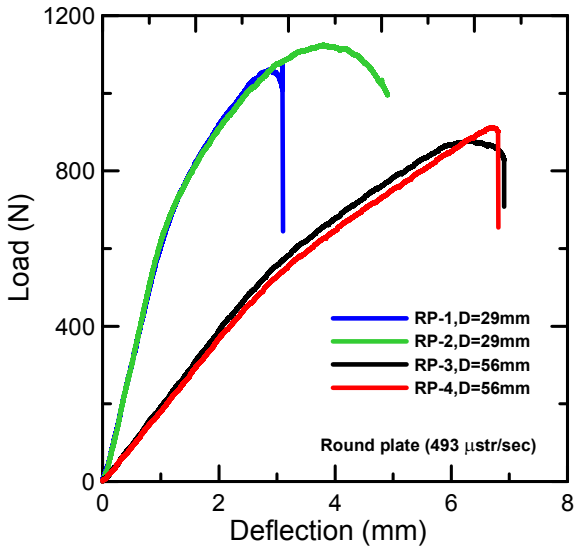

Fig. 5.9. Load deflection of round plates with diameters of 29 mm and 56 mm at 493 μstr/sec.

5.3.2. Yield Line Analysis

The yield line method is popularly used to determine the load capacity in many types of folding plate structures because it is computationally simple and has been proven accurate for the prediction of collapse loads in many types of structures (Jones and Wood, 1967). The yield line pattern which consumes the least amount of energy is considered the collapse pattern. As can be seen in Fig. 5.10 (a), the round plate is almost symmetrically divided into 3 parts. Each part rotates around a rotation axis through the support point. In other words, the governing mode of failure is taken to comprise three symmetrically arranged yield line (cracks) emanating from center of the opposite and bisecting each sector between adjacent pivot supports as shown in Fig. 5.10 (b). Along the yield lines a yield line moment M_p is acting. M_p is calculated based on the static equilibrium of bending moments for a stress distribution profile through a cross section as shown in chapter 4. The yield line moment is expressed as a moment per unit length.

The external virtual work associated with the introduction of the central point load U_{ext} is equated to the internal virtual work U_{int} to find the unknown load resistance P.

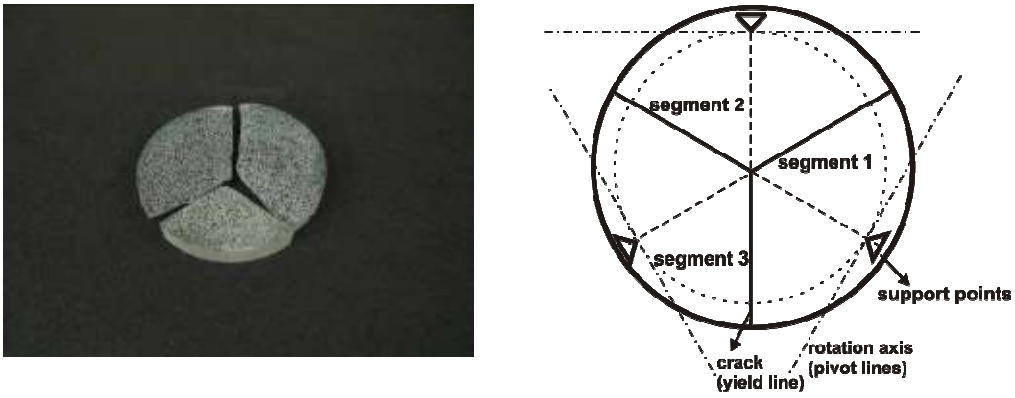

(a) (b)

Fig. 5.10. (a) Round plate specimen after failure; (b) Crack patterns for round plate subject to point load

5.3.3. Load Carrying Capacity

If the moment of resistance per unit length M_p at each yield line is held to be constant, the internal energy (U_{int}) for round plate is calculated as

$$U_{\text{int}} = 6\int_0^{R_1} M_p \theta \, d_x \tag{5.1}$$

$$M_p = M_{PEL}\, M'_{\max}\left(\lambda,\gamma,\beta,\xi,\alpha,\eta,\mu_{c0},\mu_{c1},\mu_{c2},\mu_{t1},\mu_{t2},\mu_{Ut},\mu_{Uc}\right) \tag{5.2}$$

$$M_{PEL} = \frac{h^2 E \varepsilon_{PEL}}{6} \tag{5.3}$$

where x is distance along each radial crack, R_1 is the radius of the round plate, θ is the angle of rotation, h is the thickness of the plate, and $M'_{\max}$ could be obtained from the normalized moment curvature curves shown in Fig. 5.11,hence

$$U_{\text{int}} = 6\cos(30)\frac{M_p R_1 \delta}{R} \tag{5.4}$$

where R is the radius of circle on which the pivots are located at. The external energy due to the central point load P and central deflection δ is

$$U_{ext} = P\delta \tag{5.5}$$

Hence the load associated with cracking in round plate is

$$P = 6\cos(30)\frac{M_p R_1}{R} \tag{5.6}$$

Figure 5.11 (a) shows the round plate and the virtual beam (AB) used to obtain a relationship between rate of loading (dδ/dt) and the strain rate (dε/dt). The deflection at point E, which is smaller than the deflection δ in the center of the plate, is related to the strain along the virtual beam AB as follow.

$$\delta_E = \delta\cos(30)^2 = \frac{3}{4}\delta \tag{5.7}$$

$$\theta = \frac{\delta_E}{BE} = \frac{\delta\cos(30)}{R} = \frac{w/2}{h - \kappa h} \tag{5.8}$$

where κ is the normalized height of the compression zone. Since w is equal to ε_x Lp, then the deflection rate could be calculated as follow.

$$\frac{d\delta}{dt} = \frac{R\,Lp}{2\cos(30)(1-\kappa)h}\frac{d\varepsilon_x}{dt} \tag{5.9}$$

The above equation will be used together with estimates of M_p based on nonlinear material parameters to develop predictions of the load resistance associated with cracking in round plate tests.

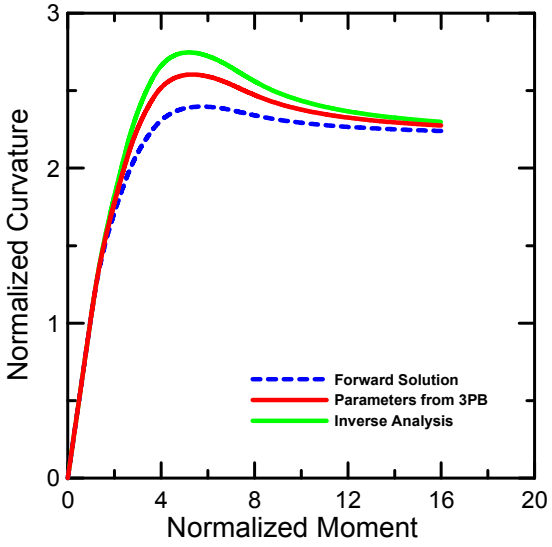

Fig. 5.11. Normalized moment curvature diagram for E 863

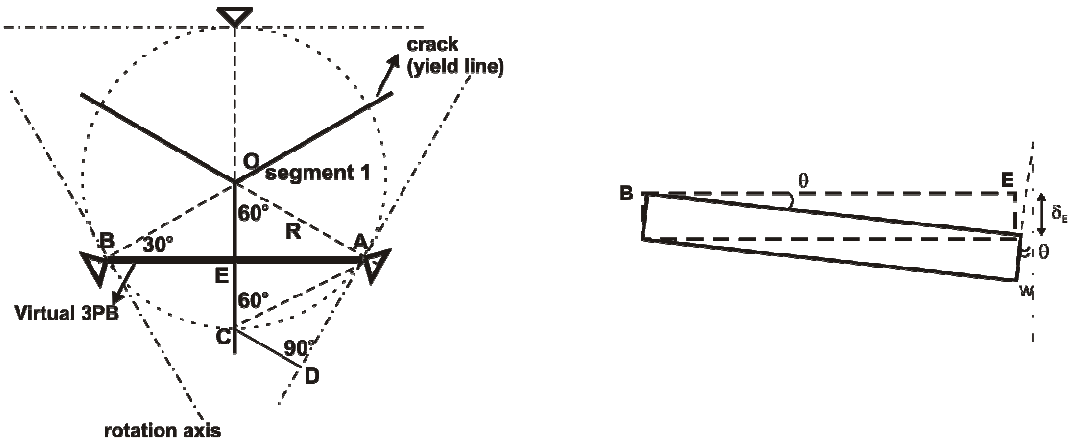

(a) (b)

Fig. 5.12. (a) Round plate and virtual 3PB beam; (b) Relation between rate of deflection and strain rate

5.3.4. Load Deflection Response of Plates

When a point load is introduced to an epoxy resin plate, the element suffers flexural stress actions and deformation around the point of loading. When the combined stress according to the yield criterion exceeds the maximum tensile stress of the material, cracks, usually immediately opposite the point of loading, propagate through the thickness and from the center toward the edge of the plate, as shown in Fig. 5.13. Figure 5.13 shows the evolution of compressive strain along the diagonal crack and on the opposite side of the crack. When the three cracks reach the edge of the plate, it will fracture. The angle of the rotation between two faces of each crack varies along the length of the crack, and the corresponding plastic moment will vary if the epoxy resin material exhibits anything other than perfectly plastic behavior in the post-peak portion of the stress strain curve.

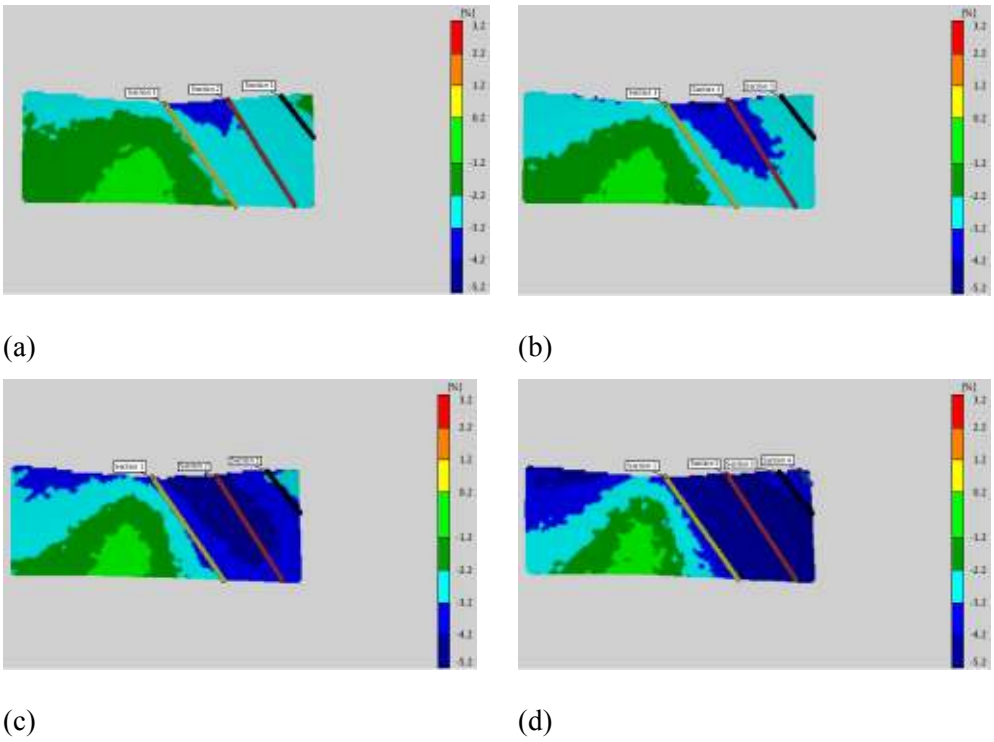

(a) (b)

(c) (d)

Fig. 5.13. Evolution of compressive strain on the top surface up to failure

For Epon E 863, tensile plastic stress in the post-peak response is around 80% of the ultimate tensile stress, while the compressive plastic flow starts from around 80% of the compressive yield stress right after the peak stress but decreases gradually in the high range of strains. However, results in chapter 4 showed that for epoxy resin materials which are stronger in compression than in tension, the compressive plastic flow has the least influence on the plastic moment in the post-peak response. This is the main reason that the normalized plastic moment, shown in Fig. 5.11, is almost constant after a drop immediately in the post-peak response. Therefore, it is assumed that the angle of the rotation between two faces of each crack and the corresponding plastic moment are constant along the length of the crack.

Since there is not any design parameter or a constitutive relation derived from the round panel test results, it is necessary to link the round panel test results to 3PB results. In this section a method is explained how the uniaxial nonlinear tension and compression stress strain curves can be used to predict the structural response of round plates. It is necessary to make some general assumptions as follows:

(i) In round plates, it has been assumed that the panel suffers three symmetric radial cracks, each of which bisects the 120° sector between each pair of support pivots.

(ii) Each un-cracked sector of the specimen has been assumed to experience negligible deformation compared to the cracks and therefore essentially remains plane.

(iii) Yield line theory has been assumed capable of adequately modeling both the cracking and post cracking load capacity of the panel.

In order to establish a link between round plate test and the 3PB test, a virtual beam (imaginary line) is assumed from a support perpendicular to the yield line as shown in Fig. 5.12. The methodology is explained as follows:

(a) Specify compressive and tensile piecewise-linear stress strain models

(b) Apply strain compatibility and stress strain model to calculate location of the neutral axis and obtain moment curvature diagram

(c) Conduct 3PB test to obtain the load deflection information

(d) Conduct inverse analysis to obtain moment curvature curve and tension and compression stress strain model

(e) Obtain moment rotation relationship based on plastic length and curvature

(f) Obtain new moment rotation relation if the depth of the beam differs from thickness of the plate using the same calibrated material parameters.

(g) Obtain the moment rotation per unit width and predict load deflection response of the plate using rigid crack plate model.

Rigid crack model will be used to calculate the load deflection response of a round plate. Figure 5.12 (a) shows the relationship between deflection at the edge and at the center. Segment 1 rigidly rotates around the axis AD. Deflection at the corner point C is calculated as:

$$\frac{\delta_C}{\delta_O} = \frac{DC}{AO} = \frac{R\sin(30)}{R} = \frac{1}{2} \tag{5.10}$$

$$\delta_C = \frac{\delta}{2} \tag{5.11}$$

In rigid crack panel model, each crack segment is rigid and it rotates around the crack axis represented by vectors V_{OA}, V_{OB}, and V_{OC} as shown in Fig. 5.14.

$$V_{OA} = \begin{cases} 0 \\ -R \\ \delta/2 \end{cases} \qquad V_{OB} = \begin{cases} R\cos(30) \\ R\sin(30) \\ \delta/2 \end{cases} \qquad V_{OC} = \begin{cases} -R\cos(30) \\ R\sin(30) \\ \delta/2 \end{cases} \quad (5.12)$$

The vectors normal to the crack segments 1 and 2 can be calculated by cross product of the two adjacent vectors.

$$n_1 = v_{OA} \times v_{OB} = \left(\frac{-\sqrt{3}\,R\delta}{4}, \frac{3R\delta}{4}, \frac{\sqrt{3}\,R^2}{2} \right) \tag{5.13}$$

$$n_2 = v_{OB} \times v_{OC} = \left(\frac{-\sqrt{3}\,R\delta}{4}, \frac{-3R\delta}{4}, \frac{\sqrt{3}\,R^2}{2} \right) \tag{5.14}$$

The rotation θ between segments 1 and 2 is the angle between the two normal vectors determined from the dot product of vectors n_1 and n_2.

$$\theta = \cos^{-1}\left(\frac{n_1 \bullet n_2}{|n_1||n_2|} \right) \tag{5.15}$$

$$\theta = \cos^{-1}\left(\frac{2R^2 - \delta^2}{2R^2 + 2\delta^2} \right) \tag{5.16}$$

The rotation of the crack line is calculated as the central deflection of the plate is incrementally imposed. Knowing the rotation of the yield line from Equation (5.16), the moment per unit width is obtained from the moment rotation relationship obtained from the 3PB test. Using principal of virtual work, the amount of load at each increment of the deflection is as follows.

$$P_i = \frac{3R m_i \theta_i}{\delta_i} \tag{5.17}$$

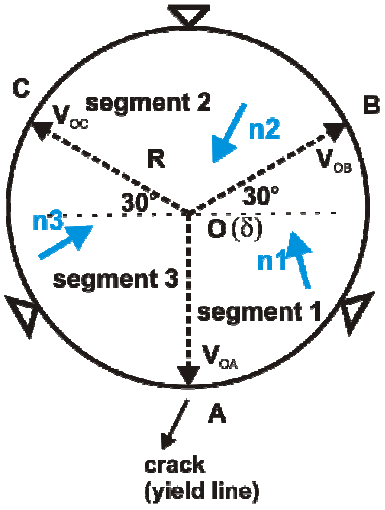

Fig. 5.14. Crack rotation based on rigid crack model

Figure 5.15 illustrates the distribution of the compressive strain at the top surface of the plate and growth of the plastic length throughout the applying load. It shows that the plastic length increases rapidly from stage 125 to stage 178 and it is almost constant from stage 178 to stage 278 where the plate fractures. Thus, the assumption of having a constant angle of rotation between two faces of each crack along the length of the crack is correct in a major part of the post-peak response. Figure 5.16 shows the tension and compression stress strain curves of Epon E 863 obtained from softening model curve-fitted to the experimental curves. Figure 5.17 illustrates that direct use of tensile and compressive uniaxial stress strain curves underestimates the actual load deflection response. Inverse analysis of the experimental load deflection curves for plates with diameters of 29 mm and 56 mm indicates that the flexural over-strength factor (C_1) is around 1.20.

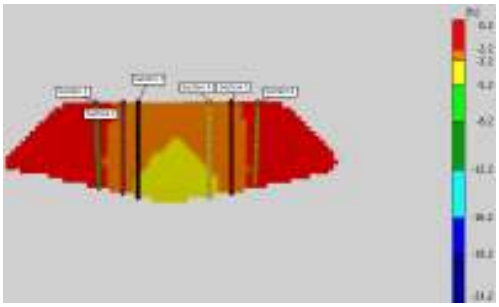

(a) stage 125

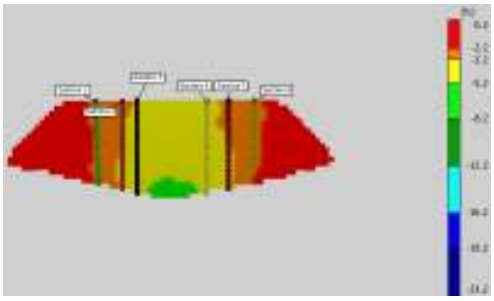

(b) stage 150

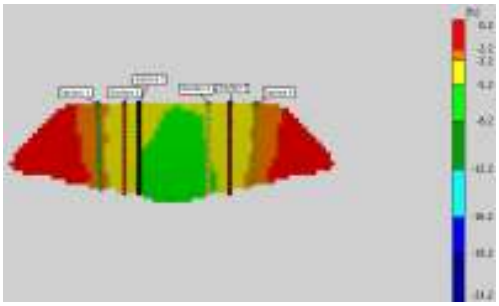

(c) stage 178

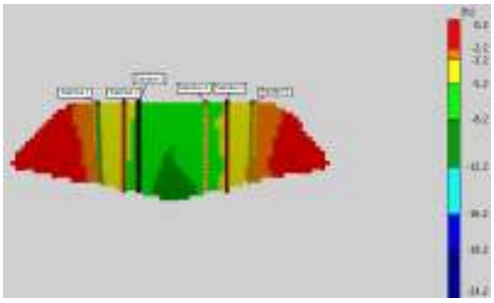

(d) stage 200

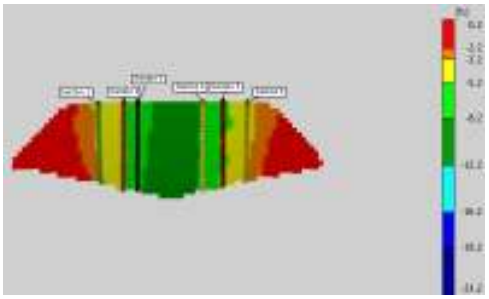

(e) stage 220

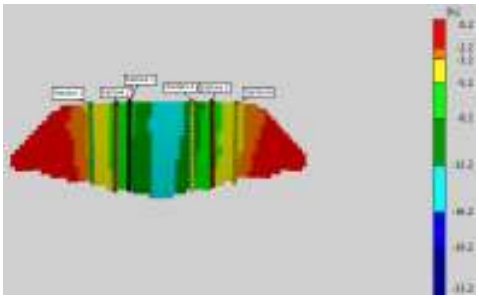

(f) stage 240

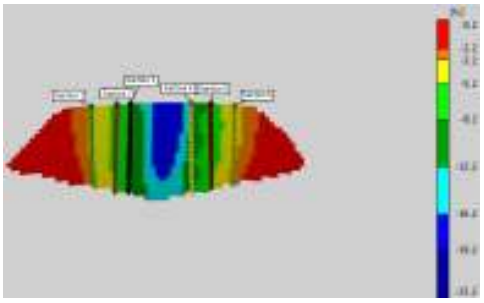

(g) stage 260

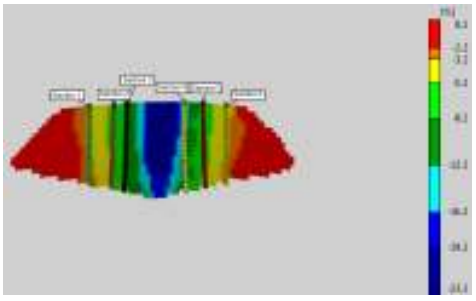

(h) stage 278

Fig. 5.15. Evolution of the compressive strain and growth of the plastic length throughout the applying load

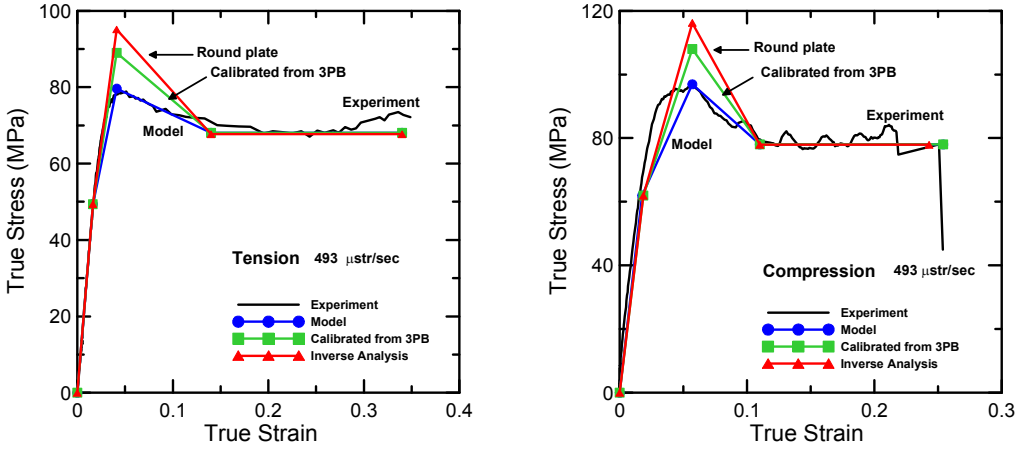

(a) (b)

Fig. 5.16. Tension and compression stress strain curves for round plate

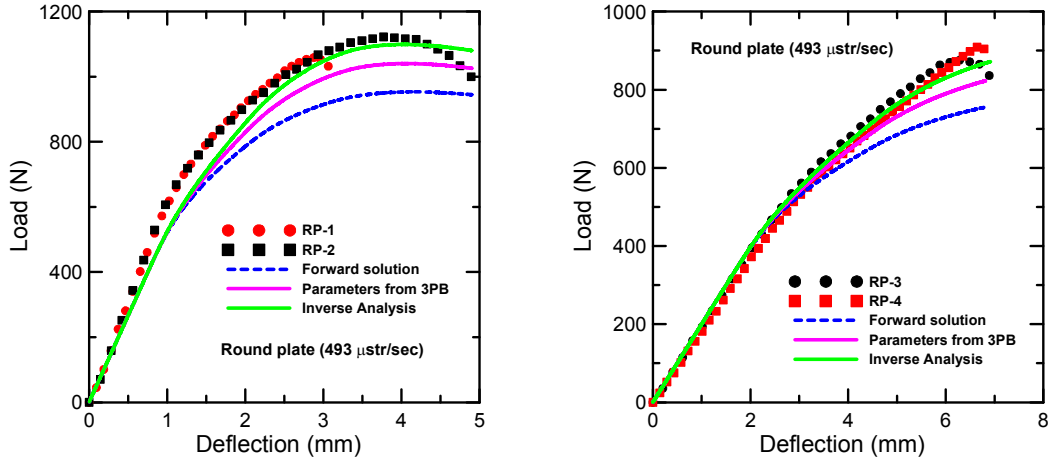

(a) (b)

Fig. 5.17. Load deflection obtained from forward solution, calibrated parameters from 3PB and inverse analysis at 493 μstr/sec with diameter of (a) 29 mm; (b) 56 mm.

5.4. Concluding Remarks

As Epon E 863 exhibits significant amount of plasticity along each radial crack in the round plates, the level of resistance presented by the governing failure mechanism remains constant over the entire deformations associated with the introduction of load. Therefore, the combination of the yield line and the virtual work methods could be used to obtain the nonlinear load deflection response. An algorithm has been developed to correlate the load deflection response in 4PB and round plates with the nonlinear uniaxial tension and compression stress strain curves. The load deflection response of epoxy resin beams in 4PB set-up and round plates supported on three symmetrical pivots showed the effect of stress gradient on the flexural load carrying capacity. Results indicate that direct use of tension and compression data underestimates the flexural strength. Like 3PB, the prediction of flexural load carrying capacity in 4PB and round plate can be improved by applying a scaling factor (C_1) to uniaxial tension and compression strength. However, the value of C_1 is higher for 4PB and round plate than 3PB due to the effect of stress concentration at the location of groove and the short fracture path in 3PB beam.

6. Contributions and Future Work

The primary objective of this dissertation is to investigate the nonlinear inelastic mechanical behavior of epoxy resin polymeric materials. Experiments have been conducted and constitutive stress strain relationships have been developed to model the flexural behavior of the constituent materials, which is critical to the overall response of polymer matrix composite structures under different loading conditions.

6.1. Contributions

The tension and compression mechanical properties of epoxy resin with different specimen shapes and at different strain rates have been investigated. Initially, the stress strain response is found to be linear, indicating elastic behavior, followed by nonlinear plastic deformation. Plastic deformations are observed in thin samples when a non-contact digital image correlation system (DIC) is used for measuring deformation and strain. Epoxy resin Epon E 863 shows high failure strain in tension. However, considerable experimental scatter associated with fracture due to crazes is observed in tension samples. Failure due to crazing is observed while the material deformed plastically. Cubic, prismatic, and cylindrical samples show different compression behavior. Cubic samples, after reaching the compressive yield stress, show a gradual drop in the stress strain curve followed by strain stiffening at high strain values. The cubic samples reach a fracture stress much higher than their yield stress. In the prismatic and cylindrical samples, the shape after the test is not barrel-like; therefore, it is correct to assume a pure uniaxial compressive state of stress due to minimum constrained areas. Results of the compression tests show that a prismatic sample with aspect ratio greater than two results in much better uniaxial compressive state of stress compared to cubic

samples. Strain rate influences the mechanical behavior of epoxy resin materials. An increase in the strain rate increases peak stress in tension and compression and modulus of elasticity. The strain at yield is found to be relatively less sensitive to strain rate in Epon E 863. Strain at failure of polymeric specimens decreases as speed of load increases, therefore, ductility decreases considerably. Results show that PEL in compression and tension could be estimated between 59% and 66% of CYS and UTS for low, medium, and high strain rates.

The DIC system was used to accurately provide strain field information in 3PB tests of polymeric materials. Effects of notches on strain distribution and stress concentration are not negligible. Stress concentration due to notch changes the strain distribution in the beams while groove reduces the stress concentration considerably. An increase in rate of loading increases the initial stiffness and modulus of rupture (MOR). Epoxy resin polymeric materials have a nonlinear nature. Quantitative estimates show that the stress at limit of proportionality (LOP) is around 72% of stress at MOR.

Epoxy resin materials exhibit the following distinct stages in the tension and compression stress strain behavior: linearly elastic, nonlinearly elastic, yield-like (peak) behavior, strain softening, and nearly perfect plastic flow. Explicit moment curvature equations using 2 models for nonlinear tension and compression stress strain models for epoxy resin materials are developed. The first model is a piecewise-linear stress strain relation for epoxy resin materials, consisting of strain softening and flow stress in tension and compression. In this model, the material response is described by two intrinsic material parameters (tensile modulus of elasticity and tensile strain at the PEL point) in addition to five non-dimensional parameters for tension and seven non-dimensional parameters for compression. Parametric studies show that the moment curvature response

is primarily controlled by the post-peak tensile and compressive strengths, σ_{UTS}, and σ_{CYS}. Compression stress strain parameters have less effect on flexural behavior than tension parameters as long as compression strength is higher than tension strength. Materials with high normalized post-peak tensile strength have a gradual reduction in the height of the compressive zone; therefore, larger deformations are possible. Epon E 863 with a considerable amount of post-peak tensile strength has a moment capacity around 2.5 times the moment at the PEL point. Flexural response in polymeric materials that are stronger in compression than in tension is independent of the shape of the compression stress strain curve at high strain values. As a result, a second model is proposed. This model is extremely useful when complete information of the post-peak material behavior is not available. This model is a piecewise-linear stress strain curve simplified in the post-peak response. It consists of constant flow stress in tension and constant yield stress in compression. While this model captures the pre-peak flexural response, it cannot show the deflection softening for epoxy resin materials. Simulation of the load deflection response of epoxy resins in 3PB, 4PB, and round plates using the strain softening model revealed the effect of stress gradient on material behavior. Results indicate that direct use of tension and compression data underestimates flexural strength. By applying a flexural scaling factor (C_1) to uniaxial tension and compression strength in stress strain curves, flexural behavior of epoxy resins can be predicted accurately. However, the value of C_1 is higher for 4PB and round plate than 3PB due to the effect of stress concentration at the location of groove and the short fracture path in 3PB beam.

6.2. Future Work

The accurate prediction of strength, damage initiation and progression, and failure of complex material systems and structures under a variety of loading and environmental conditions are essential for the safe performance of polymer matrix composite structures. Therefore it is essential to obtain a fundamental understanding of the behaviors of the constituent materials. This can be achieved through an integration of analytical methods, experiments, and numerical simulations. Based on the present study, some of improvements and new concepts are suggested as follows.

1. In the present study, the mechanical behavior of epoxy resin E 863 is studied at room temperature using DIC system. In order to characterize material behavior for different applications, further investigation is required to understand the mechanical behavior of materials under different loading conditions and in different hot/wet environmental conditions.

2. In the present study, it has been shown that the direct use of tension and compression stress strain models underestimates the flexural strength of epoxy resin materials in a few structural samples. However, it is still not adequate for use in analyzing statically indeterminate structures. In order to better evaluate the degree of flexural over strength; it is required to analytically simulate the flexural behavior of epoxy resin material for indeterminate structures. For accurate analysis of indeterminate structures, a user defined subroutine (UMAT) needs to be developed for FE analysis. In addition to the analytical and numerical analysis, significant experiments on structural coupons with different shape and boundary conditions have to be conducted. The results will be implemented in the analysis of polymer matrix composites subject to out of plane loading conditions.

3. There is no standard method for determining the mechanical properties of resins under multi-axial stresses. Plasticity theories often include several assumptions for the yield behavior of solids; yielding is uninfluenced by the hydrostatic component of stress state; tensile and compressive yield strength is equal. These assumptions are not correct for epoxy resin polymers. Hydrostatic component of the stress state influences yielding, so tensile and compressive yield strengths and strains are not equal as observed in Chapter 2. Results show that the behavior of polymers is somewhat different in tension and compression. In order to develop a user defined subroutine (UMAT), an appropriate yield function and effective elastic properties need to be developed.

4. More studies at different strain rates and on different epoxy resin materials need to be done before an average flexural over-strength factor could be recommended.

5. Separation the effects of stress relaxation (i.e., viscoelasticity and viscoplasticity), plasticity, and damage on the shape of the stress-strain relationship of epoxy resin materials has been a challenge for researchers. In the present study, a methodology has been developed for epoxy resin materials to solve the nonlinear governing equations of material behavior analytically at each time step. This concept can be further developed to separate the effect of time on the material behavior.

6. In the present study, linear strain compatibility condition has been assumed. In the polymer matrix composites, epoxy resins are subject to multi-axial stress conditions. The methodology used in this study can be further developed to consider the effect of out of plan shear strains on the material behavior.

REFERENCES

Abaqus Version, 6. (2007). *Abaqus/CAE and Abaqus/Standard.* Simulia World Headquarters, Providence.

ARAMIS (2006). "User's manual for3-D image photogrammetry".

ASTM D638, (2010). Standard Test Method for Tensile Properties of Plastics.

ASTM D695, (2010). Standard Test Method for Compressive Properties of Rigid Plastics.

ASTM D790, (2003). Standard Test Method for Flexural Properties of Unreinforced and Reinforced Plastics and Electrical Insulatins Materials.

Ballatore, E. In: Carpinteri, A., editor (1999). The Damage Crack Model, Solid Mechanics and its Applications: Nonlinear Crack Models for Nonmetallic Materials. Kluwer Academic, Vol. 71, 27-76.

Bazant, Z.P., and Chen, E., (1997). Scaling of structural failure. Appl Mech., 593-627.

Behzadi, S., and Jones, F.R. (2005). Yield Behavior of Model Epoxy Matrices for Fiber Reinforced Composites: Effect of Strain Rate and Temperature. Journal of Macromolecular Science, Part B: Physics, Vol. 44, 993-1005.

Bernard, E.S., (2006). Influence of Toughness on the Apparent Cracking Load of Fiber-Reinforced Concrete Slabs. Journal of Structural Engineering, 1976-1983.

Boyce, M.C., Parks, D.M., and Argon, A.S. (1989). Plastic Flow in Oriented Glassy Polymers. International Journal of Plasticity, Vol. 5, 593-615.

Boyce, M.C., Arruda, E.M. (1990). An Experimental and Analytical Investigation of the Large Strain Compressive and Tensile Response of Glassy Polymers. Polymer Engineering and Science, Vol. 30, 1288-1298.

Boyce, M.C., Arruda, E.M., and Jayachandran, R. (1994). The Large Strain Compression, Tension, and Simple Shear of Polycarbonate. Polymer Engineering and Science, Vol. 34, 716-725.

Buckley, C.P., and Jones, D.C. (1995). Glass-rubber Constitutive Model for Amorphous Polymers Near the Glass Transition. Polymer, Vol. 36, 3301-3312.

Buckley, C.P., Harding, J. (2001). Deformation of Thermosetting Resins at Impact Rates of Strain, Part I: Experimental Study. Journal of mechanics and Physics of Solids, Vol. 49(7), 1517–1538.

Buckley, C.P., Dooling, P.J. (2004). Deformation of Thermosetting Resins at Impact Rates of Strain, Part 2: Constitutive Model with Rejuvenation. Journal of mechanics and Physics of Solids, Vol. 52(10), 2355–2377.

Chang, W.J., and Pan, J. (1997). Effects of Yield Surface Shape and Round-off Vertex on Crack-tip Fields for Pressure Sensitive Materials. Int. J. Solids Struct., Vol. 34, 3291-3320.

Chen, W., and Zhou, B. (1998). Constitutive Behavior of Epon 828/T-403 at Various Strain Rates" Mechanics of Time-Dependent Materials, Vol. 2, 103-111.

Chen, W., Lu, F., & Cheng, M. (2002). Tension and Compression Tests of Two Polymers under Quasi-static and Dynamic Loading. Polymer testing, Vol. 21, 113-121.

Chou, S.C., Robertson, K.D. (1973). The Effect of Strain Rate and Heat Developed During Deformation on the Stress-Strain Curve of Plastics. Exp. Mech., Vol. 13, 422–432.

Dupont, D., Vandewalle, L. (2004). Comparison between the round plate test and the rilem 3-point bending test. BEFIB, 101-110.

Fiedler, B., Hojo, M., Ochiai, S., Schulte, K., & Ando, M. (2001). Failure Behavior of an Epoxy Matrix under Different Kinds of Static Loading. Composite Science and Technology, Elsevier, Vol. 61, 1615-1624.

Fergusson, A.D., Puri, A., Morris, A., & Dear, J.P. (2006). Flexural Testing of Composite Sandwich Structures with Digital Speckle Photogrammetry. Journal of Applied Mechanics and Material, 135-144.

Foreman, J.P., Porter, D., Behzadi, S., Curtis, P.T., and Jones, F.R., (2010) "Predicting the thermomechanical properties of an epoxy resin blend as a function of temperature and strain rate" Compos Part A, 41, 1072-1076

Gere, J.M., (2001). Mechanics of Materials. 5th edition, Brooks, Cole, California

Giannotti, M.I., Galante, M.J., Oyanguren, P.A., and Vallo, C.I., (2003). Role of intrinsic flaws upon flexural behavior of a thermoplastic modified epoxy resin. Polym Test, 22, 429-437.

Gilat, A., Goldberg, R.K., & Roberts, G.D. (2007). Strain Rate Sensitivity of Epoxy Resin in Tensile and Shear Loading. Journal of Aerospace Engineering, ASCE, 75-89.

Goodier, JN., (1933). "Concentration of stress around spherical and cylindrical inclusions and flaws" Trans Am Soc Mech Eng, 55, 39-44.

Govaert, L.E., Timmermans, P.H.M., and Brekelmans, W.A.M. (2000). The Influence of Intrinsic Strain Softening on Strain Localization in Polycarbonate: Modeling and Experimental Validation. Journal of Engineering Material and Technology, Vol. 122, 177-185.

G'Sell, C., Souahi, A. (1997). Influence of Cross Linking on the Plastic Behavior of Amorphous Polymers at Large Strains. Journal of Engineering Material and Technology, Vol. 119, 223-227.

G'Sell, C., Hiver, J.M., and Gehin, F. (2000). "Real-time quantitative determination of volume variations in polymers under plastic strain. In: deformation, yield and fracture of polymers" The Institute of Metals, London, 371-374.

G'Sell, C., Hiver, J.M., and Dahoun, A. (2002). Experimental Characterization of Deformation Damage in Solid Polymers under Tension, and its Interrelation with Necking" International Journal of Solids and Structures, Vol. 39, 3857-3872.

Hasan, O.A., Boyce, M.C. (1995). A Constitutive Model for the Nonlinear Viscoelastic Viscoplastic Behavior of Glassy Polymers. Polymer Engineering and Science, Vol. 35, 331-344.

Hobbiebrunken, T., Fiedler, B., Hojo, M., and Tanaka, M., (2007). "Experimental determination of the true epoxy resin strength using micro-scaled specimens" Compos Part A, 38, 814-818.

Hou, J.P., Ruiz, C., & Trojanowski, A. (2000). Torsion Tests of Thermosetting Resins at Impact Strain Rate and under Quasi-static Loading. Material Science and Engineering, 181-188.

Hsu, S.Y., Vogler, T.J., and Kyriakides, S. (1999). Inelastic Behavior of an AS4/PEEK Composite under Combined Transverse Compression and Shear, II: modeling. Int. J. Plast., Vol. 15, 807-836.

Johnson, G.R., Hoegfeldt, J.M., Lindholm, U.S., and Nagy, A. (1983). Response of Various Metals to Large Torsional Strains over a Large Range of Strain Rates- Part 1: Ductile Metals. Transactions of the ASME, Journal of Engineering Materials and Technology, Vol.105, 42-47.

Jones, L.L., Wood, R.H. (1967). Yield-line analysis of Slabs, Thames and Hudson, London.

Jordan, J.L., Foley, J.R., & Siviour, C.R. (2008). Mechanical Properties of Epon 826/DEA Epoxy. Mechanic of Time-Dependent Materials, Vol. 12, 249-272.

Kozey, V., and Kumar, S. (1994). Compressive Behavior of Epoxy Resins. In: International SAMPE Technical Conference.

Kramer, E.J., (1983), "Microscopic and molecular fundamentals of crazing. In:Kausch, H.H. (Ed.), Crazing in Polymers" Adv Polym Sci, 52, 1-56

Li, F.Z., and Pan, J. (1990). Plane Stress Crack-tip Fields for Pressure Sensitive Dilatant Materials. J. Appl. Mech. Vol. 57, 40-49.

Liang, Y.M., and Liechti, K.M. (1996). On the Large Deformation and Localization Behavior of an Epoxy Resin under Multiaxial Stress State. International Journal of Solids and Structures, Vol. 33, 1479-1500.

Littell, J.D., Ruggeri, C.R., Goldberg, R.K., Roberts, G.D., Arnold, W.A., & Binienda, W.K. (2008). Measurement of Epoxy Resin Tension, Compression, and Shear Stress Strain Curves over a Wide Range of Strain Rates Using Small Test Specimens. Journal of Aerospace Engineering, ASCE, 162-173.

Lu, H., Tan, G., and Chen, W. (2001). Modeling of Constitutive Behavior for Epon 828/T-403 at High Strain Rates. Mechanics of Time-Dependent Materials, Vol. 5, 119-130.

Mannocci, F., Sherriff, M., & Watson, T.F. (2001). Three-point Bending Test of Fiber Posts. Journal of Endodontics, Vol. 27, 758-761.

Miwa, M., and Takeno, A. (1995). Strain Rate and Temperature Dependence of Shear Properties of Epoxy Resin. J. Mater. Sci. Vol. 30(7), 1760–1765.

Mulliken, A.D., and Boyce, M.C. (2006). Mechanics of the Rate-dependent Elastic-plastic Deformation of Glassy Polymers from Low to High Strain Rates. International Journal of Solids and Structures, Vol. 43, 1331–1356.

Naaman, A. E., and Reinhardt, H.W., (2006). "Proposed classification of HPFRC composites based on their tensile response." Mater Struct, 39, 547-555

Odom, E.M., and Adams, D.F., (1992). "Specimen size effect during tensile testing of an unreinforced polymer" J Mater Sci., 27, 1767-1771.

Salmon, C.G., and Johnson, J.E. (1990). Steel Structures: Design and behavior. 3rd edition, Harper and Row, New York.

Shah Khan, M.Z., Simpson, G., & Townsend, C.R. (2001). A Comparison of the Mechanical Properties in Compression of Two Resin Systems. Material Letters, Vol. 52, 173-179.

Soranakom, C., and Mobasher, B., (2007a). Closed-form Solutions for Flexural Response of Fiber-Reinforced Concrete Beams. Journal of Engineering Mechanics, ASCE, 933-941.

Soranakom, C., and Mobasher, B., (2007b), Closed-form Moment Curvature Expressions for Homogenized Fiber-Reinforced Concrete. ACI Materials Journal, 303-311

Soranakom, C., and Mobasher, B., (2008). Correlation of Tensile and Flexural Responses of Strain Softening and Strain Hardening Cement Composites. Cement & Concrete Composites.

Tervoort, T.A., Klompen, E.T.J., and Govaert, L.E. (1996). A Multi-mode Approach to Finite, Three Dimensional, Nonlinear Viscoelastic Behavior of Polymer Glasses. J. Rheol. Vol. 40, 779-797.

Tervoort, T.A., Smit, R.J.M., Brekelmans, W.A.M., and Govaert, L.E. (1998). A Constitutive Equation for the Elasto-viscoplastic Deformation of Glassy Polymers. Mechanics of Time-Dependent Materials, Vol. 1, 269-291.

Timoshenko, S.P., and Gere, J. M. (2004). Mechanical of Materials, 3rd edition, PWS-KENT publishing company.

Tschoegl N.W. (1971). Failure Surfaces in Principal Stress Space. Journal of polymer science, Part C, polymer symposia, Vol. 32, 239-267.

Vallo, C.I., (2002). "Influence of load type on flexural strength of a bone cement based on PMMA" Polym Test, 21, 793-800.

Vandewalle, L., Rickstal, F.V., Heirman, G., and Parmentier, B., (2008). On the Round Panel and 3-Point Bending Tests. Seventh Intnl. RILEM Symp. on Fiber Reinforced Concrete: Design and Applications, 173-182.

Walley, S.M., and Field, J.E. (1994). Strain Rate Sensitivity of Polymers in Compression from Low to High rates. DYMAT J. Vol. 1(3), 211–227.

Ward, I. M., and Sweeney, J. (2004). Mechanical Properties of Solid Polymers. 2nd edition, John Wiley & Sons.

Wineman, A.S., and Rajagopal, K.R. (2000). Mechanical Response of Polymers. Cambridge Univeristy Press, New York.

Yekani fard, M., Yingtao, L., and Chattopadhyay, A. (2010). Moment curvature response of polymer materials. 51st AIAA/ASME/ASCE/AHS/ASC Structures, Structural Dynamics and Materials Conference, Orlando, Florida.

Yekani fard, M., Yingtao, L., and Chattopadhyay, A. (2011a). Inverse Analysis of Constitutive Relation for Epoxy Resin Materials. 52nd AIAA/ASME/ASCE/AHS/ ASC Structures, Structural Dynamics and Materials Conference, 4-7 April, Denver, Colorado, USA.

Yekani Fard, M., Liu, Y., and Chattopadhyay, A., (2011b). "Nonlinear Flexural Behavior and Moment Curvature Response of Epoxy Resin Using Digital Image Correlation Technique," Journal of Materials Science and Engineering, 5, 212-219.

Yekani Fard, M., Liu, Y., and Chattopadhyay, A., (2011c). "Characterization of Epoxy Resin Including Strain Rate Effects Using Digital Image Correlation System," Journal of Aerospace Engineering, in press

Yekani Fard, M., Liu, Y., and Chattopadhyay, A., (2011d). "Analytical Solution for Flexural Response of Epoxy Resin Materials," Journal of Aerospace Engineering, in press

Zhang, C., and Moore, I.D. (1997). Nonlinear Mechanical Response of High Density Polyethylene II: Uniaxial Constitutive Model. Polym. Eng. Sci., Vol. 37. 414-420.

APPENDIX A

STRAIN SOFTENING MODEL IN TENSION AND COMPRESSION

Table A.1

Normalized Height of Tension Sub-zones

Cases	$\frac{h_{t1}}{h}$	$\frac{h_{t2}}{h}$	$\frac{h_{t3}}{h}$	$\frac{h_{t4}}{h}$
1,3,6,10	$(1-\kappa)$	-	-	-
2,5,8,13	$\frac{\kappa}{\lambda}$	$1-\kappa-\frac{\kappa}{\lambda}$	-	-
4,7,11,14	$\frac{\kappa}{\lambda}$	$\frac{\kappa(\mu_{t1}-1)}{\lambda}$	$1-\kappa-\frac{\kappa\mu_{t1}}{\lambda}$	-
9,12,15,16	$\frac{\kappa}{\lambda}$	$\frac{\kappa(\mu_{t1}-1)}{\lambda}$	$\frac{\kappa(\mu_{t2}-\mu_{t1})}{\lambda}$	$1-\kappa-\frac{\kappa\mu_{t2}}{\lambda}$

Table A.2

Normalized Height of Compression Sub-zones

Cases	$\frac{h_{c1}}{h}$	$\frac{h_{c2}}{h}$	$\frac{h_{c3}}{h}$	$\frac{h_{c4}}{h}$
1,2,4,9	κ	-	-	-
3,5,7,12	$\frac{\mu_{c0}\kappa}{\lambda}$	$\kappa\left(1-\frac{\mu_{c0}}{\lambda}\right)$	-	-
6,8,11,15	$\frac{\mu_{c0}\kappa}{\lambda}$	$\frac{(\mu_{c1}-\mu_{c0})\kappa}{\lambda}$	$\kappa\left(1-\frac{\mu_{c1}}{\lambda}\right)$	-
10,13,14,16	$\frac{\mu_{c0}\kappa}{\lambda}$	$\frac{(\mu_{c1}-\mu_{c0})\kappa}{\lambda}$	$\frac{(\mu_{c2}-\mu_{c1})\kappa}{\lambda}$	$\kappa\left(1-\frac{\mu_{c2}}{\lambda}\right)$

Table A.3

Normalized Stress at Vertices of Each Tension Sub-zone for Each Case

Cases	$\frac{\sigma_{t1}}{E\varepsilon_{PEL}}$	$\frac{\sigma_{t2}}{E\varepsilon_{PEL}}$	$\frac{\sigma_{t3}}{E\varepsilon_{PEL}}$	$\frac{\sigma_{t4}}{E\varepsilon_{PEL}}$
1,3,6,10	$\left(\frac{1-\kappa}{\kappa}\right)\lambda$	-	-	-
2,5,8,13	1	$1+\alpha\left(\frac{(1-\kappa)\lambda}{\kappa}-1\right)$	-	-
4,7,11,14	1	$1+\alpha(\mu_{t1}-1)$	$1+\alpha(\mu_{t1}-1)+\eta\left(\left(\frac{1-\kappa}{\kappa}\right)\lambda-\mu_{t1}\right)$	-
9,12,15,16	1	$1+\alpha(\mu_{t1}-1)$	$1+\alpha(\mu_{t1}-1)+\eta(\mu_{t2}-\mu_{t1})$	$1+\alpha(\mu_{t1}-1)+\eta(\mu_{t2}-\mu_{t1})$

Table A.4

Normalized Stress at Vertices of Each Compression Sub-zone for Each Case

Cases	$\frac{\sigma_{c1}}{E\varepsilon_{PEL}}$	$\frac{\sigma_{c2}}{E\varepsilon_{PEL}}$	$\frac{\sigma_{c3}}{E\varepsilon_{PEL}}$	$\frac{\sigma_{c4}}{E\varepsilon_{PEL}}$
1,2,4,9	$\gamma\lambda$	-	-	-
3,5,7,12	$\gamma\mu_{c0}$	$\gamma\mu_{c0}+\beta(\lambda-\mu_{c0})$	-	-
6,8,11,15	$\gamma\mu_{c0}$	$\gamma\mu_{c0}+\beta(\mu_{c1}-\mu_{c0})$	$\gamma\mu_{c0}+\beta(\mu_{c1}-\mu_{c0})+\xi(\lambda-\mu_{c1})$	-

10,13,14, 16	$\gamma\mu_{c0}$	$\gamma\mu_{c0} + \beta(\mu_{c1} - \mu_{c0})$	$\gamma\mu_{c0} + \beta(\mu_{c1} - \mu_{c0}) + \xi(\mu_{c2} - \mu_{c1})$	$\gamma\mu_{c0} + \beta(\mu_{c1} - \mu_{c0}) + \xi(\mu_{c2} - \mu_{c1})$

Table A.5

Normalized Force Component of Each Tension Sub-zone for Each Case

Cases	$\frac{F_{t1}}{bhE\varepsilon_{PEL}}$	$\frac{F_{t2}}{bhE\varepsilon_{PEL}}$	$\frac{F_{t3}}{bhE\varepsilon_{PEL}}$	$\frac{F_{t4}}{bhE\varepsilon_{PEL}}$
1,3,6,10	$\frac{\lambda\kappa}{2} - \lambda + \frac{\lambda}{2\kappa}$	-	-	-
2,5,8,13	$\frac{\kappa}{2\lambda}$	$\frac{(\lambda+1)p_1\kappa}{2\lambda} + \frac{-2\alpha\lambda^2 - 2\alpha\lambda + 2\lambda}{2\lambda} + \frac{\alpha\lambda}{2\kappa}$, $p_1 = -2 + \alpha\lambda + \alpha$		-
4,7,11,14	$\frac{\kappa}{2\lambda}$	$\frac{(2+\alpha\mu_{t1}-\alpha)(\mu_{t1}-1)\kappa}{2\lambda}$	$\frac{(-\lambda-\mu_{t1})p_2\kappa}{2\lambda} - \frac{\eta(\lambda+\mu_{t1})-p_2}{2} + \frac{\eta\lambda}{2\kappa}$, $p_2 = 2 + 2\alpha\mu_{t1} - 2\alpha - \eta\lambda - \eta\mu_{t1}$	-
9,12,15,16	$\frac{\kappa}{2\lambda}$	$\frac{(2+\alpha\mu_{t1}-\alpha)(\mu_{t1}-1)\kappa}{2\lambda}$	$\frac{(\mu_{t2}-\mu_{t1})p_3\kappa}{2\lambda}$, $p_3 = 2 + 2\alpha\mu_{t1} - 2\alpha + \eta\mu_{t2} - \eta\mu_{t1}$	$\frac{(-\lambda-\mu_{t2})p_4\kappa}{\lambda} + P_4$, $p_4 = 1 + \alpha\mu_{t1} - \alpha + \eta\mu_{t2} - \eta\mu_{t1}$

Table A.6

Normalized Force Component of Each Compression Sub-zone for Each Case

Cases	$\frac{F_{c1}}{bhE\varepsilon_{PEL}}$	$\frac{F_{c2}}{bhE\varepsilon_{PEL}}$	$\frac{F_{c3}}{bhE\varepsilon_{PEL}}$	$\frac{F_{c4}}{bhE\varepsilon_{PEL}}$
1,2,4,9	$\frac{\gamma\lambda\kappa}{2}$	-	-	-
3,5,7,12	$\frac{\gamma\mu_{c0}^2\kappa}{2\lambda}$	$\frac{p_5(\lambda-\mu_{c0})\kappa}{2\lambda}$ $p_5=2\gamma\mu_{c0}+\beta(\lambda-\mu_{c0})$	-	-
6,8,11,15	$\frac{\gamma\mu_{c0}^2\kappa}{2\lambda}$	$\frac{p_6(\mu_{c1}-\mu_{c0})\kappa}{2\lambda}$ $p_6=2\gamma\mu_{c0}+$ $\beta(\mu_{c1}-\mu_{c0})$	$\frac{p_7(\mu_{c1}-\mu_{c0})\kappa}{2\lambda}$ $p_7=2\gamma\mu_{c0}+$ $2\beta(\mu_{c1}-\mu_{c0})+$ $\xi(\lambda-\mu_{c1})$	-
10,13,14, 16	$\frac{\gamma\mu_{c0}^2\kappa}{2\lambda}$	$\frac{p_6(\mu_{c1}-\mu_{c0})\kappa}{2\lambda}$ $p_6=2\gamma\mu_{c0}+$ $\beta(\mu_{c1}-\mu_{c0})$	$\frac{p_8(\mu_{c2}-\mu_{c1})\kappa}{2\lambda}$ $p_8=2\gamma\mu_{c0}+$ $2\beta(\mu_{c1}-\mu_{c0})+$ $\xi(\mu_{c2}-\mu_{c1})$	$\frac{p_9(\lambda-\mu_{c2})\kappa}{\lambda}$ $p_9=\gamma\mu_{c0}+$ $\beta(\mu_{c1}-\mu_{c0})+$ $\xi(\mu_{c2}-\mu_{c1})$

Table A.7

Characteristic Points in the Stress Strain Development Diagram

A	$\frac{\sqrt{\gamma}-1}{\gamma-\sqrt{\gamma}}$
B	$\frac{\mu_{c0}(\beta-\gamma)+\sqrt{\mu_{c0}^2\gamma(\gamma-\beta)+\beta}}{\beta}$
C	$\sqrt{\frac{\alpha(\mu_{t1}-1)^2+2\mu_{t1}-1}{\gamma}}$
D	$\frac{1}{\xi}(\mu_{c0}(\beta-\gamma)+\mu_{c1}(\xi-\beta))$ $+\frac{1}{\xi}\sqrt{\begin{matrix}\beta^2\mu_{c0}^2-2\beta\gamma\mu_{c0}^2-2\beta^2\mu_{c0}\mu_{c1}+2\beta\xi\mu_{c0}\mu_{c1}\\+\gamma^2\mu_{c0}^2+2\gamma\beta\mu_{c0}\mu_{c1}-2\gamma\xi\mu_{c0}\mu_{c1}+\beta^2\mu_{c1}^2\\-\beta\xi\mu_{c1}^2-\beta\xi\mu_{c0}^2+\gamma\xi\mu_{c0}^2+\xi\end{matrix}}$
E	$\frac{\mu_{c0}(\beta-\gamma)+\sqrt{\gamma\mu_{c0}^2(\gamma-\beta)+\alpha\beta\mu_{t1}^2+\beta(1-\alpha)(2\mu_{t1}-1)}}{\beta}$
F	$\frac{1}{\gamma}\sqrt{-\gamma(-2\mu_{t2}+2\eta\mu_{t1}\mu_{t2}-\alpha-\eta\mu_{t1}^2+\alpha\mu_{t1}^2+2\alpha\mu_{t2}+1-\eta\mu_{t2}^2-2\alpha\mu_{t1}\mu_{t2}}$
G	$\frac{\xi\mu_{c1}^2-\beta\mu_{c1}^2+\beta\mu_{c0}^2-\gamma\mu_{c0}^2-\xi\mu_{c2}^2-1}{2(\xi\mu_{c1}-\beta\mu_{c1}+\beta\mu_{c0}-\gamma\mu_{c0}-\xi\mu_{c2})}$
H	$\frac{1}{\xi}(-\beta\mu_{c1}+\xi\mu_{c1}-\gamma\mu_{c0}+\beta\mu_{c0})$ $+\frac{1}{\xi}\sqrt{\begin{matrix}\beta(\beta-\xi)(\mu_{c1}-\mu_{c0})^2+\alpha\xi(\mu_{t1}-1)^2+2\gamma\beta\mu_{c0}\mu_{c1}-2\gamma\xi\mu_{c0}\mu_{c1}+\gamma^2\mu_{c0}^2\\-2\beta\gamma\mu_{c0}^2+\gamma\xi\mu_{c0}^2+2\xi\mu_{t1}-\xi\end{matrix}}$
I	$\frac{1}{\beta}(\beta\mu_{c0}-\gamma\mu_{c0}+\sqrt{\begin{matrix}-\beta\gamma\mu_{c0}^2+\gamma^2\mu_{c0}^2+\beta\eta\mu_{t1}^2-2\alpha\beta\mu_{t2}+\beta\eta\mu_{t2}^2-\beta\\-2\beta\eta\mu_{t1}\mu_{t2}-\alpha\beta\mu_{t1}^2+2\beta\mu_{t2}+2\alpha\beta\mu_{t1}\mu_{t2}+\alpha\beta\end{matrix}})$

J $$\sqrt{\frac{-1-\mu_{t1}^2(\alpha-\eta)-\eta\mu_{t2}^2+\alpha+2\mu_{Ut}+2\alpha\mu_{Ut}(\mu_{t1}-1)+2\eta\mu_{Ut}(\mu_{t2}-\mu_{t1})}{\gamma}}$$

K $$\frac{-\beta\mu_{c0}^2+\gamma\mu_{c0}^2-\xi\mu_{c1}^2+\beta\mu_{c1}^2+\xi\mu_{c2}^2-1+2\mu_{t1}+\alpha\mu_{t1}^2-2\alpha\mu_{t1}+\alpha}{2(-\xi\mu_{c1}+\beta\mu_{c1}-\beta\mu_{c0}+\gamma\mu_{c0}+\xi\mu_{c2})}$$

L $$\frac{1}{\xi}(\xi\mu_{c1}-\beta\mu_{c1}+\beta\mu_{c0}-\gamma\mu_{c0})+\frac{1}{\xi}\sqrt{\begin{matrix}\xi(\gamma-\beta)(\mu_{c1}-\mu_{c0})^2+\beta^2(\mu_{c1}-\mu_{c0})^2+\xi(\eta-\alpha)(\mu_{t2}-\mu_{t1})^2\\-\xi\gamma\mu_{c1}^2+2\gamma\beta\mu_{c0}(\mu_{c1}-\mu_{c0})+\alpha\xi(\mu_{t2}-1)^2+\gamma^2\mu_{c0}^2\\+\xi(2\mu_{t2}-1)\end{matrix}}$$

M $$\frac{1}{\beta}(\beta\mu_{c0}-\gamma\mu_{c0})+\frac{1}{\beta}\sqrt{\begin{matrix}\gamma\mu_{c0}^2(\gamma-\beta)-\beta(1-\alpha)+\beta\mu_{t1}^2(\eta-\alpha)+\eta\beta\mu_{t2}(2\mu_{Ut}-\mu_{t2})\\+2\beta\mu_{t1}\mu_{Ut}(\alpha-\eta)+2\beta\mu_{Ut}(1-\alpha)\end{matrix}}$$

N $$N=\frac{\begin{matrix}-1+\eta\mu_{t1}^2+\gamma\mu_{c0}^2-\beta\mu_{c0}^2-\xi\mu_{c1}^2+\alpha-\alpha\mu_{t1}^2+\xi\mu_{c2}^2+\beta\mu_{c1}^2-2\eta\mu_{t1}\mu_{t2}+\eta\mu_{t2}^2\\+2\alpha\mu_{t1}\mu_{t2}-2\alpha\mu_{t2}+2\mu_{t2}\end{matrix}}{2(-\xi\mu_{c1}+\beta\mu_{c1}-\beta\mu_{c0}+\gamma\mu_{c0}+\xi\mu_{c2})}$$

O $$\frac{1}{\xi}(-\gamma\mu_{c0}+\beta\mu_{c0}+\xi\mu_{c1}-\beta\mu_{c1})+\frac{1}{\xi}\sqrt{\begin{matrix}\mu_{c0}^2(\gamma-\beta)^2-\xi\beta(\mu_{c1}-\mu_{c0})^2+\xi\eta(\mu_{Ut}-\mu_{t1})^2\\-\xi\eta(\mu_{Ut}-\mu_{t2})^2+2\beta\mu_{c0}\mu_{c1}(\gamma-\beta)\\+\xi\gamma\mu_{c0}(\mu_{c0}-2\mu_{c1})+(1-\alpha)\xi(2\mu_{t3}-1)\\+\alpha\xi\mu_{t1}(2\mu_{Ut}-\mu_{t1})+\beta^2\mu_{c1}^2\end{matrix}}$$

P $$\frac{\begin{matrix}(\gamma-\beta)\mu_{c0}^2+(\beta-\xi)\mu_{c1}^2+\xi\mu_{c2}^2+(\eta-\alpha)\mu_{t1}^2-\eta\mu_{t2}^2+\alpha-1+2\mu_{Ut}+2\alpha\mu_{Ut}(\mu_{t1}-1)\\+2\eta\mu_{Ut}(\mu_{t2}-\mu_{t1})\end{matrix}}{2\mu_{c0}(\gamma-\beta)+2\mu_{c1}(\beta-\xi)+2\mu_{c2}\xi}$$

Table A.8

Neutral Axis Depth Ratio for Each Case

Case	κ_i
1	$\dfrac{-1+\sqrt{\gamma}}{\gamma-1}$
2	$\dfrac{-\lambda\left(\alpha(\lambda+1)-1-\sqrt{-\alpha+1+\alpha\gamma\lambda^2}\right)}{-\left(\alpha(\lambda+1)^2-2\lambda-1\right)+\gamma\lambda^2}$
3	$\dfrac{\lambda\left(\lambda-\sqrt{(\lambda-\mu_{c0})^2(\beta-\gamma)+\gamma\lambda^2}\right)}{\lambda^2-(\lambda-\mu_{c0})^2(\beta-\gamma)-\gamma\lambda^2}$
4	$\dfrac{\lambda\left(-\eta(\lambda+\mu_{t1})+1+\alpha(\mu_{t1}-1)+\sqrt{1+\alpha^2(\mu_{t1}-1)^2-\eta\alpha(\mu_{t1}-1)^2+2\alpha(\mu_{t1}-1)+\eta\gamma\lambda^2-2\eta\mu_{t1}+\eta}\right)}{\alpha(\mu_{t1}^2-1)+2\lambda+2\alpha\lambda(\mu_{t1}-1)-\eta(\lambda+\mu_{t1})^2+1+\gamma\lambda^2}$
5	$\dfrac{\lambda\left(\alpha(\lambda+1)-1-\sqrt{-\alpha+1+\alpha\left((\lambda-\mu_{c0})^2(\beta-\gamma)+\gamma\lambda^2\right)}\right)}{\alpha(\lambda+1)^2-2\lambda-1-(\lambda-\mu_{c0})^2(\beta-\gamma)-\gamma\lambda^2}$
6	$\dfrac{\lambda\left(-\lambda+\sqrt{\gamma\lambda^2-\gamma(\lambda-\mu_{c0})^2-\beta(\lambda-\mu_{c1})^2+\beta(\lambda-\mu_{c0})^2+\xi(\lambda-\mu_{c1})^2}\right)}{-\lambda^2+\gamma\lambda^2-\gamma(\lambda-\mu_{c0})^2-\beta(\lambda-\mu_{c1})^2+\beta(\lambda-\mu_{c0})^2+\xi(\lambda-\mu_{c1})^2}$
7	$\dfrac{\lambda\left(1+\alpha\mu_{t1}-\alpha-\eta\lambda-\eta\mu_{t1}+\sqrt{1-2\alpha+\eta+2\mu_{t1}(\alpha-\eta)+\eta\gamma\lambda^2+\eta(\lambda-\mu_{c0})(\beta-\gamma)+\alpha(\alpha-\eta)(\mu_{t1}-1)^2}\right)}{(\lambda+\mu_{t1})^2(\alpha-\eta)+(\beta-\gamma)(\lambda-\mu_{c0})^2-\alpha(\lambda+1)^2+\gamma\lambda^2+2\lambda+1}$

8

$$\frac{\lambda\left(\alpha(\lambda+1)-1-\sqrt{\alpha(\beta-\gamma)(\lambda-\mu_{c0})^2+\alpha(\xi-\beta)(\lambda-\mu_{c1})^2+\alpha\gamma\lambda^2-\alpha+1}\right)}{(\lambda-\mu_{c0})^2(\gamma-\beta)+(\beta-\xi)(\lambda-\mu_{c1})^2-\gamma\lambda^2+\alpha(\lambda+1)^2-2\lambda-1}$$

9

$$\frac{2\lambda(1+\alpha(\mu_{t1}-1)+\eta(\mu_{t2}-\mu_{t1}))}{1+2\lambda+\gamma\lambda^2+(\lambda+\mu_{t1})^2(\alpha-\eta)+\eta(\lambda+\mu_{t2})^2-\alpha(\lambda+1)^2}$$

10

$$\frac{\lambda\left(\lambda-\sqrt{(\lambda-\mu_{c1})^2(-\beta+\xi)+(-\gamma+\beta)(\lambda-\mu_{c0})^2+\gamma\lambda^2-\xi(\lambda-\mu_{c2})^2}\right)}{(\lambda-\mu_{c1})^2(\beta-\xi)+(\gamma-\beta)(\lambda-\mu_{c0})^2+\lambda^2(1-\gamma)+\xi(\lambda-\mu_{c2})^2}$$

11

$$\frac{\lambda(-\eta\lambda-\eta\mu_{t1}+1+\alpha\mu_{t1}-\alpha)}{-\alpha(\lambda+1)^2+(\alpha-\eta)(\lambda+\mu_{t1})^2+(\xi-\beta)(\lambda-\mu_{c1})^2+(\beta-\gamma)(\lambda-\mu_{c0})^2+\gamma\lambda^2+2\lambda+1}$$
$$+\frac{\lambda\sqrt{\eta(\lambda-\mu_{c0})^2(\beta-\gamma)+\eta(\lambda-\mu_{c1})^2(\xi-\beta)+\alpha(\mu_{t1}-1)^2(\alpha-\eta)+\eta\gamma\lambda^2+2\alpha\mu_{t1}-2\eta\mu_{t1}+\eta-2\alpha+1}}{-\alpha(\lambda+1)^2+(\alpha-\eta)(\lambda+\mu_{t1})^2+(\xi-\beta)(\lambda-\mu_{c1})^2+(\beta-\gamma)(\lambda-\mu_{c0})^2+\gamma\lambda^2+2\lambda+1}$$

12

$$\frac{2\lambda(1+\alpha(\mu_{t1}-1)+\eta(\mu_{t2}-\mu_{t1}))}{\alpha(\lambda+\mu_{t1})^2-\alpha(\lambda+1)^2+(\beta-\gamma)(\lambda-\mu_{c0})^2+2\eta\lambda(\mu_{t2}-\mu_{t1})+\eta(\mu_{t2}^2-\mu_{t1}^2)+\gamma\lambda^2+2\lambda+1}$$

13

$$\frac{\lambda\left(\alpha\lambda+\alpha-1-\sqrt{\alpha(\lambda-\mu_{c0})^2(\beta-\gamma)+\alpha(\lambda-\mu_{c1})^2(\xi-\beta)-\alpha\xi(\lambda-\mu_{c2})^2+\alpha\gamma\lambda^2-\alpha+1}\right)}{(\lambda-\mu_{c0})^2(\gamma-\beta)+(\lambda-\mu_{c1})^2(\beta-\xi)+\xi(\lambda-\mu_{c2})^2+\alpha(\lambda+1)^2-\gamma\lambda^2-2\lambda-1}$$

14

$$\frac{-\lambda(\eta\lambda+\eta\mu_{t1}+\alpha-\alpha\mu_{t1}-1)}{(\lambda-\mu_{c0})^2(\beta-\gamma)+(\lambda-\mu_{c1})^2(\xi-\beta)-\xi(\lambda-\mu_{c2})^2+(\lambda+\mu_{t2})^2(\alpha-\eta)-\alpha(\lambda+1)^2+\gamma\lambda^2+2\lambda+1}$$
$$+\frac{\lambda\sqrt{\eta(\lambda-\mu_{c0})^2(\beta-\gamma)+\eta(\lambda-\mu_{c1})^2(\xi-\beta)-\eta\xi(\lambda-\mu_{c2})^2+\alpha(\mu_{t1}-1)^2(\alpha-\eta)+2\alpha(\mu_{t1}-1)+\eta\gamma\lambda^2-2\eta\mu_{t1}+\eta+1}}{(\lambda-\mu_{c0})^2(\beta-\gamma)+(\lambda-\mu_{c1})^2(\xi-\beta)-\xi(\lambda-\mu_{c2})^2+(\lambda+\mu_{t2})^2(\alpha-\eta)-\alpha(\lambda+1)^2+\gamma\lambda^2+2\lambda+1}$$

15

$$\frac{2\lambda(1+\alpha(\mu_{t1}-1)+\eta(\mu_{t2}-\mu_{t1}))}{(\lambda-\mu_{c0})^2(\beta-\gamma)+(\xi-\beta)(\lambda-\mu_{c1})^2+(\lambda+\mu_{t1})^2(\alpha-\eta)+\eta(\lambda+\mu_{t2})^2-\alpha(\lambda+1)^2+\gamma\lambda^2+2\lambda+1}$$

16

$$\frac{-2\lambda(1+\alpha(\mu_{t1}-1)+\eta(\mu_{t2}-\mu_{t1}))}{(\lambda-\mu_{c0})^2(\gamma-\beta)+(\lambda-\mu_{c1})^2(\beta-\xi)+\xi(\lambda-\mu_{c2})^2+(\lambda+\mu_{t1})^2(\eta-\alpha)-\eta(\lambda+\mu_{t2})^2+\alpha(\lambda+1)^2-\gamma\lambda^2-2\lambda-1}$$

Table A.9

Normalized Moment for Each Case

Case	M'_i
1	$2\lambda(\gamma-1)\kappa_1^{\,2}+6\lambda\kappa_1-6\lambda+\frac{2\lambda}{\kappa_1}$
2	$\frac{\left((1-\alpha)\left(3\lambda^2-1\right)-2\lambda^3(\alpha-\gamma)\right)\kappa_2^2}{\lambda^2}+6\left(\alpha(\lambda+1)-1\right)\kappa_2+3\left(1-\alpha(1+2\lambda)\right)+\frac{2\alpha\lambda}{\kappa_2}$
3	$\frac{(-\gamma\mu_{c0}^3-3\mu_{c0}\beta\lambda^2+3\gamma\mu_{c0}\lambda^2+2\beta\lambda^3+\beta\mu_{c0}^3-2\lambda^3)\kappa_3^{\,2}}{\lambda^2}+6\lambda\kappa_3-6\lambda+\frac{2\lambda}{\kappa_3}$
4	$\frac{(3\lambda^2\alpha\mu_{t1}+\mu_{t1}^3\eta-1-3\mu_{t1}\eta\lambda^2+2\gamma\lambda^3+\alpha-3\alpha\lambda^2-2\eta\lambda^3+3\lambda^2-\alpha\mu_{t1}^3)\kappa_4^{\,2}}{\lambda^2}+$ $(6\alpha+6\eta\lambda+6\mu_{t1}\eta-6-6\alpha\mu_{t1})\kappa_4+-3\mu_{t1}\eta+3-6\eta\lambda+3\alpha\mu_{t1}-3\alpha+\frac{2\eta\lambda}{\kappa_4}$
5	$\frac{(-\gamma\mu_{c0}^3-3\mu_{c0}\beta\lambda^2+3\gamma\mu_{c0}\lambda^2+2\beta\lambda^3+\beta\mu_{c0}^3-1-2\alpha\lambda^3+\alpha+3\lambda^2-3\alpha\lambda^2)\kappa_5^{\,2}}{\lambda^2}$ $+(-6+6\alpha\lambda+6\alpha)\kappa_5-3\alpha-6\alpha\lambda+3+\frac{2\alpha\lambda}{\kappa_5}$
6	$\frac{(-\gamma\mu_{c0}^3+3\gamma\mu_{c0}\lambda^2-\beta\mu_{c1}^3+\beta\mu_{c0}^3-3\mu_{c1}\xi\lambda^2+\xi\mu_{c1}^3+3\beta\mu_{c1}\lambda^2-3\beta\mu_{c0}\lambda^2+2\xi\lambda^3-2\lambda^3)\kappa_6^{\,2}}{\lambda^2}$ $+6\lambda\kappa_6-6\lambda+\frac{2\lambda}{\kappa_6}$
7	$\frac{(\alpha+3\lambda^2+3\lambda^2\alpha\mu_{t1}+2\beta\lambda^3-\gamma\mu_{c0}^3+\beta\mu_{c0}^3-3\mu_{c0}\beta\lambda^2-\alpha\mu_{t1}^3+\mu_{t1}^3\eta-3\alpha\lambda^2-2\lambda^3\eta-1+3\gamma\mu_{c0}\lambda^2-3\mu_{t1}\eta\lambda^2)\kappa_7^{\,2}}{\lambda^2}$ $+(6\lambda\eta+6\mu_{t1}\eta-6-6\alpha\mu_{t1}+6\alpha)\kappa_7+3\alpha\mu_{t1}-6\lambda\eta+3-3\mu_{t1}\eta-3\alpha+\frac{2\eta\lambda}{\kappa_7}$

8	$-\frac{(1-3\gamma\mu_{c0}\lambda^2-3\beta\mu_{c1}\lambda^2+3\mu_{c1}\xi\lambda^2+\beta\mu_{c1}^3-\beta\mu_{c0}^3+3\beta\mu_{c0}\lambda^2+\gamma\mu_{c0}^3-\xi\mu_{c1}^3+3\alpha\lambda^2-\alpha-2\xi\lambda^3+2\alpha\lambda^3-3\lambda^2)\kappa_8^{\,2}}{\lambda^2}$ $-(6-6\alpha\lambda-6\alpha)\kappa_8-(3\alpha-3+6\alpha\lambda)+\frac{2\alpha\lambda}{\kappa_8}$
9	$\frac{(3\lambda^2\alpha\mu_{t1}+3\eta\mu_{t2}\lambda^2-3\mu_{t1}\eta\lambda^2+\alpha-\alpha\mu_{t1}^3+\mu_{t1}^3\eta-\eta\mu_{t2}^3-3\alpha\lambda^2-1+2\gamma\lambda^3+3\lambda^2)\kappa_9^{\,2}}{\lambda^2}$ $+(-6\eta\mu_{t2}-6-6\alpha\mu_{t1}+6\alpha+6\mu_{t1}\eta)\kappa_9+3\alpha\mu_{t1}-3\mu_{t1}\eta+3+3\eta\mu_{t2}-3\alpha$
10	$-\frac{(\beta\mu_{c1}^3-\xi\mu_{c1}^3-\beta\mu_{c0}^3+\gamma\mu_{c0}^3+\xi\mu_{c2}^3+2\lambda^3-3\gamma\mu_{c0}\lambda^2-3\beta\mu_{c1}\lambda^2+3\beta\mu_{c0}\lambda^2-3\xi\mu_{c2}\lambda^2+3\xi\mu_{c1}\lambda^2)\kappa_{10}^{\,2}}{\lambda^2}+6\lambda\kappa_{1(}$ $-6\lambda+\frac{2\lambda}{\kappa_{10}}$
11	$-\frac{1}{\lambda^2}(-\alpha+1-3\lambda^2-2\xi\lambda^3+2\eta\lambda^3-3\gamma\mu_{c0}\lambda^2-\beta\mu_{c0}^3+3\xi\mu_{c1}\lambda^2-\mu_{t1}^3\eta+3\mu_{t1}\eta\lambda^2+3\beta\mu_{c0}\lambda^2+3\alpha\lambda^2-3\alpha\mu_{t1}\lambda^2$ $-3\beta\mu_{c1}\lambda^2+\beta\mu_{c1}^3+\gamma\mu_{c0}^3-\xi\mu_{c1}^3+\alpha\mu_{t1}^3)\kappa_{11}^{\,2}-(-6\eta\lambda+6+6\alpha\mu_{t1}-6\mu_{t1}\eta-6\alpha)\kappa_{11}$ $+3\alpha\mu_{t1}-6\eta\lambda-3\alpha+3-3\mu_{t1}\eta+\frac{2\eta\lambda}{\kappa_{11}}$
12	$\frac{1}{\lambda^2}(3\gamma\mu_{c0}\lambda^2-3\mu_{t1}\eta\lambda^2+2\beta\lambda^3+\alpha-\alpha\mu_{t1}^3-\gamma\mu_{c0}^3-\eta\mu_{t2}^3+\beta\mu_{c0}^3-3\beta\mu_{c0}\lambda^2+\mu_{t1}^3\eta+3\lambda^2-1+3\alpha\mu_{t1}\lambda^2$ $-3\alpha\lambda^2+3\eta\mu_{t2}\lambda^2)\kappa_{12}^{\,2}+(6\alpha+6\mu_{t1}\eta-6-6\alpha\mu_{t1}-6\eta\mu_{t2})\kappa_{12}-3\mu_{t1}\eta+3\alpha\mu_{t1}-3\alpha+3+3\eta\mu_{t2}$
13	$\frac{1}{\lambda^2}(\beta\mu_{c0}^3+\xi\mu_{c1}^3-\beta\mu_{c1}^3+\alpha+3\lambda^2-3\alpha\lambda^2-\gamma\mu_{c0}^3-1-\xi\mu_{c2}^3+3\gamma\mu_{c0}\lambda^2+3\beta\mu_{c1}\lambda^2-3\beta\mu_{c0}\lambda^2+3\xi\mu_{c2}\lambda^2$ $-3\xi\mu_{c1}\lambda^2-2\alpha\lambda^3)\kappa_{13}^{\,2}+(-6+6\alpha\lambda+6\alpha)\kappa_{13}+3-3\alpha-6\alpha\lambda+\frac{2\alpha\lambda}{\kappa_{13}}$
14	$\frac{1}{\lambda^2}(3\xi\mu_{c2}\lambda^2-3\xi\mu_{c1}\lambda^2-3\mu_{t1}\eta\lambda^2-\gamma\mu_{c0}^3+3\beta\mu_{c1}\lambda^2+\alpha+\beta\mu_{c0}^3+3\gamma\mu_{c0}\lambda^2+3\alpha\mu_{t1}\lambda^2-3\beta\mu_{c0}\lambda^2-3\alpha\lambda^2$ $+\mu_{t1}^3\eta+3\lambda^2-2\eta\lambda^3-\xi\mu_{c2}^3+\xi\mu_{c1}^3-\alpha\mu_{t1}^3-1-\beta\mu_{c1}^3)\kappa_{14}^{\,2}+(-6+6\alpha-6\alpha\mu_{t1}+6\mu_{t1}\eta+6\eta\lambda)\kappa_{14}$ $-3\mu_{t1}\eta+3+3\alpha\mu_{t1}-6\eta\lambda-3\alpha+\frac{2\eta\lambda}{\kappa_{14}}$

15	$-\frac{1}{\lambda^2}(1+\beta\mu_{c1}^3-\beta\mu_{c0}^3-3\alpha\mu_{t1}\lambda^2+\gamma\mu_{c0}^3+3\alpha\lambda^2-2\xi\lambda^3+\alpha\mu_{t1}^3-\eta\mu_{t1}^3+\eta\mu_{t2}^3+3\mu_{c1}\xi\lambda^2-3\gamma\mu_{c0}\lambda^2-3\beta\mu_{c1}\lambda^2$ $+3\beta\mu_{c0}\lambda^2-3\eta\mu_{t2}\lambda^2-\alpha+3\eta\mu_{t1}\lambda^2-3\lambda^2-\xi\mu_{c1}^3)\kappa_{15}{}^2-(-6\alpha+6+6\eta\mu_{t2}+6\alpha\mu_{t1}-6\eta\mu_{t1})\kappa_{15}$ $+3\alpha\mu_{t1}-3\alpha+3\eta\mu_{t2}-3\eta\mu_{t1}+3$
16	$-\frac{1}{\lambda^2}(1+\xi\mu_{c2}^3-3\eta\mu_{t2}\lambda^2+\alpha\mu_{t1}^3+3\eta\mu_{t1}\lambda^2+3\beta\mu_{c0}\lambda^2-3\lambda^2+3\mu_{c1}\xi\lambda^2-3\beta\mu_{c1}\lambda^2-\eta\mu_{t1}^3-3\xi\mu_{c2}\lambda^2-\xi\mu_{c1}^3$ $+3\alpha\lambda^2-\alpha+\eta\mu_{t2}^3-3\alpha\mu_{t1}\lambda^2-3\gamma\mu_{c0}\lambda^2+\beta\mu_{c1}^3-\beta\mu_{c0}^3+\gamma\mu_{c0}^3)\kappa_{16}{}^2-(-6\alpha+6+6\eta\mu_{t2}+6\alpha\mu_{t1}-6\eta\mu_{t1})\kappa_{16}$ $+3\alpha\mu_{t1}-3\alpha+3\eta\mu_{t2}-3\eta\mu_{t1}+3$

APPENDIX B

SIMPLIFIED TENSION AND COMPRESSION MODEL WITH CONSTANT FLOW STRESS IN TENSION AND CONSTANT YIELD IN COMPRESSION

Table B.1

Normalized Height for Each Sub-zone

Case	$\frac{h_{c3}}{h}$	$\frac{h_{c2}}{h}$	$\frac{h_{c1}}{h}$	$\frac{h_{t1}}{h}$	$\frac{h_{t2}}{h}$	$\frac{h_{t3}}{h}$
1	-	-	κ	$(1-\kappa)$	-	-
2	-	-	κ	$\frac{\kappa}{\lambda}$	$1-\kappa-\frac{\kappa}{\lambda}$	-
3	-	$\kappa\left(1-\frac{\mu_{c0}}{\lambda}\right)$	$\frac{\mu_{c0}\kappa}{\lambda}$	$(1-\kappa)$	-	-
4	-	-	κ	$\frac{\kappa}{\lambda}$	$\frac{\kappa}{\lambda}(\mu_{t1}-1)$	$1-\kappa-\frac{\mu_{t1}\kappa}{\lambda}$
5	-	$\kappa\left(1-\frac{\mu_{c0}}{\lambda}\right)$	$\frac{\mu_{c0}\kappa}{\lambda}$	$\frac{\kappa}{\lambda}$	$1-\kappa-\frac{\kappa}{\lambda}$	-
6	$\kappa\left(1-\frac{\mu_{c1}}{\lambda}\right)$	$\frac{\kappa}{\lambda}(\mu_{c1}-\mu_{c0})$	$\frac{\mu_{c0}\kappa}{\lambda}$	$(1-\kappa)$	-	-
7	-	$\kappa\left(1-\frac{\mu_{c0}}{\lambda}\right)$	$\frac{\mu_{c0}\kappa}{\lambda}$	$\frac{\kappa}{\lambda}$	$\frac{\kappa}{\lambda}(\mu_{t1}-1)$	$1-\kappa-\frac{\mu_{t1}\kappa}{\lambda}$
8	$\kappa\left(1-\frac{\mu_{c1}}{\lambda}\right)$	$\frac{\kappa}{\lambda}(\mu_{c1}-\mu_{c0})$	$\frac{\mu_{c0}\kappa}{\lambda}$	$\frac{\kappa}{\lambda}$	$1-\kappa-\frac{\kappa}{\lambda}$	-
9	$\kappa\left(1-\frac{\mu_{c1}}{\lambda}\right)$	$\frac{\kappa}{\lambda}(\mu_{c1}-\mu_{c0})$	$\frac{\mu_{c0}\kappa}{\lambda}$	$\frac{\kappa}{\lambda}$	$\frac{\kappa}{\lambda}(\mu_{t1}-1)$	$1-\kappa-\frac{\mu_{t1}\kappa}{\lambda}$

Table B.2

Normalized Stresses at the Vertices of Tension Sub-zones

Case	$\frac{\sigma_{t1}}{E\varepsilon_{PEL}}$	$\frac{\sigma_{t2}}{E\varepsilon_{PEL}}$	$\frac{\sigma_{t3}}{E\varepsilon_{PEL}}$
1	$\left(\frac{1-\kappa}{\kappa}\right)\lambda$	-	-
2	1	$1+\alpha\left(\frac{(1-\kappa)\lambda}{\kappa}-1\right)$	-

3	$\left(\frac{1-\kappa}{\kappa}\right)\lambda$	-	-
4	1	$1+\alpha(\mu_{t1}-1)$	ω
5	1	$1+\alpha\left(\frac{(1-\kappa)\lambda}{\kappa}-1\right)$	-
6	$\left(\frac{1-\kappa}{\kappa}\right)\lambda$	-	-
7	1	$1+\alpha(\mu_{t1}-1)$	ω
8	1	$1+\alpha\left(\frac{(1-\kappa)\lambda}{\kappa}-1\right)$	-
9	1	$1+\alpha(\mu_{t1}-1)$	ω

Table B.3

Normalized Stresses at the Vertices of Compression Sub-zones

Case	$\frac{\sigma_{c3}}{E\varepsilon_{PEL}}$	$\frac{\sigma_{c2}}{E\varepsilon_{PEL}}$	$\frac{\sigma_{c1}}{E\varepsilon_{PEL}}$
1	-	-	$\gamma\lambda$
2	-	-	$\gamma\lambda$
3	-	$\gamma\mu_{c0}+\beta(\lambda-\mu_{c0})$	$\gamma\mu_{c0}$
4	-	-	$\gamma\lambda$
5	-	$\gamma\mu_{c0}+\beta(\lambda-\mu_{c0})$	$\gamma\mu_{c0}$
6	$\gamma\mu_{c0}+\beta(\mu_{c1}-\mu_{c0})$	$\gamma\mu_{c0}+\beta(\mu_{c1}-\mu_{c0})$	$\gamma\mu_{c0}$
7	-	$\gamma\mu_{c0}+\beta(\lambda-\mu_{c0})$	$\gamma\mu_{c0}$
8	$\gamma\mu_{c0}+\beta(\mu_{c1}-\mu_{c0})$	$\gamma\mu_{c0}+\beta(\mu_{c1}-\mu_{c0})$	$\gamma\mu_{c0}$
9	$\gamma\mu_{c0}+\beta(\mu_{c1}-\mu_{c0})$	$\gamma\mu_{c0}+\beta(\mu_{c1}-\mu_{c0})$	$\gamma\mu_{c0}$

Table B.4

Normalized Tension Forces for Simplified Model

Case	$\frac{F_{t1}}{bhE\varepsilon_{PEL}}$	$\frac{F_{t2}}{bhE\varepsilon_{PEL}}$	$\frac{F_{t3}}{bhE\varepsilon_{PEL}}$
1	$\frac{\lambda\kappa}{2}-\lambda+\frac{\lambda}{2\kappa}$	-	-
2	$\frac{\kappa}{2\lambda}$	$\frac{(\lambda+1)p\kappa}{2\lambda}+\frac{-2\alpha\lambda^2-2\alpha\lambda+2\lambda}{2\lambda}+\frac{\alpha\lambda}{2\kappa},\ p=-2+\alpha\lambda+\alpha$	-
3	$\frac{\lambda\kappa}{2}-\lambda+\frac{\lambda}{2\kappa}$	-	-
4	$\frac{\kappa}{2\lambda}$	$\frac{(2+\alpha\mu_{t1}-\alpha)(\mu_{t1}-1)\kappa}{2\lambda}$	$\frac{-\omega(\lambda+\mu_{t1})\kappa}{\lambda}+\omega$
5	$\frac{\kappa}{2\lambda}$	$\frac{(\lambda+1)p\kappa}{2\lambda}+\frac{-2\alpha\lambda^2-2\alpha\lambda+2\lambda}{2\lambda}+\frac{\alpha\lambda}{2\kappa}$	-
6	$\frac{\lambda\kappa}{2}-\lambda+\frac{\lambda}{2\kappa}$	-	-
7	$\frac{\kappa}{2\lambda}$	$\frac{(2+\alpha\mu_{t1}-\alpha)(\mu_{t1}-1)\kappa}{2\lambda}$	$\frac{-\omega(\lambda+\mu_{t1})\kappa}{\lambda}+\omega$
8	$\frac{\kappa}{2\lambda}$	$\frac{(\lambda+1)p\kappa}{2\lambda}+\frac{-2\alpha\lambda^2-2\alpha\lambda+2\lambda}{2\lambda}+\frac{\alpha\lambda}{2\kappa}$	-
9	$\frac{\kappa}{2\lambda}$	$\frac{(2+\alpha\mu_{t1}-\alpha)(\mu_{t1}-1)\kappa}{2\lambda}$	$\frac{-\omega(\lambda+\mu_{t1})\kappa}{\lambda}+\omega$

Table B.5

Normalized Compression Forces for Simplified Model

Case	$\frac{F_{c3}}{bhE\varepsilon_{PEL}}$	$\frac{F_{c2}}{bhE\varepsilon_{PEL}}$	$\frac{F_{c1}}{bhE\varepsilon_{PEL}}$
1	-	-	$\frac{\gamma\lambda\kappa}{2}$
2	-	-	$\frac{\gamma\lambda\kappa}{2}$
3	-	$\frac{q(\lambda-\mu_{c0})\kappa}{2\lambda}$ $q=2\gamma\mu_{c0}+\beta(\lambda-\mu_{c0})$	$\frac{\gamma\mu_{c0}^2\kappa}{2\lambda}$
4	-	-	$\frac{\gamma\lambda\kappa}{2}$
5	-	$\frac{q(\lambda-\mu_{c0})\kappa}{2\lambda}$	$\frac{\gamma\mu_{c0}^2\kappa}{2\lambda}$
6	$\frac{s(\lambda-\mu_{c1})\kappa}{\lambda}$ $s=\gamma\mu_{c0}+\beta(\mu_{c1}-\mu_{c0})$	$\frac{r(\mu_{c1}-\mu_{c0})\kappa}{2\lambda}$ $r=2\gamma\mu_{c0}+\beta(\mu_{c1}-\mu_{c0})$	$\frac{\gamma\mu_{c0}^2\kappa}{2\lambda}$
7	-	$\frac{q(\lambda-\mu_{c0})\kappa}{2\lambda}$	$\frac{\gamma\mu_{c0}^2\kappa}{2\lambda}$
8	$\frac{s(\lambda-\mu_{c1})\kappa}{\lambda}$	$\frac{r(\mu_{c1}-\mu_{c0})\kappa}{2\lambda}$	$\frac{\gamma\mu_{c0}^2\kappa}{2\lambda}$
9	$\frac{s(\lambda-\mu_{c1})\kappa}{\lambda}$	$\frac{r(\mu_{c1}-\mu_{c0})\kappa}{2\lambda}$	$\frac{\gamma\mu_{c0}^2\kappa}{2\lambda}$

Table B.6

Normalized Arm Moment for Tension Forces

Case	$\frac{Z_{t1}}{h}$	$\frac{Z_{t2}}{h}$	$\frac{Z_{t3}}{h}$
1	$\frac{2}{3}(1-\kappa)$	-	-
2	$\frac{2\kappa}{3\lambda}$	$\frac{y_1\kappa^2+y_2\kappa-2\alpha\lambda^2}{3\lambda(p\kappa-\alpha\lambda)}, y_1=3\lambda-3-\alpha\lambda$ $+\alpha-2\alpha\lambda^2, y_2=4\alpha\lambda^2+\lambda(\alpha-3)$	-
3	$\frac{2}{3}(1-\kappa)$	-	-
4	$\frac{2\kappa}{3\lambda}$	$\frac{y_4\kappa}{3y_5\lambda}, y_4=3\mu_{t1}+3+2\alpha\mu_{t1}^2-\alpha\mu_{t1}$ $-\alpha,\ y_5=2+\alpha(\mu_{t1}-1)$	$\frac{1}{2}\left(1-\frac{(\lambda-\mu_{t1})\kappa}{\lambda}\right)$
5	$\frac{2\kappa}{3\lambda}$	$\frac{y_1\kappa^2+y_2\kappa-2\alpha\lambda^2}{3\lambda(p\kappa-\alpha\lambda)}$	-
6	$\frac{2}{3}(1-\kappa)$	-	-
7	$\frac{2\kappa}{3\lambda}$	$\frac{y_4\kappa}{3y_5\lambda}$	$\frac{1}{2}\left(1-\frac{(\lambda-\mu_{t1})\kappa}{\lambda}\right)$
8	$\frac{2\kappa}{3\lambda}$	$\frac{y_1\kappa^2+y_2\kappa-2\alpha\lambda^2}{3\lambda(p\kappa-\alpha\lambda)}$	-
9	$\frac{2\kappa}{3\lambda}$	$\frac{y_4\kappa}{3y_5\lambda}$	$\frac{1}{2}\left(1-\frac{(\lambda-\mu_{t1})\kappa}{\lambda}\right)$

Table B.7

Normalized Arm Moment for Compression Forces

Case	$\frac{Z_{c3}}{h}$	$\frac{Z_{c2}}{h}$	$\frac{Z_{c1}}{h}$
1	-	-	$\frac{2\kappa}{3}$
2	-	-	$\frac{2\kappa}{3}$
3	-	$\frac{y_3\kappa}{3q\lambda},\ y_3 = 3\gamma\mu_{c0}^2 - \mu_{c0}\beta\lambda - \beta\mu_{c0}^2 + 3\gamma\mu_{c0}\lambda + 2\beta\lambda^2$	$\frac{2\mu_{c0}\kappa}{3\lambda}$
4	-	-	$\frac{2\kappa}{3}$
5	-	$\frac{y_3\kappa}{3q\lambda}$	$\frac{2\mu_{c0}\kappa}{3\lambda}$
6	$\frac{(\lambda+\mu_{c1})\kappa}{2\lambda}$	$\frac{y_6\kappa}{3r\lambda}, y_6 = 3\gamma\mu_{c0}^2 - \mu_{c0}\beta\mu_{c1} - \beta\mu_{c0}^2 + 3\gamma\mu_{c0}\mu_{c1} + 2\beta\mu_{c1}^2$	$\frac{2\mu_{c0}\kappa}{3\lambda}$
7	-	$\frac{y_3\kappa}{3q\lambda}$	$\frac{2\mu_{c0}\kappa}{3\lambda}$
8	$\frac{(\lambda+\mu_{c1})\kappa}{2\lambda}$	$\frac{y_6\kappa}{3r\lambda}$	$\frac{2\mu_{c0}\kappa}{3\lambda}$
9	$\frac{(\lambda+\mu_{c1})\kappa}{2\lambda}$	$\frac{y_6\kappa}{3r\lambda}$	$\frac{2\mu_{c0}\kappa}{3\lambda}$

Table B.8

Expressions for Characteristic Points Based on the Simplified Model

A	$\frac{\sqrt{\gamma}-1}{\gamma-\sqrt{\gamma}}$
B	$\frac{\mu_{c0}(\beta-\gamma)+\sqrt{\mu_{c0}^2\gamma(\gamma-\beta)+\beta}}{\beta}$
C	$\sqrt{\frac{\alpha(\mu_{t1}-1)^2+2\mu_{t1}-1}{\gamma}}$
D	$\frac{1+\gamma\mu_{c0}^2+\beta(\mu_{c1}^2-\mu_{c0}^2)}{2(\gamma\mu_{c0}+\beta(\mu_{c1}-\mu_{c0}))}$
E	$\frac{\mu_{c0}(\beta-\gamma)+\sqrt{\gamma\mu_{c0}^2(\gamma-\beta)+\alpha\beta\mu_{t1}^2+\beta(1-\alpha)(2\mu_{t1}-1)}}{\beta}$
F	$\sqrt{\frac{2\omega(\mu_{Ut}-\mu_{t1})+\alpha(\mu_{t1}-1)^2+2\mu_{t1}-1}{\gamma}}$
G	$\frac{\alpha\mu_{t1}^2+(\alpha-1)(1-2\mu_{t1})+\gamma\mu_{c0}^2+\beta(\mu_{c1}^2-\mu_{c0}^2)}{2(\gamma\mu_{c0}+\beta(\mu_{c1}-\mu_{c0}))}$
H	$\frac{\mu_{c0}(\beta-\gamma)+\sqrt{2\omega\beta(\mu_{Ut}-\mu_{t1})+\gamma\mu_{c0}^2(\gamma-\beta)+\alpha\beta\mu_{t1}^2+\beta(1-\alpha)(2\mu_{t1}-1)}}{\beta}$
I	$\frac{2\omega(\mu_{Ut}-\mu_{t1})+\alpha\mu_{t1}^2+(\alpha-1)(1-2\mu_{t1})+\gamma\mu_{c0}^2+\beta(\mu_{c1}^2-\mu_{c0}^2)}{2(\gamma\mu_{c0}+\beta(\mu_{c1}-\mu_{c0}))}$

Table B.9

Expressions for normalized moment and curvature based on the simplified model

Case	κ_i	M'_i
1	$\frac{-1+\sqrt{\gamma}}{\gamma-1}$	$2\lambda(\gamma-1)\kappa_1^2+6\lambda\kappa_1-6\lambda+\frac{2\lambda}{\kappa_1}$
2	$\frac{-\lambda\left(\alpha(\lambda+1)-1-\sqrt{-\alpha+1+\alpha\gamma\lambda^2}\right)}{-t_1+\gamma\lambda^2}$, $t_1=\alpha(\lambda+1)^2-2\lambda-1$	$\frac{\left((1-\alpha)(3\lambda^2-1)-2\lambda^3(\alpha-\gamma)\right)\kappa_2^2}{\lambda^2}+t_9\,\kappa_2+t_{10}+\frac{2\alpha\lambda}{\kappa_2}$, $t_9=6(\alpha(\lambda+1)-1)$, $t_{10}=3(1-\alpha(1+2\lambda))$
3	$\frac{\lambda\left(\lambda-\sqrt{t_2}\right)}{\lambda^2-t_2}$, $t_2=(\lambda-\mu_{c0})^2(\beta-\gamma)+\gamma\lambda^2$	$\frac{\left(t_5-2\lambda^3(1-\beta)\right)\kappa_3^2}{\lambda^2}+6\lambda(\kappa_3-1)+\frac{2\lambda}{\kappa_3}$, $t_5=(\beta-\gamma)\mu_{c0}\left(\mu_{c0}^2-3\lambda^2\right)$
4	$\frac{2\omega\lambda}{t_4+\gamma\lambda^2}$, $t_4=1+2\omega\lambda+2\mu_{t1}(\omega-1)-\alpha(\mu_{t1}-1)^2$	$\frac{\left(t_7+t_8+2\left(\gamma\lambda^3+\alpha\mu_{t1}^3\right)\right)\kappa_4^2}{\lambda^2}-6\omega\kappa_4+3\omega$, $t_7=(1-\alpha)\left(3\mu_{t1}^2-1\right)$, $t_8=3\omega\left(\lambda^2-\mu_{t1}^2\right)$
5	$\frac{\lambda\left(\alpha(\lambda+1)-1-\sqrt{-\alpha+1+\alpha t_2}\right)}{t_1-t_2}$	$\frac{\left(t_5-2\lambda^3(\alpha-\beta)+(1-\alpha)(3\lambda^2-1)\right)\kappa_5^2}{\lambda^2}+t_9\,\kappa_5+t_{10}+\frac{2\alpha\lambda}{\kappa_5}$
6	$\frac{\lambda\left(\lambda-\sqrt{t_3}\right)}{\lambda^2-t_3}$, $t_3=t_2-\beta(\lambda-\mu_{c1})^2$	$\frac{\left(t_5-t_6-2\lambda^3\right)\kappa_6^2}{\lambda^2}+6\lambda(\kappa_6-1)+\frac{2\lambda}{\kappa_6}$, $t_6=\beta\mu_{c1}\left(\mu_{c1}^2-3\lambda^2\right)$
7	$\frac{2\omega\lambda}{t_4+t_2}$	$\frac{\left(t_5+t_7+t_8+2\left(\beta\lambda^3+\alpha\mu_{t1}^3\right)\right)\kappa_7^2}{\lambda^2}-6\omega\kappa_7+3\omega$
8	$\frac{\lambda\left(\alpha(\lambda+1)-1-\sqrt{-\alpha+1+\alpha t_3}\right)}{t_1-t_3}$	$\frac{\left(t_5-t_6+3\lambda^2(1-\alpha)+\alpha\left(1-2\lambda^3\right)-1\right)\kappa_8^2}{\lambda^2}+t_9\,\kappa_8+t_{10}+\frac{2\alpha\lambda}{\kappa_8}$

9	$\frac{2\omega\lambda}{t_4 + t_3}$	$\frac{\left(t_5 - t_6 - 3\mu_{t1}^2(\omega + \alpha - 1) + \alpha\left(1 + 2\mu_{t1}^3\right) + 3\omega\lambda^2\right)\kappa_9^2}{\lambda^2} - 6\omega\kappa_9 + 3\omega$